Eidgenössische Technische Hochschule Zürich
Swiss Federal Institute of Technology Zurich

Parameter estimation for creating Schrödinger cat states in an electromechanical system

Master's Thesis

Alessandro Bruno

Laboratory for Solid State Physics
Departement of Physics, D-PHYS
ETH Zürich

Supervisors:
Prof. Yiwen Chu
Marius Bild
Yu Yang

March 21, 2022

Abstract

Schrödinger's cat states are defined as macroscopic superpositions of distinct states and have not yet been generated in an acoustic resonator. The goal of this thesis is to demonstrate the creation of such states in a mechanical oscillator. Therefore, we make use of a device containing a superconducting qubit coupled to a High-overtone Bulk Acoustic wave Resonator (HBAR). Recently, parity measurements of phonon modes directly extracted from the phonon state have been demonstrated [1]. In this work, we present the three different protocols for generating a cat state. We simulate the device and the control operations through a simulator framework based on QuTiP and analyze each necessary step of the cat state protocols. Control parameters for the experimental realization of the simulated results are extracted and used for the creation of an approximate cat state of an average phonon number of $\overline{n} \approx 2$. Finally, we simulate the state coherence and sensitivity to a displacement, to characterize the macroscopic nature of these massive quantum states.

Contents

1 Introduction

Domesticating Schrödinger's cat

"The scientist only imposes two things, namely truth and sincerity, imposes them upon himself and upon other scientists."
Erwin Schrödinger

In recent times, the enormous technological advances of the world have thoroughly altered the style in which human beings lead their lives. This radical improvement has been feasible due to the consistent linear density increase in semiconductor devices [2]. The single transistor size is shrinking over time, with some companies like Samsung [3], TSMC [4] and Intel [5] recently adopting a dimension of 5 nm. These companies are ambitiously planning to employ 3 nm processes by 2023 and 2 nm processes by 2025. However, as the chip length approaches the atom size, quantum effects come into play. A possible single atom transistor has been demonstrated [6]. Nevertheless, the control and precision needed for its correct operation renders the whole process non-scalable. The growth in technological complexity seems to be in the process of fading away.

Over the last couple of decades, owing to exceptional development in quantum hardware, a new branch of technology has been originating from quantum mechanics: quantum computers. A couple of years ago, Google [7] has demonstrated quantum advantage of quantum computers based on superconducting circuit over classical ones, by solving an algorithm exponentially faster than a supercomputer. IBM [8] has recently shown a 127 quantum bit (qubit) based quantum computer. Nonetheless, major challenges persist in the process of real-life deployment of quantum computers. Scaling up is an arduous task due to several issues such as the increase of heat load as a function of control lines or qubit connectivity [9]. Furthermore, environmental noise and imperfections in experiment control impede the accuracy of quantum processing units [10].

Quantum Error Correction (QEC) [11], used to protect quantum information from noise, is crucial for universal quantum computation. The adoption of QEC could be employed for Noisy Intermediate-Scale Quantum algorithms (NISQ) [12], potentially feasible for less than a hundred qubits. QEC with bosonic modes, infinite dimension Hilbert space systems, has reached and even exceeded the break-even point [13], i.e. the point in which the lifetime of a logical qubit exceeds every single unit of the system in which it is encoded.

One type of bosonic code is the cat code, based on Schrödinger cat states (SCS), generally defined as superposition of classical states. Encoding in a stabilized cat qubit has been achieved in superconducting circuits [14]. More applications are possible for cat codes for different platforms. In fact, they can be also employed for quantum simulation [15], quantum communication [16], quantum metrology [17] and quantum computation [18, 19].

The aim of this thesis is to generate a SCS inside an acoustic resonator, something which has not achieved thus far. For this purpose, we manipulate a system composed of a mechanical resonator interfaced with a superconducting qubit, whose non-linearity is necessary for deterministically generating quantum states of acoustic waves [20]. Direct measurements of the phonon mode are needed to characterize the quantum state. We manage to perform parity measurements of the phonon Fock state operating in the strong dispersive regime.

In the continuation of this chapter, we explore the Schrödinger cat as a thought experiment and the associated SCS in an analytical way. In chapter 2 we present the background theory of a bosonic field interacting with a two-level atom and the protocols to generate a SCS viable for implementation in our system. In chapter 3, we dive into the theory of superconducting qubits and their interaction with a 3D cavity and the phonon modes in acoustic resonators. In chapter 4, we present simulation results of the necessary steps to create and measure phonon states. Furthermore, the SCSs for the three protocols are generated and

analyzed. In chapter 5, we show the measurements we have performed to create a resonant SCS. In chapter 6, we speak about macroscopicity and possible applications to characterize the state found. In chapter 7, we draw out conclusions about our work and give an outlook for further measurements and applications, potentially exploiting the results of this thesis.

1.1 Schrödinger cat paradox and macroscopic states

The objective and experimental realization of this work are mentally intertwined with an article Schrödinger published in 1935 [21]. Schrödinger criticized one aspect of quantum mechanics: the Copenhagen interpretation [22]. The renowned work states:

"One can even set up quite ridiculous cases. A cat is penned up in a steel chamber, along with the following device (which must be secured against direct interference by the cat): in a Geiger counter, there is a tiny bit of radioactive substance, so small, that perhaps in the course of the hour one of the atoms decays, but also, with equal probability, perhaps none; if it happens, the counter tube discharges and through a relay releases a hammer that shatters a small flask of hydrocyanic acid. If one has left this entire system to itself for an hour, one would say that the cat still lives if meanwhile no atom has decayed. The first atomic decay would have poisoned it. The psi-function of the entire system would express this by having in it the living and dead cat (pardon the expression) mixed or smeared out in equal parts. It is typical of these cases that an indeterminacy originally restricted to the atomic domain becomes transformed into macroscopic indeterminacy, which can then be resolved by direct observation. That prevents us from so naively accepting as valid a "blurred model" for representing reality. In itself, it would not embody anything unclear or contradictory. There is a difference between a shaky or out-of-focus photograph and a snapshot of clouds and fog banks."

This thought experiment based on real life seems completely absurd and contradictory to quantum mechanics. It implies that the cat can exist in a equally weighted superposition of being dead or alive. If the box is still closed (equivalent to the state not measured), this superposition survives indefinitely, only collapsing in one of two states when the box is opened (a measurement is performed). Using the formalism of quantum theory, the wavefunction of the cat is

$$|\psi_{cat}\rangle = \frac{1}{\sqrt{2}}(|\psi_{alive}\rangle + |\psi_{dead}\rangle) \ . \tag{1.1}$$

However, the goal of this thesis is to create a macroscopic superposition of two different quasi-classical states in acoustic modes. The realization of this state has never been reached before. Such a state has a considerable mass compared to previously generated photonic SCSs or based on atoms [23]. A question to pose oneself is how macroscopic these states can become. *Which are the boundaries of quantum mechanics?*

1.2 Cat states in quantum mechanics

Taking inspiration from Schrödinger's conceptual dilemma, the SCS is defined in the framework of quantum mechanics as a quantum superposition of two coherent states with opposite phase. The SCS wavefunction reads [24]

$$|\psi_{\pm}\rangle = \frac{1}{\sqrt{2(1 \pm e^{-2|\alpha|^2})}}(|\alpha\rangle \pm |-\alpha\rangle) \ , \tag{1.2}$$

where $|\pm\alpha\rangle$ is defined as

$$|\pm\alpha\rangle = e^{-\frac{1}{\sqrt{2}}|\alpha|^2} \sum_{n=0}^{\infty} \frac{(\pm\alpha)^n}{\sqrt{n!}} |n\rangle \ . \tag{1.3}$$

Eqn. (A.19) shows two superpositions with a relative phase between the two states of $\theta = 0$ and $\theta = \pi$. These particular states have respectively even and odd parity. This behaviour can be discerned when adding the two coherent states term by term. In fact, the two states ψ_+ and ψ_- turn into

$$\begin{aligned} \psi_+ &\propto e^{-\frac{1}{\sqrt{2}}|\alpha|^2} \left(\frac{\alpha^0}{\sqrt{0!}}|0\rangle + \frac{\alpha^2}{\sqrt{2!}}|2\rangle + \frac{\alpha^4}{\sqrt{4!}}|4\rangle + \cdots \right) \ , \\ \psi_- &\propto e^{-\frac{1}{\sqrt{2}}|\alpha|^2} \left(\frac{\alpha^1}{\sqrt{1!}}|1\rangle + \frac{\alpha^3}{\sqrt{3!}}|3\rangle + \frac{\alpha^5}{\sqrt{5!}}|5\rangle + \cdots \right) \ . \end{aligned} \tag{1.4}$$

However, when referring to an SCS in this work the more general definition is invoked.

$$|\psi_\theta\rangle = \frac{1}{\sqrt{2(1+\cos(\theta)e^{-2|\alpha|^2})}} (|\alpha\rangle + e^{i\theta}|-\alpha\rangle) \ , \tag{1.5}$$

with relative phase between the two coherent states of θ. In the protocols of the next chapter to generate cat states, the term SCS refers to this generalized version.

2 Cat state protocols

Breeding the cat

"It is hard to rationalise or explain why you love what you love. But I have always been interested in science and maths, and in high school I was struck that you could use maths to understand nature and science."
Serge Haroche

After introducing the relevance of a Schrödinger cat state and its convenient applications, the goal of this chapter is to present ways of creating these states in a system coupling a qubit to an harmonic oscillator mode. Three cat state protocols are presented here. To understand one of the protocols implemented in this thesis, covering the basic theory of atom-cavity interaction is a prerequisite. This treatment additionally lays the foundations of the physics of the device described in chapter 3. Most of the derivation of the atom-cavity interaction is taken from [25].
In section 2.1 the Jaynes-Cummings model is presented. Afterwards the three cat state protocols are discussed starting from section 2.2 -the resonant cat- , continuing with section 2.3 -the heralded cat- , and finishing with the qcMAP protocol in section 4.2.3.

2.1 Atom-field interaction

Jaynes-Cummings Model

The model to describe the dynamics of a system of two levels coupled to an infinite dimensional Hilbert space was introduced by Jaynes and Cummings in 1963 [26]. This framework is used for several different experimental domains such as cavity Quantum Electrodynamics (cavity QED) [25], trapped ions [27], circuit QED [28] and also the case of this thesis, circuit Quantum Acousto Dynamics [29].
The full Hamiltonian of the system can be described as:

$$H = H_a + H_c + H_i \ , \tag{2.1}$$

where $H_a = \frac{\hbar\omega_{ge}}{2}\hat{\sigma}_z$, $H_c = \hbar w_c \hat{a}^\dagger \hat{a}$ and H_i represent the atom, cavity and interaction Hamiltonian respectively. Assuming that the cavity mode frequency is close to the atom transition, we can neglect the highly non-resonant terms proportional to $\hat{\sigma}_+ a$ and $\hat{\sigma}_- \hat{a}^\dagger$.
After performing this Rotating Wave Approximation (RWA), the interaction Hamiltonian can be written as:

$$H_i = -i\hbar\frac{\Omega_0}{2}[\hat{a}\hat{\sigma}_+ + \hat{a}^\dagger\hat{\sigma}_-] \ , \tag{2.2}$$

where Ω_0 is the vacuum Rabi frequency measuring the strength of the atom-cavity coupling:

$$\Omega_0 = 2\frac{dE_0 {\epsilon_{\mathbf{a}}}^* \cdot \epsilon_{\mathbf{c}}}{\hbar} \ , \tag{2.3}$$

with d being the dipole matrix element of the atomic transition, $\epsilon_{\mathbf{a}}$ and $\epsilon_{\mathbf{c}}$ the unit vector describing the polarization of the atomic and cavity fields, E_0 the root mean squared amplitude of the vacuum field in the cavity. The eigenstates of the Hamiltonian without the interaction term are the states $|e,n\rangle$ and $|g,n\rangle$ with each of their energies $\hbar(n\omega_c + \frac{\omega_{ge}}{2})$ and $\hbar(n\omega_c - \frac{\omega_{ge}}{2})$. It is straightforward to check that if the atom-cavity detuning $\Delta_c = \omega_{ge} - \omega_c$ is equal to 0, then the uncoupled states $|e,n\rangle$ and $|g,n+1\rangle$ experience degeneracy. As a consequence, except for the ground state $|g,0\rangle$, the excited states are configured as a ladder of doublets, each separated by $\hbar\omega_c$. The total number of atomic and field excitations are represented by the operator $M = \hat{a}^\dagger\hat{a} + \hat{\sigma}_+\hat{\sigma}_-$, which commutes with the Hamiltonian and is a constant of motion. The energy levels of the bare states are shown in Fig. 1(a).

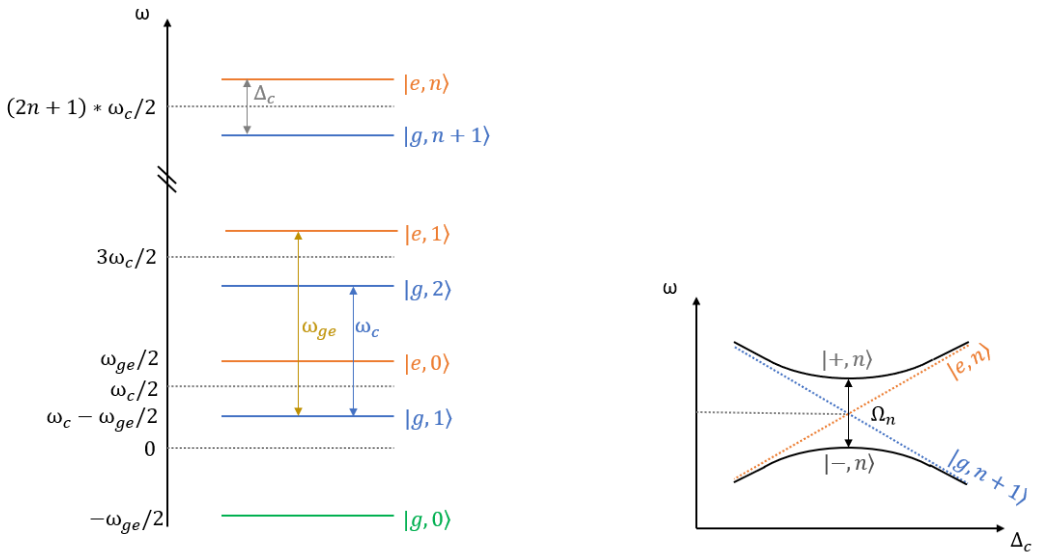

Figure 1: Jaynes-Cummings Hamiltonian energy levels in the (a) bare state energy levels of the atom-cavity system for the whole JC ladder, (b) dressed state energy levels when coupled to each other. ω_c represents the cavity frequency, while ω_{ge} the two-level system frequency, $\Delta_c = \omega_{ge} - \omega_c$ is the detuning between the two.

The interaction term H_i connects states inside a single doublet, solvable in a decoupled manner. Define H_n as the Jaynes-Cummings Hamiltonian referring to the doublet number n, we can write it in matrix form as:

$$H_n = \hbar\omega_c(n + 1/2)\mathbb{1} + V_n \ , \tag{2.4}$$

with

$$V_n = \frac{\hbar}{2}\begin{pmatrix} \Delta_c & -i\Omega_n \\ i\Omega_n & -\Delta_c \end{pmatrix} = \frac{\hbar}{2}(\Delta_c\hat{\sigma}_z + \Omega_n\hat{\sigma}_y) \ , \tag{2.5}$$

and

$$\Omega_n = \Omega_0\sqrt{n+1} \ . \tag{2.6}$$

It is possible to diagonalize H_n by analogy with a spin placed in a magnetic field, whose components in the $\hat{y}$ and $\hat{z}$ directions are proportional to Ω_n and Δ_c respectively. By defining the "mixing angle" θ_n as the angle between the field and the $\hat{z}$ direction by the following formula

$$\tan\theta_n = \Omega_n/\Delta_c \ , \tag{2.7}$$

it is possible to represent the eigenvectors of the Hamiltonian in the $\{|e,n\rangle, |g,n+1\rangle\}$ basis similarly to a two-level system on a Bloch sphere by imposing a relative phase of $\pi/2$ between the two states. These states are

$$\begin{aligned} |+,n\rangle &= \cos\theta_n/2|e,n\rangle + i\sin\theta_n/2|g,n+1\rangle \ ; \\ |-,n\rangle &= \sin\theta_n/2|e,n\rangle - i\cos\theta_n/2|g,n+1\rangle \ , \end{aligned} \tag{2.8}$$

with the corresponding eigenenergies being

$$E_n^{\pm} = (n+1/2)\hbar\omega_c \pm \frac{\hbar}{2}\sqrt{\Omega_n^2 + \Delta_c^2} \ . \tag{2.9}$$

These entangled states are called "dressed states", whose variation as a function of Δ_c is represented in Fig. 1(b). At zero detuning, the atom-cavity coupling transforms the crossing of the bare states into an avoided crossing, with the minimum energy distance between the dressed states being the coupling energy $\hbar\Omega_n$.

Quantum Rabi oscillations

From now on it is assumed that the atom and field are on resonance ($\Delta_c = 0$). The mixing angle is $\theta_n = \pi/2$ and eqn. (2.8) can be rewritten as

$$|\pm, n\rangle = (|e, n\rangle \pm i|g, n+1\rangle)/\sqrt{2} \ , \tag{2.10}$$

separated by Ω_n, i.e. the frequency of the reversible energy exchange between the two systems. Suppose that the atom is initialized in the $|e\rangle$ state placed inside a cavity containing n phonons. The initial state $|\Psi(0)\rangle = |e, n\rangle$ can be rewritten in the dressed state basis

$$|\Psi(0)\rangle = (|+, n\rangle + |-, n\rangle)/\sqrt{2} \ . \tag{2.11}$$

The atom-field state at time t can be described by the time evolution in the rotating frame of the cavity frequency

$$|\Psi(t)\rangle = (e^{-i\Omega_n t/2}|+, n\rangle + e^{i\Omega_n t/2}|-, n\rangle)/\sqrt{(2)} \ . \tag{2.12}$$

By changing back in the uncoupled basis

$$|\Psi(t)\rangle = \cos\frac{\Omega_n t}{2}|e, n\rangle + \sin\frac{\Omega_n t}{2}|g, n+1\rangle \ . \tag{2.13}$$

Analogously, by starting with state $|g\rangle$ in a cavity with $n+1$ phonons, the resulting state is similar, only modified by a phase offset $\pi/2$ in the trigonometric functions. The expression derived represents Rabi oscillations, the reversible energy exchange at frequency Ω_n. An oscillatory spontaneous emission occurs when having initially $|e, 0\rangle$, that couples to $|g, 1\rangle$ and the same for the opposite process, spontaneous absorption. The resulting oscillation has the characteristic frequency Ω_0, hence the name Vacuum Rabi oscillation.

2.2 Resonant cat

In this thesis, the term "resonant cat" is adopted to indicate the approximated Schrödinger cat state that arises from the resonant interaction of a two-level system with a quantum harmonic oscillator prepared in a coherent state [30, 31].

Collapse and revival of Rabi oscillations induced by a coherent field

Considering the atom initialized in the $|e\rangle$ state (the initial state is not relevant for the effect) and the cavity in a coherent field with state and number distribution

$$|\alpha\rangle = \sum_n c_n|n\rangle = e^{-|\alpha|^2/2}\sum_n \frac{\alpha_n}{\sqrt{n!}}|n\rangle \ , \quad p_\alpha(n) = |c_n|^2 = e^{-|\alpha|^2}\frac{|\alpha_n|^2}{n!} \ . \tag{2.14}$$

For each phonon number n, it is possible to calculate the effect of the corresponding Fock state interaction with the atom. The state at time t directly results by substituting the individual Fock state n with the coherent state superposition in eqn. (2.13):

$$|\Psi(t)\rangle = \sum_n (c_n \cos\frac{\Omega_{n+1} t}{2}|e, n\rangle + c_n \sin\frac{\Omega_{n+1} t}{2}|g, n+1\rangle) \ . \tag{2.15}$$

By recalling eqn. (2.6), it is possible to derive Rabi oscillations of the qubit population interacting with a coherent state as a sum of oscillations with frequency $\Omega_0\sqrt{n+1}$ scaled by the corresponding phonon number probability. This probability $P_e(t)$ of finding the atom in the $|e\rangle$ state is shown in subsection 5.3.2 for $\alpha = 3$ and for any coherent state can be written as

$$P_e(t) = \sum_n p_\alpha(n) \frac{1 + \cos\Omega_0\sqrt{n+1}t}{2} \ . \tag{2.16}$$

The qubit populations experience a sequence of idle periods in which it is constant at a value of 1/2, where the qubit is in a superposition state, alternated by oscillation between the qubit $|g\rangle$ and $|e\rangle$ states. This "collapse" of the Rabi oscillation occurs due to the incommensurability of Rabi frequencies of different phonon numbers n. This effect can be simulated even for an interacting atom with a noisy classical field. The "quantumness" of the oscillations depicted can be confirmed by the "revival" of the oscillations, the moment in which different phonon number contributions show constructive interference after rephasing. The revival can be linked to the quantization of the field energy interacting with the qubit. There are two fundamental times that govern the qubit population dynamics: the collapse time t_c and the revival time t_r. At short times, the Rabi oscillation happen at a frequency of nearly $\Omega_0\sqrt{\overline{n}+1}$, proportional to the field amplitude when $1 \ll \overline{n}$, with $\overline{n} = |\alpha|^2$. Afterwards, these oscillations quickly fade away, until shortly before t_c the qubit excited state probability reaches 1/2. The timescale for the collapse time can be estimated by setting the phase variation over the width $\sqrt{\overline{n}}$ of the Poisson distribution to the order of 2π such that states with phonon numbers higher and lower than $\overline{n}$ cancel out

$$\frac{2\,t_c\,\Omega_0\sqrt{\overline{n}+1}}{\sqrt{\overline{n}}} \approx 2\pi \ . \tag{2.17}$$

Since the phase variation itself depends on $\sqrt{\overline{n}+1}$, for high enough $\overline{n}$, the collapse time is independent from the average Fock number. The revival time can be computed by comparing two adjacent phonon numbers n and $n+1$ that rephase by imposing

$$\frac{t_r\,\Omega_0}{2\sqrt{\overline{n}}} \approx 2\pi \ . \tag{2.18}$$

From the previous two equations, the times are

$$t_c \approx \frac{\pi}{\Omega_0} \ , \qquad t_r \approx \frac{4\pi}{\Omega_0}\sqrt{\overline{n}} \ . \tag{2.19}$$

The timescale corresponding to half of the revival time t_r is an essential element of the resonant cat protocol.

An approximated cat state

Previously, the probability of finding the atom state in the excited state over time was computed. However, interesting features manifest themselves by analyzing the cavity state at certain points in time. The reasoning behind the following derivation is taken from [32]. Starting with an initial state:

$$|\Psi(0)\rangle = |\Psi_a(0)\rangle \otimes |\Psi_c(0)\rangle = (c_g|g\rangle + c_e|e\rangle) \otimes (\sum_n c_n|n\rangle) \ , \tag{2.20}$$

the evolution under the Jaynes-Cummings unitary returns the state at time t

$$|\Psi(t)\rangle = \sum_n [(c_e c_n \cos\frac{\Omega_0\sqrt{n+1}}{2}t - ic_g c_{n+1}\sin\frac{\Omega_0\sqrt{n+1}}{2}t)|e\rangle + (-ic_e c_{n-1}\sin\frac{\Omega_0\sqrt{n}}{2}t + c_g c_n\cos\frac{\Omega_0\sqrt{n}}{2}t)|g\rangle] \otimes |n\rangle \ . \tag{2.21}$$

Expanding the following factor in the limit of $\frac{n-\overline{n}}{\overline{n}} \ll 1$ up to the second order gives

$$\sqrt{n+1}-\sqrt{n} = \sqrt{\overline{n}}\left(\sqrt{\frac{n+1}{\overline{n}}}-\sqrt{\frac{n}{\overline{n}}}\right) = \sqrt{\overline{n}}\left[1+\frac{1}{2}\left(\frac{1+(n-\overline{n})}{\overline{n}}\right)+\frac{1}{8}\left(\frac{1+(n-\overline{n})}{\overline{n}}\right)^2 - 1 - \frac{1}{2}\left(\frac{(n-\overline{n})}{\overline{n}}\right)+\frac{1}{8}\left(\frac{(n-\overline{n})}{\overline{n}}\right)^2 + o\left(\left(\frac{n-\overline{n}}{\overline{n}}\right)^3\right)\right] = \frac{1}{2\sqrt{\overline{n}}}\left(1-\frac{n-\overline{n}+1/2}{2\overline{n}}\right)+o\left(\left(\frac{n-\overline{n}}{\overline{n}}\right)^3\right) \ . \tag{2.22}$$

Now, the term inside the trigonometric functions can be approximated as

$$\frac{\Omega_0}{2}t\sqrt{n+1} \approx \frac{\Omega_0}{2}\left[\sqrt{n}+\frac{1}{\sqrt{\overline{n}}}\left(1-\frac{n-\overline{n}+1/2}{2\overline{n}}\right)\right]t \approx \pi\sqrt{\overline{n}}\sqrt{n}+\frac{\pi}{2} \ , \tag{2.23}$$

where in the last step consists in imposing a specific time $t \approx t_0 = \frac{t_r}{2}$, half of the revival time introduced in eqn. (2.19). For a coherent state the coefficients of different Fock number states are related $c_{n+1} = \frac{\alpha}{\sqrt{n+1}}c_n$. In the limit of a large coherent state (already used before) these coefficients can be related to each other in the following manner

$$c_{n+1} = \frac{\alpha}{\sqrt{\overline{n}}}c_n = e^{-i\phi}c_n \ , \tag{2.24}$$

where ϕ is the phase of the coherent state and the result

$$\sqrt{n+1} = \sqrt{\overline{n}}\left(1+o\left(\frac{n-\overline{n}}{\overline{n}}\right)\right) \approx \sqrt{\overline{n}} \ , \tag{2.25}$$

has been used. Replacing our approximations eqn. (2.23) and eqn. (2.24) into eqn. (2.21) and replacing $\frac{\Omega_0\sqrt{n}}{2}t_0 = A$ for better readability

$$|\Psi(t_0)\rangle = \sum_n c_n[(-c_e\sin A - ic_g e^{-i\phi}\cos A)|e\rangle - ie^{i\phi}(c_e\sin A + c_g e^{-i\phi}\cos A)|g\rangle] \otimes |n\rangle = -(|e\rangle + ie^{i\phi}|g\rangle) \otimes \sum_n c_n(c_e\sin A + ic_g e^{-i\phi}\cos A)|n\rangle = |\Psi_a(t_0)\rangle \otimes |\Psi_c(t_0)\rangle \ . \tag{2.26}$$

There are three fundamental things to note in this last equation. At half of the revival time, the atom is disentangled from the cavity, making it possible to measure and control the atom without modifying the state of the cavity. Furthermore, the state can be written as a superposition of macroscopic states by substituting the coherent state coefficients

$$|\Psi_c(t_0)\rangle \approx |\Psi_c^+(t_0)\rangle + |\Psi_c^-(t_0)\rangle, \tag{2.27}$$

with the macroscopic states being

$$|\Psi_c^{\pm}(t_0)\rangle = e^{-\overline{n}/2}\sum_n \frac{\overline{n}^{n/2}}{\sqrt{n!}} e^{\mp i\pi\sqrt{n}\sqrt{\overline{n}}}|n\rangle. \tag{2.28}$$

One additional and final thing to note, subsequently shown in simulations, is that starting with whichever different initial states for the atom, results in the atom state to be disentangled from the cavity at t_0. Furhtermore, this state is relatively straightforward to track for further analysis because it is always a 50-50 superposition state, with a different relative phase θ between the $|g\rangle$ and $|e\rangle$ that depends on the exact initial atom state.

Precise state calculation

The expression at time t_0 for finite n is derived in the following. For calculating the correct state without the approximation of $\overline{n} \to \infty$, the initial point of the computation is again eqn. (2.21). For convenience, two parameters are defined in the following computation: A, from eqn. (2.26) and B, equal to the higher order terms in the expansion neglected in eqn. (2.22). The full expression reads

$$\begin{aligned}|\Psi(t_0)\rangle = \sum_n [&\left(c_e c_n \cos\left(A+\frac{\pi}{2}+B\right) - ic_g c_{n+1}\sin\left(A+\frac{\pi}{2}+B\right)\right)|e\rangle + \\ &(-ic_e c_{n-1}\sin A + c_g c_n \cos A)|g\rangle] \otimes |n\rangle \ .\end{aligned} \tag{2.29}$$

Using $\sin(a+b) = \sin a\cos b + \cos a \sin b$ and $\cos(a+b) = \cos a\cos b - \sin a \sin b$, the expression modifies to

$$\begin{aligned}|\Psi(t_0)\rangle = \sum_n \{[&c_e c_n \left(\cos\left(A+\frac{\pi}{2}\right)\cos B - \sin\left(A+\frac{\pi}{2}\right)\sin B\right) \ + \\ -ic_g c_{n+1}&\left(\sin\left(A+\frac{\pi}{2}+B\right)\cos B + \cos\left(A+\frac{\pi}{2}+B\right)\sin B\right)]|e\rangle \ + \\ &+ \ (-ic_e c_{n-1}\sin A + c_g c_n \cos A)\,|g\rangle\} \otimes |n\rangle \ .\end{aligned} \tag{2.30}$$

Using cosine and sine rules, coherent state coefficient properties and rearranging terms

$$\begin{aligned}|\Psi(t_0)\rangle = &-\sum_n c_e c_{n-1}\left(\frac{\alpha}{\sqrt{n}}(\cos A\sin B + \sin A\cos B)|e\rangle + i\sin A|g\rangle\right)\otimes|n\rangle \ + \\ &-\sum_n ic_g c_n\left(\frac{\alpha}{\sqrt{n+1}}(\cos A\cos B - \sin A\sin B)|e\rangle + i\cos A|g\rangle\right)\otimes|n\rangle \ .\end{aligned} \tag{2.31}$$

where by substituting into A and B the expression for t_0 they can be written as

$$B = -\frac{1}{2\overline{n}}\left(\frac{n-\overline{n}+\frac{1}{2}}{2}\right)\pi \qquad\qquad A = \pi\sqrt{\overline{n}}\sqrt{n} \ . \tag{2.32}$$

This derivation is carried out for the purpose of isolating the terms yielding infidelity. The full formula can be compared with the approximated formula, suggesting possible imperfections with an ideal cat state. The deviation between the two expressions can be seen in Fig. 2, in particular the difference in fidelity between the two as a function of the cat state size α, calculated as [33]

$$\mathcal{F}(\rho_1,\rho_2) = Tr\left[\sqrt{\sqrt{\rho_1}\rho_2\sqrt{\rho_1}}\right]^2 \ , \tag{2.33}$$

for two mixed states ρ_1 and ρ_2 defined in eqn. (A.1). The behaviour of the fidelity is interesting: At small alphas the value is high because both states resemble a vacuum state; as alpha increases there is a dip close to $\alpha = 1$ and an oscillatory behaviour that tends to unity as $\alpha \to \infty$ as expected from one of the two approximations employed previously.

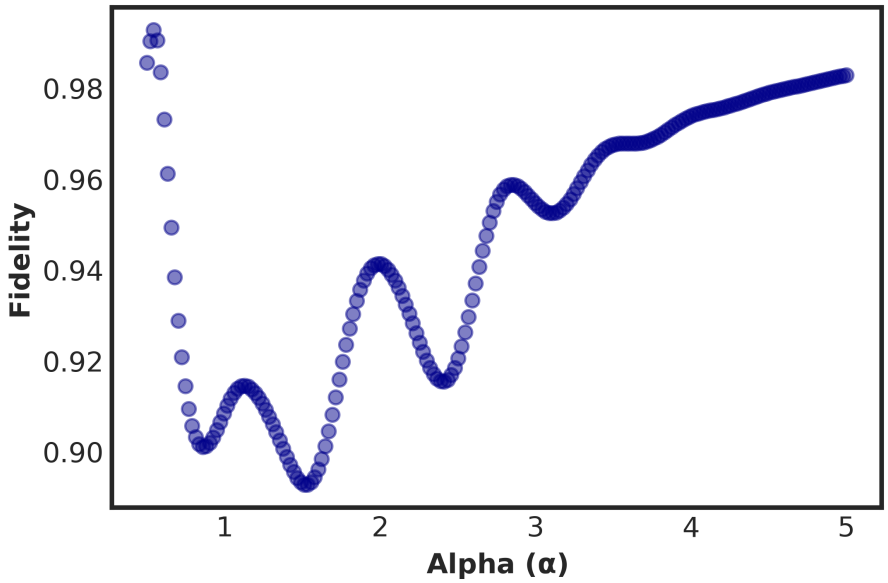

Figure 2: Fidelity between the full resonant cat expression of eqn. (2.31) and the approximated expression of eqn. (2.28) as a function of the cat size α.

2.3 Heralded cat

The term "heralded cat" refers to a particular type of cat state protocol presented in this section. The generated state is not fully deterministic, but can be postselected between an even and odd cat state with a 50% chance. In particular, it is called "heralded" since the state depends on the measured qubit state. The protocol exploits conditional phase gates in the context of the dispersive interaction explained in section 3.3.1, whose experimental realization is discussed in subsection 3.3.1. The sequence of gates of the protocol is shown in Fig. 3. Starting in a vacuum state for both systems, we displace the cavity state:

$$\hat{D}(\alpha)|\Psi(0)\rangle = \hat{D}(\alpha)(|g\rangle \otimes |0\rangle) = |g\rangle \otimes |\alpha\rangle \ , \tag{2.34}$$

where the displacement operator is defined as

$$\hat{D}(\alpha) = e^{(\alpha\hat{a}^\dagger - \alpha^*\hat{a})} \ . \tag{2.35}$$

Afterwards, the sequence requires a $\pi/2$ pulse on the qubit with an arbitrary phase (we choose 0 as the relative phase)

$$\hat{R}_x\left(\frac{\pi}{2}\right)(|g\rangle \otimes |\alpha\rangle) = \frac{1}{\sqrt{2}}(|g\rangle + |e\rangle) \otimes |\alpha\rangle \ . \tag{2.36}$$

The conditional phase gate on the phonon states creates a π phase shift depending on the qubit state. The interaction is possible through the dispersive regime. The qubit is shifted in frequency through a stark shift pulse, as described in subsection 3.1.3. Depending on the qubit state, the cavity coherent state accumulates a different phase. More on that in chapter 4. We can describe this action by a unitary of parameter π/χ by $\hat{S}$

$$\hat{S}\left(\frac{\pi}{\chi}\right)\frac{1}{\sqrt{2}}(|g\rangle + |e\rangle) \otimes |\alpha\rangle) = \frac{1}{\sqrt{2}}(|g\rangle \otimes |\alpha\rangle + |e\rangle \otimes |-\alpha\rangle) \ . \tag{2.37}$$

The cavity and qubit state are now entangled. Afterwards a subsequent $\pi/2$ pulse is performed. Its phase must be chosen accordingly to take into account the relative phase between the two states of the superposition accumulated due to the shift in frequency $e^{-i(\omega_r - \omega_i)t_i}$,

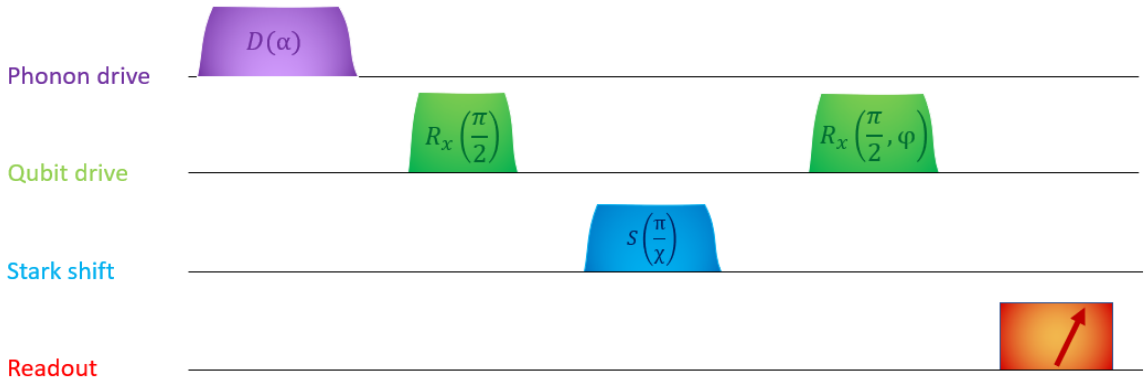

Figure 3: Sequence of gates for the heralded cat.

where ω_r is the qubit rest frequency, ω_i is the qubit interaction frequency, and t_i is the time of the operation, or the interaction time.

$$\hat{R}_x\left(\frac{\pi}{2},\phi\right)\frac{1}{\sqrt{2}}(|g\rangle\otimes|\alpha\rangle+|e\rangle\otimes|-\alpha\rangle)=\frac{1}{\sqrt{2}}\left[\frac{1}{\sqrt{2}}(|g\rangle+|e\rangle)\otimes|\alpha\rangle+\frac{1}{\sqrt{2}}(|g\rangle-|e\rangle)\otimes|-\alpha\rangle)\right]= \\ \frac{1}{\sqrt{2}}\left[\frac{1}{\sqrt{2}}|g\rangle\otimes(|\alpha\rangle+|-\alpha\rangle)+\frac{1}{\sqrt{2}}|e\rangle\otimes(|\alpha\rangle-|-\alpha\rangle)\right]. \tag{2.38}$$

Eventually, a projective measurement collapses the state in one of the cat states. We perform readout and obtain a different cat state of different parity depending on the result

$$\begin{cases}\frac{1}{\sqrt{2}}(|\alpha\rangle+|-\alpha\rangle) & \text{if } |\Psi_q\rangle=|g\rangle \\ \frac{1}{\sqrt{2}}(|\alpha\rangle-|-\alpha\rangle) & \text{if } |\Psi_q\rangle=|e\rangle\end{cases}. \tag{2.39}$$

It is important to notice that in order to use the cat state at the end of the protocol, a Quantum Non-Destructive (QND) measurement on the qubit needs to be employed, thus preserving the "quantumness" of the cavity system. Dispersive readout is what makes the measurement QND. Furthermore, Single-shot readout is a technique needed in case the cat state needs to be employed in applications. Furthermore, the parity of the cat state depends on the qubit state measured. On one hand, this allows to have cat states of different parities. On the other hand, the protocol is non deterministic, instead of the one in the following section.

2.4 qcMAP protocol

The qcMAP is a protocol described in [34]. The qcMAP gate, in Fig. 4, is shown to be subdivided in different gates. This protocol takes more time with respect to the previous protocols for the same system, due to the presence of gates at the end of the control sequence

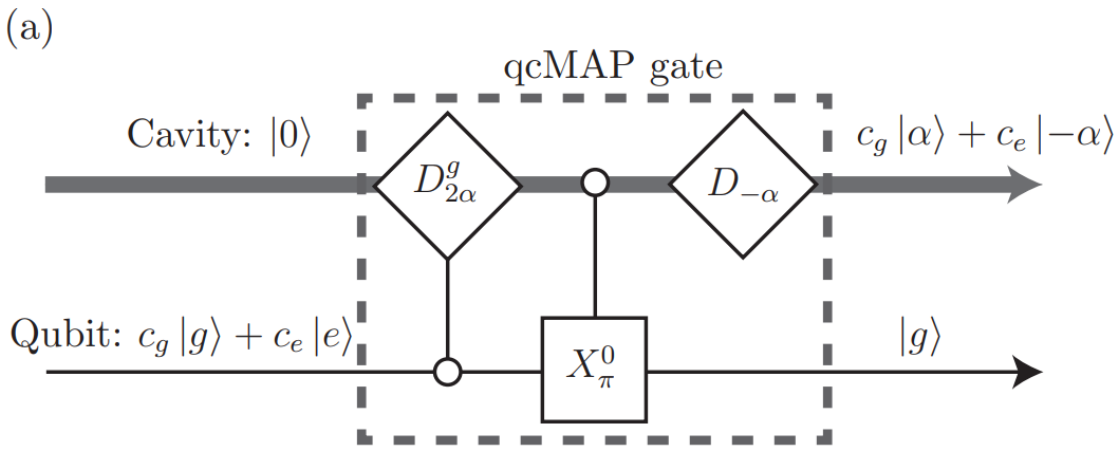

Figure 4: qcMAP gate subdivided into simpler gate. Image taken from [34].

that disentangle the qubit and the phonon state, instead of relying on projective qubit measurements. The disentanglement requires roughly the same amount of time as entangling the two systems. The initial state is

$$\hat{R}_x\left(\frac{\pi}{2}\right)(|\Psi(0)\rangle) = \hat{R}_x\left(\frac{\pi}{2}\right)(|g\rangle \otimes |0\rangle) = \frac{1}{\sqrt{2}}(|g\rangle + |e\rangle) \otimes |0\rangle \ . \tag{2.40}$$

The second operation consists of a conditional displacement $\hat{D}_g(2\alpha)$ of 2α conditioned on the qubit being in the ground state

$$\hat{D}_g(2\alpha)\left[\frac{1}{\sqrt{2}}(|g\rangle + |e\rangle) \otimes |0\rangle\right] = \frac{1}{\sqrt{2}}(|g\rangle \otimes |2\alpha\rangle + |e\rangle \otimes |0\rangle) \ . \tag{2.41}$$

The final gate applied is a conditional pi pulse $\hat{X}^0_\pi$ on the qubit, a pi pulse that depends on the cavity being in the vacuum state. This results in

$$\hat{X}^0_\pi\left[\frac{1}{\sqrt{2}}(|g\rangle \otimes |2\alpha\rangle + |e\rangle \otimes |0\rangle)\right] = \frac{1}{\sqrt{2}}|g\rangle \otimes (|2\alpha\rangle + |0\rangle) \ . \tag{2.42}$$

The final result is a cat state disentangled from the qubit, however displaced by α with respect to the center of the phase space. To bring the cat state back to the origin it is possible to apply an unconditional displacement

$$\hat{D}(-\alpha)\left[\frac{1}{\sqrt{2}}|g\rangle \otimes (|2\alpha\rangle + |0\rangle)\right] = \frac{1}{\sqrt{2}}|g\rangle \otimes (|\alpha\rangle + |-\alpha\rangle) \ . \tag{2.43}$$

This protocol suffers from a large time overhead due to the conditional operations used. It is possible to substitute one conditional operation with the following equality

$$\hat{D}_g(2\alpha) = \hat{D}(\alpha)\hat{S}\left(\frac{\pi}{\chi}\right)\hat{D}(\alpha) \ . \tag{2.44}$$

The full protocol with these substituted gates is shown in Fig. 5. The protocols described in this chapter can be theoretically implemented for generating a cat state in an acoustic resonator with the aid of a superconducting qubit. In the following chapter, the device employed for the SCS generation protocols is illustrated and the necessary physics for understanding the exact implementation is presented.

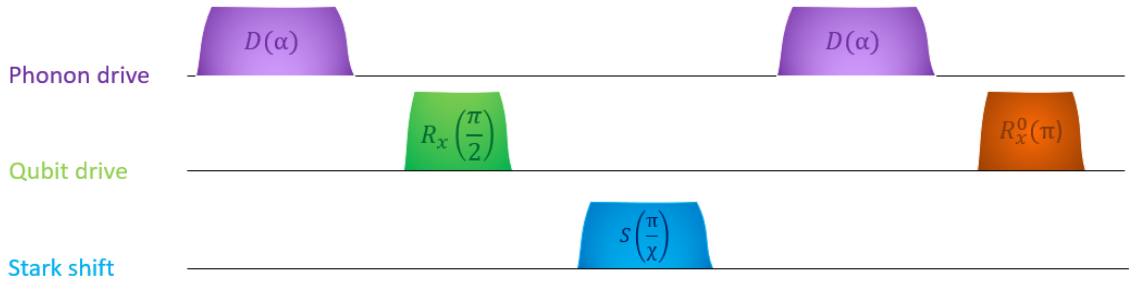

Figure 5: qcMAP gate subdivided into individual phonon and qubit operations. Displacement operation swapped with first $\pi/2$ pulse for experimental implementation.

3 Device physics

Preparing the kennel

"I consider that I understand an equation when I can predict the properties of its solutions, without actually solving it."
Paul Dirac

In the past years, a brand new field of research has been advancing in experimental physics. It is based on the coupling of superconducting qubits to acoustic resonators. This has generated the potential of harnessing control of macroscopic states of mechanical motion. Together with their strong coupling to infrared and microwave photons, acoustic resonators could mediate a transfer between information stored in superconducting qubits and infrared wavelength photons. The types of acoustic resonators are of different kinds, among others are phononic crystals [35], membranes [36], Surface Acoustic Wave resonators (SAW) [37] and High-overtune Bulk Acoustic wave Resonators (HBAR) [38]. All of the proposed devices show strong prospect for quantum state generation and quantum information processing protocols in acoustic modes. In particular the HBAR, a type of a high quality acoustic wave device, has several benefits compared to other acoustic resonators. Due to their small size, thin-Film Bulk Acoustic wave Resonators (FBAR) devices are used everywhere in technology, even in cellphones, complementary to SAWs, and in sensors [39]. The particularity of an HBAR stem from its high quality factor and very compact structure due to the speed of sound being much lower than the speed of light. This means that they have longer coherence times compared to a superconducting qubit and that multiple phonon modes are frequency dense, such that the qubit can address multiple modes. Being able to access several quantum harmonic oscillators modes and control them individually is crucial for the creation of a quantum Random Access Memory (qRAM) [40], useful for several quantum algorithms. Furthermore, their standard fabrication is simpler than producing other acoustic resonators, such as a membrane. There are different types of acoustic modes present in such a structure. In particular, one type is Laguerre-Gaussian (LG) modes [41]. These have a radial number n, and a phase number m. The modes of interest have $n = 0, m = 0$. Different mode families differ by the longitudinal number. Higher order transverse modes have higher number of n, m. In the case of the device employed, the spacing between each mode family is $\approx$ 12 MHz defined as the Free Spectral Range (FSR) of the HBAR. Higher order modes are spaced a multiple of $\approx$ 1 MHz away from the fundamental mode.
The device utilized is the same as used in previous work [1]. A schematic representation of the device is displayed in Fig. 6.

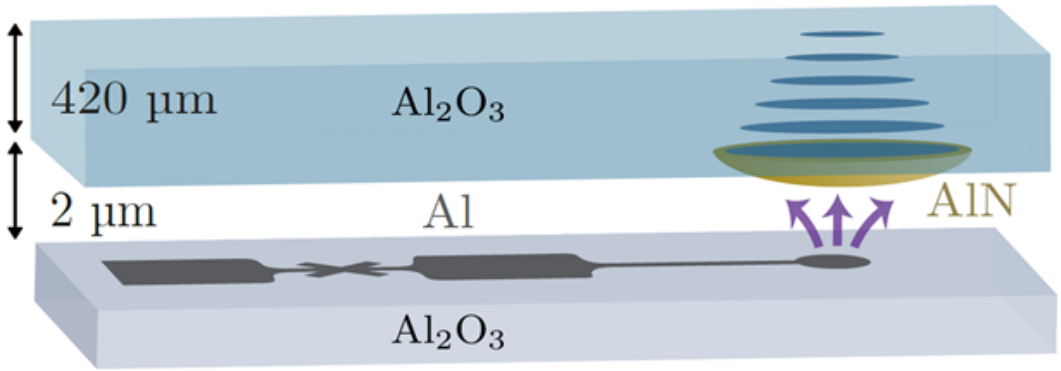

Figure 6: Schematic of the device in use.

It is composed of two chips assembled together in a flip-chip bonding technique and put

inside a 3D cavity made of aluminum. The individual chips are made of sapphire (Al_2O_3) constituting the substrate. the HBAR chip has a dome composed of a piezoelectric material, currently Aluminum Nitride (AlN). This piezoelectric dome, etched on the chip, allows the field from the antenna to enter the substrate in order to couple to the qubit. The superconducting qubit is a standard single-junction, non-flux tunable transmon [42] made of Aluminum sitting on the sapphire substrate. Section 3.1 treats the basics of superconducting qubits, the qubit in the transmon regime, an introduction to its decoherence mechanisms (subsection 3.1.1), the control of a qubit in the system through single qubit rotations (subsection 3.1.2) and stark shift control (subsection 3.1.3). In section 3.2 the physics of a 3D cavity is briefly discussed. Furthermore, the interaction between the cavity and the qubit is highlighted , focusing on the dispersive coupling regime (subsection 3.2.1). The interaction between phonon modes and superconducting qubit is described in section 3.3, in the strong dispersive coupling regime (subsection 3.3.1) together with the operation allowing to drive a phonon mode (subsection 3.3.2).

3.1 The superconducting qubit and the transmon regime

The superconducting qubit is one of the main components of our device. Its non-linearity allows to deterministically generate non-classical states. The basic component of the superconducting qubit is a Josephson junction (JJ), a non-linear inductor composed of two superconducting electrodes with a thin insulating barrier in between. The transmon qubit can be made flux-tunable by fabricating two JJs in a loop such that the transmon frequency can be varied by changing the magnetic flux penetrating the loop. This is not the case in this work, as an aluminum cavity is employed to shield any stray magnetic fields causing frequency noise. The frequency tuning is achieved by applying a probe pulse that induces an AC-stark shift effect on the qubit, as described in section 3.1.3.

The Josephson junction Hamiltonian

The Josephson junction under the critical current I_c can be regarded as a non-linear inductor. The amplitude of this current, depending on the material and the size of the junction, is the maximum current that the qubit can withstand before Cooper pairs, the superconducting charge units, are broken [43]. The element that provides the non-linearity is the Josephson inductance L_j, related to the flux Φ and critical current I_c as a consequence of the two Josephson's equations. Substituting L_j in a normal LC-circuit, the energy levels change from a harmonic oscillator spectrum to an anharmonic transition spectrum. The qubit is defined as the subsystem composed of the ground and first excited state, a two-level system. By adding the shunted capacity C_S, the full Hamiltonian of a Josephson junction can be written in the following way [42]

$$H_{JJ} = 4E_c(\hat{n} - n_g)^2 - E_J \cos\hat{\phi} \ , \tag{3.1}$$

where the first term comes from the capacitive part of the system plus the shunted capacitance, with $n_g = \hat{Q}_g/2e$ being the offset charge and $E_c = e^2/2C_\Sigma$ ($C_\Sigma = C_J + C_S$ the total capacitance, with C_J the capacitance of the JJ) being the capacitive energy. The second term represents the energy stored in the non-linear inductor, with E_J being the Josephson energy. The offset charge arises from undesired effects in the transmon environment together with an external gate voltage $V_g = \hat{Q}_g/C_g$. $\hat{n} = \hat{Q}/2e$ represents the charge number operator (divided by the unit charge of the superconductor) and $\hat{\phi} = (2\pi/\Phi_0)\hat{\Phi}$ the phase operator. The ratio E_J/E_C determine the qubit's sensitivity to offset charge. If the charging energy is larger than the josephson energy $E_J/E_C < 1$, the eigenstates of the Hamilto-

nian are approximately the same ones for the charge operator(the non linearity has a very small effect). Furthermore, the device is strongly sensitive to the offset charge n_g, leading to frequency fluctuations and dephasing. It is possible to remove this problem by working in the transmon regime, where $E_J/E_C \gg 1$. As a consequence of the insensitivity to charge noise, the qubit has longer lifetimes. This behaviour can be seen in Fig. 7.

The transmon qubit

In the transmon limit it is possible to rewrite eqn. (3.1), expanding the cosine in the following fashion.

$$H_T = 4E_c(\hat{n} - n_g)^2 + E_J\frac{\hat{\phi}^2}{2} - E_J\frac{\hat{\phi}^4}{4!} + o(\hat{\phi}^6) \ . \tag{3.2}$$

The approximation $E_J/E_C \gg 1$ allows to remove the offset charge term due to the charge dispersion being suppressed in this regime. Furthermore, while the variance of the charge degree of freedom is large in this regime, using the Heisenberg uncertainty principle, the variance of the conjugate variable $\hat{\phi}$ is small, namely $\Delta\phi = \sqrt{\overline{\phi^2} - \overline{\phi}^2} \ll 1$. Hence, higher order terms from eqn. (3.2) can be removed, transforming the Hamiltonian to the one of a weakly anharmonic oscillator

$$H_T = 4E_C\hat{n}^2 + E_J\frac{\hat{\phi}^2}{2} - E_J\frac{\hat{\phi}^4}{4!} \ . \tag{3.3}$$

Rewriting the Hamiltonian as a function of the creation and annihilation operators of the qubit (respectively $\hat{q}^\dagger$ and $\hat{q}$), allows to easily describe the qubit dynamics and interaction with other systems. The charge number and flux operator can be expressed as

$$\hat{n} = \frac{i}{2}\left(\frac{E_J}{2E_C}\right)^{1/4}(\hat{q}^\dagger - \hat{q}) \ , \qquad \hat{\phi} = \left(\frac{2E_C}{E_J}\right)^{1/4}(\hat{q}^\dagger + \hat{q}) \ . \tag{3.4}$$

It is straightforward to notice from these equations what was mentioned above regarding $\Delta\phi$ decreasing with E_J/E_C, and the opposite for Δn. The final Hamiltonian for a transmon is then

$$H_q = \sqrt{8E_cE_J}\hat{q}^\dagger\hat{q} - \frac{E_C}{12}(\hat{q}^\dagger + q)^4 \ . \tag{3.5}$$

Expanding and keeping only terms that conserve the number of excitations (with the same number of creation and annihilation operators), H_q can be approximated as

$$H_q \approx \hbar\omega_q\hat{q}^\dagger\hat{q} - \frac{E_C}{2}\hat{q}^\dagger\hat{q}^\dagger\hat{q}q \ , \tag{3.6}$$

substituting $\hbar\omega_q = \sqrt{8E_cE_J} - E_C$. This approximation is justified by the fact that in a frame rotating at the qubit frequency ω_q, all terms that are not energy conserving are oscillating. This rotating-wave approximation (RWA) is valid if $\hbar\omega_q \gg E_C/4$, strongly satisfied in the transmon regime. From eqn. (3.6), it is possible to notice that the g-e transition is larger in energy, while the e-f transition is smaller by a factor of E_C. The difference between the two, better known as the anharmonicity α_a, can be defined as

$$\alpha_a = \omega_{ge} - \omega_{ef} \ . \tag{3.7}$$

Typical values for α_a are $\approx 100{-}400$ MHz [42]. This non-linearity is essential to not address unwanted transitions in the transmon spectrum.

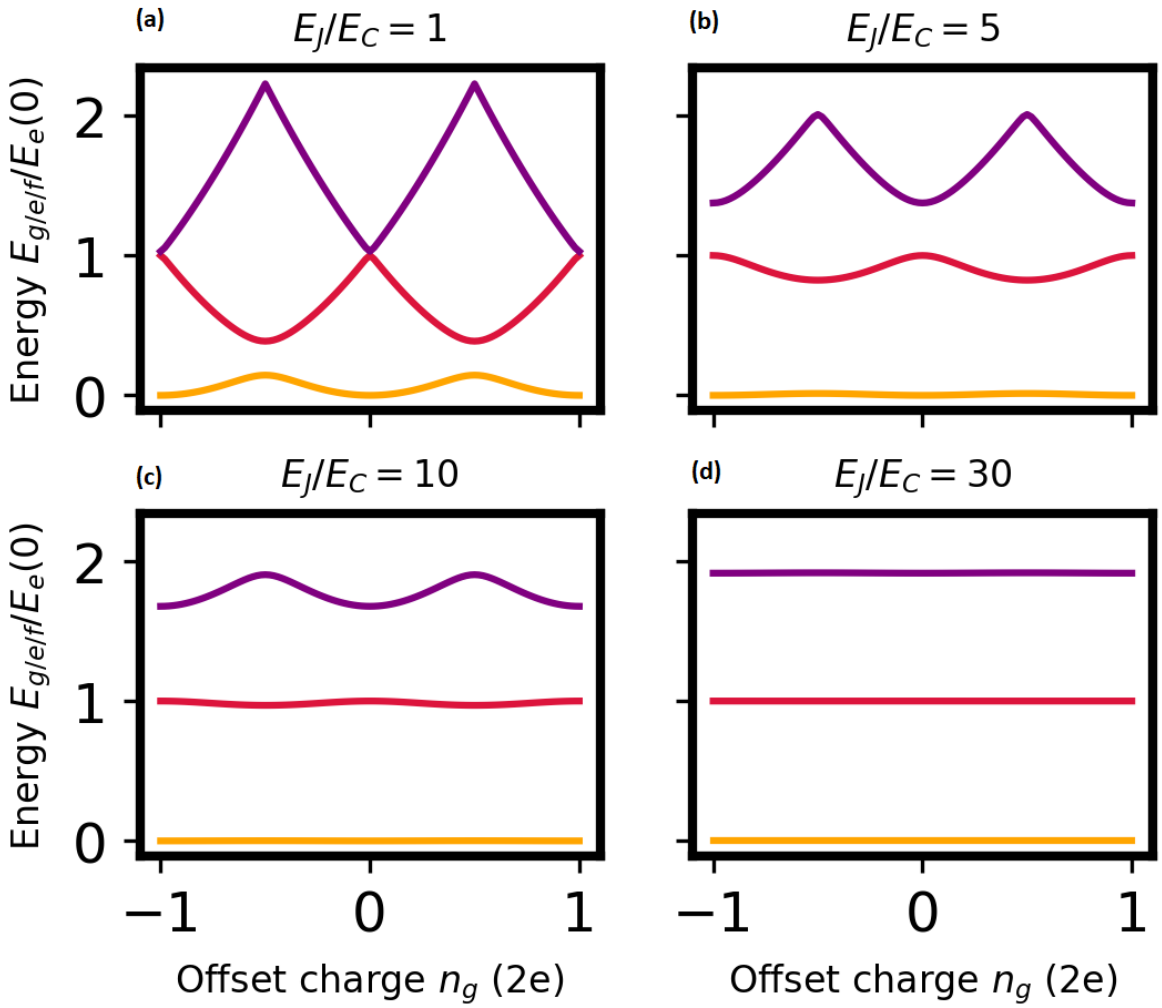

Figure 7: QuTiP simulation of Hamiltonian eigenstates of eqn. (3.1). Plotted are energies of the first three superconducting qubit levels as a function of charge offset plotted for four different ratios of E_J/E_C. In (a) ($E_J/E_C = 1$), the field strongly depends on charge bias that the e and f state are degenerate at integer multiples of n_g. (b) - (d) With increasing E_J/E_C, eigenenergies are increasingly independent of the charge offset.

3.1.1 Decoherence mechanisms

This subsection treats the causes of decoherence both according to theory and in practice. Afterwards, the possible sources of decoherence in the device of this work are discussed for both qubit and HBAR chips. The theory discussion is adapted from the one in [44].

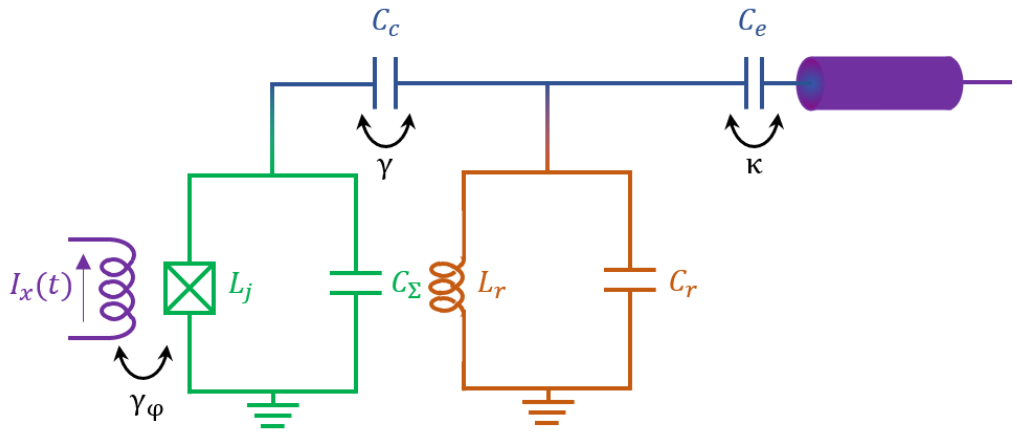

Figure 8: Schematic of the qubit-cavity-environment system. γ_ϕ represents the dephasing noise, γ the decay due to the cavity-environment system and κ the decay from the cavity to the environment. The capacitor C_σ is the full capacitance of the qubit, C_r the one of the cavity, C_c couples the qubit to the cavity and C_e couples the cavity to the environment. L_j is the non linear inductance of the qubit, while L_r is the cavity inductance.

Theory

Qubit losses can be modeled through the coupling to modes of a thermal bath. A schematic of the qubit coupling to the cavity and the environment is shown in Fig. 8. The Hamiltonian of the continuous modes can be written as

$$H_b = \int_0^\infty \hbar\omega \hat{b}_\omega^\dagger \hat{b}_\omega \, d\omega \ , \tag{3.8}$$

where $\hat{b}_\omega$ is the boson mode operator satisfying $[\hat{b}_\omega^\dagger, \hat{b}_{\omega'}] = \delta(\omega - \omega')$. The full Hamiltonian is the sum of the dynamics of the bath, the Hamiltonian of the qubit given in eqn. (3.6) and the interaction Hamiltonian (adapted from [45]).

$$H_{tot} \approx \int_0^\infty \hbar\omega \hat{b}_\omega^\dagger \hat{b}_\omega \, d\omega + \hbar\omega_q \hat{q}^\dagger \hat{q} - \frac{E_c}{2} \hat{q}^\dagger \hat{q}^\dagger \hat{q}\hat{q} + \int_0^\infty \hbar\lambda(\omega_q)(\hat{q}\hat{b}_\omega^\dagger - \hat{q}^\dagger \hat{b}_\omega) \, d\omega \ , \tag{3.9}$$

where

$$\lambda(\omega) = \frac{C_c}{\sqrt{cC_q}} \sqrt{\frac{\omega_q \omega}{2\pi\nu}} \tag{3.10}$$

is the frequency-dependent coupling strength, with C_c being the coupling capacitance between the qubit and the cavity and C_q the qubit capacitance. It is worth mentioning that in eqn. (3.9) two approximations are applied: The first is that $\lambda(\omega)$ can be assumed to be small with respect to ω_q (which is the case in our device), the second is the RWA already used in eqn. (2.2). The first approximation implies that the interaction term can be seen as a perturbation compared to the two bare Hamiltonians. This corresponds to the system

having a high quality factor, so that the qubit is affected in a small range around ω_q. Consequently allowing to write $\lambda(\omega) \approx \lambda(\omega_q)$, as already substituted in eqn. (3.9). The second approximation is the Born-Markov approximation, leading to the Markovian master equation in Lindblad form for the density matrix $\hat{\rho}$ of the transmon state. The master equation is

$$\dot{\hat{\rho}} = -i[H_q, \hat{\rho}] + \gamma(\overline{n}_\gamma + 1)\mathcal{D}[\hat{q}]\hat{\rho} + \gamma\overline{n}_\gamma\mathcal{D}[\hat{q}^\dagger]\hat{\rho} \ , \tag{3.11}$$

where $\mathcal{D}[\hat{O}]$ (with $\hat{O}$, an arbitrary operator) is the dissipator operation acting on $\hat{\rho}$ in the following manner

$$\mathcal{D}[\hat{O}]\hat{\rho} = \hat{O}\hat{\rho}\hat{O}^\dagger - \frac{1}{2}\{\hat{O}^\dagger\hat{O}, \hat{\rho}\} \ , \tag{3.12}$$

with $\{\cdot,\cdot\}$ being the anticommutator. Additionally, $\gamma = 2\pi\lambda(\omega_q)^2$ is the relaxation rate of the artificial atom related to the coupling strength between the qubit and the environment calculated at the qubit frequency. $\overline{n}_\gamma = \overline{n}_\gamma(\omega_q)$ is the thermal photon number of the environment evaluated through the Bose-Einstein distribution $\overline{\hat{b}^\dagger_\omega \hat{b}_{\omega'}} = \overline{n}_\gamma(\omega)\delta(\omega - \omega')$ at the environment temperature T and at the qubit frequency ω_q. In the literature it is customary to consider $\hbar\omega_q \gg k_B T$ at typical dilution refrigerator temperatures, such that $\overline{n}_\gamma \to 0$, even though in reality, a residual thermal qubit population can be measured. A further term to add to the Master equation is one that encompasses dephasing deriving by fluctuations of the transition frequency or stray coupling to other degrees of freedom. Models based on experiments show that the term can be written as [46]

$$2\gamma_\phi\mathcal{D}[\hat{q}^\dagger\hat{q}]\hat{\rho} \ , \tag{3.13}$$

with γ_ϕ being the pure dephasing rate. The full master equation is then

$$\dot{\hat{\rho}} = -i[H_q, \hat{\rho}] + \gamma\mathcal{D}[\hat{q}]\hat{\rho} + 2\gamma_\phi\mathcal{D}[\hat{q}^\dagger\hat{q}]\hat{\rho} \ . \tag{3.14}$$

Analyzing this equation we note that the first term is related to the normal qubit Hamiltonian dynamics, the second is related to the characteristic relaxation time T_1 and the third is related to the dephasing time T_2. Their expressions, found in [47] are

$$T_1 = \frac{1}{\gamma_1} \approx \frac{1}{\gamma} \ , \qquad\qquad T_2 = \frac{1}{\gamma_2} = \left(\gamma_\phi + \frac{\gamma_1}{2}\right)^{-1} \ . \tag{3.15}$$

More precisely, T_1 is defined as the characteristic time for a two-level system to relax from its first excited state to the ground state, while T_2 is defined as the characteristic lifetime of coherent superpositions, including both pure dephasing (γ_ϕ) and relaxation (γ_1). The Markovian master equation in eqn. (3.14) describes very well statistical effects such as qubit relaxation and incoherent excitation, that occur due to the undesired exchange of microwave photons between the qubit and the environment. However, other effects such as dephasing are non-Markovian, since the time scale of the processes is set by the phase coherence time, corresponding to lower-frequencies. This means that the operator introduced for dephasing is based on an inconsistent approximation. Even if the master equation of eqn. (3.14) is wrong in principle, it is still widely applied for predicting steady-state response of the system, where decoherence effects are not averaged out.

System decay and decoherence

As a yardstick, coherence times T_1, T_2 of aluminum-based transmons are currently on the order of $\approx 50 - 120\ \mu s$ [44]. The bare qubits measured in the laboratory can reach coherence times of $\approx 30 - 40\ \mu s$, while, when bonded to an HBAR, they plummet to $\approx 10 - 20$

μs[1]. This difference in coherence times is mainly present due to the piezoelectric coupling. The interaction causes two main effects: dieletric losses in the AlN layer which are known to be considerable, and phonon radiation. In fact, due to the piezoelectric interaction, energy decay to undesired phonon modes is possible. As regards coherence times of the phonon modes, they evaluate to around $\approx 40 - 200\ \mu s$. Several sources of coherence losses can be attributed to HBAR devices. Potential candidates are surface roughness and residual diffraction loss in case the geometry of the fabricated chip is not exactly the one desired.

3.1.2 Single qubit rotations

The control of a superconducting qubit can be achieved through pulse driving at the qubit frequency. The conventional approach in 3D architectures consists in sending a signal in the readout cavity to drive the qubit. Due to the detuning between the two on the order of GHz, a strong input power signal is needed from the source, since a significant portion is reflected. In a device with multiple qubits coupled to the same cavity, it is crucial to design and fabricate them separated in frequency enough from each other, such that there is little to no cross-talk driving between them. In general, consider a microwave drive sent from an Arbitrary Waveform Generator (AWG) at frequency ω_d. It is possible to derive the drive Hamiltonian through input output theory to be

$$H_d(t) = \hbar\epsilon(t)(\hat{q}^\dagger e^{-i\omega_d t - i\phi_d} + \hat{q}e^{i\omega_d t + i\phi_d}) \ , \tag{3.16}$$

where the coherent drive has the parameters $\epsilon(t)$ as the time varying amplitude, phase ϕ_d and frequency ω_d. Afterwards, the simplification of the full Hamiltonian by adding eqn. (3.6) and rotating in a frame at the drive frequency ω_d with the corresponding unitary transformation $U_{\omega_d} = e^{i\omega_d q^\dagger q t}$ leads to

$$U^\dagger_{\omega_d} H_{tot}(t) U_{\omega_d} = U^\dagger_{\omega_d}(H_q + H_d(t))U_{\omega_d} = \hbar\delta_q \hat{q}^\dagger\hat{q} - \frac{E_C}{2}\hat{q}^\dagger\hat{q}^\dagger\hat{q}\hat{q} + \hbar\epsilon(t)(\hat{q}^\dagger e^{i\phi_d} + \hat{q}e^{i\phi_d}) \ , \tag{3.17}$$

with $\delta_q = \omega_q - \omega_d$ being the detuning between the qubit frequency and drive frequency. The usual approximation is to truncate the qubit subspace to a two-level system such that the Hamiltonian reads

$$H'_{tot} = \frac{\hbar\delta_q}{2}\hat{\sigma}_z + \frac{\hbar\Omega_R(t)}{2}[\cos(\phi_d)\hat{\sigma}_x + \sin(\phi_d)\hat{\sigma}_y] \ , \tag{3.18}$$

where $\Omega_R = 2\epsilon$ is the Rabi frequency, $\hat{\sigma}_x$, $\hat{\sigma}_y$ and $\hat{\sigma}_z$ are the Pauli X,Y,Z operators for the qubit. From this expression, it is trivial to choose the right axis of rotation. Setting $\delta_q = 0$ and changing ϕ_d, allows to realize arbitrary single-qubit gates. For example, choosing $\phi_d = 0$ rotations along the X axis of the Bloch Sphere can be performed while $\phi_d = \pi/2$ changes the axis of rotation to Y.

3.1.3 Stark shift control

As described in [48], the presented way to tune the qubit transition frequency consists in applying a strongly detuned microwave tone on the qubit. In the case of $\Omega_R/\delta_q \ll 1$, an ac-Stark shift comes about instead of Rabi oscillations due to virtual transitions caused by the drive. It is possible to start from eqn. (3.17) and derive an approximated off-resonant driven Hamiltonian

$$H_{ss} \approx \frac{1}{2}\left(\hbar\omega_q - E_C\frac{\Omega_R^2}{2\delta_q}\right) \ . \tag{3.19}$$

It is interesting to note that this Hamiltonian can also be used to realize Z rotations in case of a finite time microwave drive. Due to the phonon mode frequencies being very close to the qubits, the stark shift is performed in a slightly different manner, in order to reduce undesired driving of the qubit. This is carried out by choosing a stark drive frequency close to the cavity at a detuning $\delta_c = \omega_{st} - \omega_c$ such that the Hamiltonian is proportional to

$$H_{ss} \propto \frac{\Omega_R^2}{\delta_c^2 \delta_q} \ . \tag{3.20}$$

The stark shift is stronger when closer to the cavity, due to higher transmission at the cavity input port, since the cavity acts as a band-pass filter around the cavity frequency. Typical values for δ_c are on the order of 20 - 200 MHz, such that the qubit can be tuned over a range of 50 MHz. It is essential for δ_c to be far away enough from the cavity frequency, because driving too closely to the cavity populates the cavity itself, generating undesired effects. This method for tuning the qubit has the disadvantage that it can only be lowered in frequency. As seen in section 3.3, this is not an issue, because the phonon mode spectrum is periodic. Thus, the qubit can be tuned to address the closest modes lower in frequency.

3.2 3D cavity

3D resonator cavities are formed by a conducting material that confines the eigenmodes of the electric field inside. While being less scalable compared to coplanar waveguides, 3D cavities are preferred due to their lower surface induced loss. In fact, in a 3D cavity, the energy of the modes is stored in the vacuum inside instead of near the surface [49]. On the contrary, 2D resonators, having smaller feature sizes, have usually lower internal quality factors Q. A typical shape of these cavities is rectangular, constituted by a portion of a waveguide terminated by conducting walls. In essence, the cavity is composed of metal on all sides surrounding vacuum. The metal used for the 3D cavity is usually either copper, allowing for the magnetic field to penetrate inside the cavity, or aluminum, to further increase the internal quality factor up to the order of 10^6 - 10^7, with subsequently less losses at cryogenic temperatures. Stray magnetic fields induces instances of non-superconducting material. since aluminum is paramagnetic, magnetic field lines are shielded out. The boundary conditions are imposed by the metallic structure on the field. The frequencies of the cavity modes are determined by the box dimensions [50]

$$\omega_{mnl} = c\sqrt{\left(\frac{m\pi}{a}\right)^2 + \left(\frac{n\pi}{b}\right)^2 + \left(\frac{l\pi}{d}\right)^2} \ , \tag{3.21}$$

with a,b and d being the cavity dimensions, m,n and l the three corresponding mode numbers (integers and ≥ 0) and c the speed of light. It is possible to obtain a target frequency of several GHz for the first modes with all three dimensions a,b and d on the order of centimeters. The modes are not dependent from each other, such that the Hamiltonian of the cavity is

$$H_c = \sum_m \hbar\omega_m \hat{a}_m^\dagger \hat{a}_m \ , \tag{3.22}$$

simply a sum of independent harmonic oscillators.

3.2.1 The qubit-cavity dispersive regime

The Jaynes-Cummings interaction between a two-level system and a cavity system was already discussed in section 2.1. In the case of the system treated here, the qubit represents

the atom, while the 3D resonator represents the cavity. To simplify our calculations let us define an effective coupling factor g independent from n in the following fashion

$$g = \frac{1}{2}\frac{\Omega_n}{\sqrt{n+1}} \ . \tag{3.23}$$

With this new variable, the full Hamiltonian H (eqn. (2.1)) can be rewritten, substituting eqn. (3.6)

$$H = \hbar\omega_c \hat{a}^\dagger \hat{a} + \hbar\omega_q \hat{q}^\dagger \hat{q} - \frac{E_C}{2}\hat{q}^\dagger \hat{q}^\dagger \hat{q} q + \hbar g(\hat{q}^\dagger \hat{a} + q\hat{a}^\dagger) \ , \tag{3.24}$$

taking from eqn. (3.22) only the first order mode closer to the qubit, because higher order modes are too high in frequency to interact. The JC Hamiltonian is found by going through the same steps as already discussed in section 2

$$H_{JC} = \hbar\omega_c \hat{a}^\dagger \hat{a} + \hbar\frac{\omega_q}{2}\hat{\sigma}_z + \hbar g(\hat{a}\hat{\sigma}_+ + \hat{a}^\dagger \hat{\sigma}_-) \ , \tag{3.25}$$

with the usual RWA and two-level approximation for the qubit. The resulting states are described in eqn. (2.8). The qubit is in a mixed state when tracing out the resonator subspace. It is more efficient and preferred to work in the dispersive regime, where the coupling strength is much smaller with respect to the resonator-qubit detuning, i.e. $\lambda = |g/\Delta| \ll 1$. Qubit and resonator are only weakly coupled through virtual photon interaction. Starting from eqn. (3.24), it is possible to perform a Schrieffer-Wolff transformation, equivalent to second-order perturbation theory. As long as the interaction term in the equation is small, the dispersive Hamiltonian can be approximated to

$$H_{disp} \approx \hbar\omega_c' \hat{a}^\dagger a + \hbar\frac{\omega_q'}{2}\hat{\sigma}_z + \hbar\frac{\chi}{2}\hat{a}^\dagger a\hat{\sigma}_z \ , \tag{3.26}$$

with the qubit truncated to a two-level system. The new parameters in the equation are the dressed frequencies of the cavity ω_c' and the qubit ω_q', and the qubit state dependent dispersive cavity shift χ. These take the form

$$\omega_c' = \omega_c - \frac{g^2}{\Delta - E_C/\hbar} \ , \qquad \omega_q' = \omega_q + \frac{g^2}{\Delta} \ , \qquad \chi = -\frac{g^2 E_C/\hbar}{\Delta(\Delta - E_C/\hbar)} \ , \tag{3.27}$$

with ω_c and ω_q being the bare cavity and qubit frequencies. Eqn. (3.26) can be read in two different ways: If the qubit transitions to the excited state, then the resonator shifts by χ in frequency. At the same time, if the cavity is populated by n photons, the qubit shifts by $n\chi$ in frequency. Hence, it is important that the linewidth of the two is much smaller than the dispersive parameter χ (so the decoherence times of eqn. (3.15) have an effect on a longer timescale). That is because the cavity needs to shift enough in frequency depending on the qubit state allowing to differentiate the two states when measuring. By defining κ as the linewidth of the cavity, this means

$$\gamma \ll \chi \ , \qquad \kappa \ll \chi \ . \tag{3.28}$$

This condition is denoted as strong dispersive regime.

3.3 Circuit QAD

The field of circuit Quantum Acousto-Dynamics (cQAD) has been developing in the recent years [29]. It stems from the analogous, more well-established field of circuit Quantum Electro-Dynamics (cQED) [44]. The two are almost equivalent: the interaction between a superconducting qubit and an electrical resonator can be modeled in the same way of the interaction between the qubit and a mechanical resonator. This is due to the same quantum structure of the two resonators, both being bosonic modes.

3.3.1 Strong dispersive regime in cQAD

The strong dispersive regime described through eqn. (3.28) has been experimentally reached in cQED for some time. Despite the similarities between cQAD and cQED, the same thing can not be claimed for cQAD. In fact, only recently this regime has been realized [1], due to improved qubit coherence. As regards theory, most of the results of section 3.2.1 are translated to this case. The full Hamiltonian of the qubit-phonon system is

$$H = \sum_k \hbar\omega_k \hat{b}_k^\dagger \hat{b}_k + \hbar\omega_q \hat{q}^\dagger \hat{q} - \frac{E_C}{2}\hat{q}^\dagger \hat{q}^\dagger \hat{q}\hat{q} + \sum_k \hbar g_k (\hat{b}_k \hat{q}^\dagger + \hat{b}_k^\dagger \hat{q}) \tag{3.29}$$

The qubit linewidth is a lot smaller than the spacing between the different modes. The coupling term g to higher order modes (LG-01 for example) is not present when coupling to LG-00. Furthermore, the frequency of higher order transverse modes have a greater frequency than the fundamental mode. Thus, the qubit resting point is chosen below the fundamental mode, so as not to couple to others. When every assumption is satisfied, the interaction with other modes can be neglected. Moreover, g and the detuning $\delta_k = \omega_q - \omega_k$ between the qubit frequency ω_q and the k phonon mode frequency ω_k needs to be compared with the FSR such that the qubit is not on resonance with other longitudinal modes. The dispersive regime approximation can be pursued if the condition $g \ll \delta_k$ holds. Similarly to eqn. (3.26), the Hamiltonian can be reduced to a single phonon mode in case the FSR is large enough and the coupling is adequately selective. Using the two-level system approximation we get

$$H_{pdisp} \approx \hbar\omega_k \hat{b}_k^\dagger \hat{b}_k + \hbar\frac{\omega_q}{2}\hat{\sigma}_z + \hbar\frac{\chi}{2}\hat{b}_k^\dagger \hat{b}_k \hat{\sigma}_z \ , \tag{3.30}$$

by substituting the dressed frequencies from eqn. (3.27). Further approximation of the dispersive parameter χ in the equations can be performed using $\alpha_a \gg \delta_k$, condition opposite to the cQED case, where the anharmonicity is much less than the detuning between cavity and qubit. As a function of $\alpha = \hbar E_C/2$, χ can be written as

$$\chi = -2\frac{|g|^2}{\delta_k}\frac{\alpha_a}{\delta_k - \alpha_a} \approx 2\frac{|g|^2}{\delta_k} \ . \tag{3.31}$$

We can notice that χ in this regime depends just on the coupling and the phonon-qubit detuning. Hence, it is of utmost importance to improve the coupling in order to reach a high χ, key not only for better state separation but also the SCS protocols of section 2. Furthermore, the FSR limits how much the qubit can be detuned until it is closer to another fundamental mode after a detuning of FSR/2. For the purposes of this thesis, the FSR stemming from the device implies a limitation on the qubit-phonon coupling g, which must be less than a MHz to individually couple to each phonon mode. Higher coupling would allow to operate in a different regime, with several potential applications such as creating states of multiple phonon modes.

3.3.2 Phonon driving

Creating a coherent state in the mechanical resonator is crucial for the resonant cat protocol of section 2.2 and for characterizing the state in a phonon mode. In this subsection the creation of a phononic state is computed. A phonon mode can be probed by sending a signal at its frequency. The antenna of the qubit interacts with the piezolectric layer of the phonon cavity, transforming the electric signal in acoustic waves. A schematic of the full system and the drive pulse sent is shown in Fig. 9. Consider the longitudinal modes,

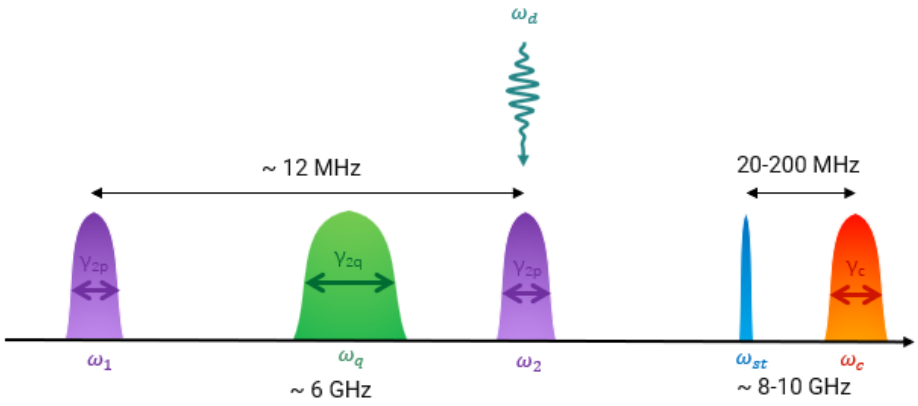

Figure 9: Schematic picture of system components in frequency space. In purple longitudinal phonon modes are shown. In green the qubit is shown, at around 6 GHz. In red the cavity is shown, usually between 8-10 GHz. In blue we can see the stark shift drive discussed in subsection 3.1.3. In aqua green the drive to a phonon mode is shown.

ordered by k and apply a drive on resonance with one of the modes. The corresponding Hamiltonian in the interaction picture of the qubit and the phonon can be written as

$$H_{pdrive} = -\hbar\frac{\alpha_a}{2}\hat{q}^\dagger\hat{q}^\dagger\hat{q}\hat{q} + \hbar\sum_k (g_k\hat{q}^\dagger\hat{b}_k e^{-i\delta_k t} + g_k^*\hat{q}\hat{b}_k^\dagger e^{i\delta_k t}) + \hbar\epsilon\hat{q}^\dagger e^{-i\delta_q t} + \hbar\epsilon^*\hat{q}e^{i\delta_q t} \ , \quad (3.32)$$

where g_k is the coupling between each qubit and phonon mode, $\delta_k = \omega_k - \omega_q$ is the detuning between each phonon mode and the qubit, $\delta_q = \omega_d - \omega_q$ is the detuning between the drive and the qubit, as before. Define $\lambda_k = g_k/\delta_k$ and use the following unitary U' to remove the coupling term in H_{pdrive}

$$U' = e^{-\sum_k(\lambda_k\hat{b}_k\hat{q}^\dagger e^{-i\delta_k t} + \lambda_k^*\hat{b}_k^\dagger\hat{q}e^{i\delta_k t})} \ . \quad (3.33)$$

Using the well known

$$H_{rot} = UHU^\dagger + i\hbar\frac{\delta U}{\delta t}U^\dagger \ , \quad (3.34)$$

the commutation relation for Fermionic operators $[\hat{q}^\dagger, \hat{q}] = 1$ and the Baker-Campbell-Hausdorff (BCH) formula [51] that states that for two possibly noncommutative operators $\hat{\mathcal{X}}$, $\hat{\mathcal{Y}}$ in the Lie algebra of a Lie group

$$\begin{aligned} e^{\hat{\mathcal{X}}}e^{\hat{\mathcal{Y}}} &= e^{\hat{\mathcal{Z}}} \ , \\ \hat{\mathcal{Z}} &= \hat{\mathcal{X}} + \hat{\mathcal{Y}} + \frac{1}{2}[\hat{\mathcal{X}}, \hat{\mathcal{Y}}] + \frac{1}{12}[\hat{\mathcal{X}}, [\hat{\mathcal{X}}, \hat{\mathcal{Y}}]] - \frac{1}{12}[\hat{\mathcal{Y}}, [\hat{\mathcal{X}}, \hat{\mathcal{Y}}]] + \cdots \ , \end{aligned} \quad (3.35)$$

getting

$$H'_{pdrive} = -\hbar\frac{\alpha_a}{2}\hat{Q}_1^\dagger\hat{Q}_1^\dagger\hat{Q}_1\hat{Q}_1 + \hbar\sum_k(\lambda_k\hat{b}_k e^{i(\delta_k-\delta_q)t} + \lambda_k^*\hat{b}_k^\dagger e^{-i(\delta_k-\delta_q)t}) + \hbar\epsilon\hat{q}^\dagger e^{-i\delta_q t} + \hbar\epsilon^*\hat{q}e^{i\delta_q t} \ , \quad (3.36)$$

where $\hat{Q}_1 = \hat{q} + \sum_k \lambda_k\hat{b}_k e^{-i\delta_k t}$. In order to remove the qubit drive an additional unitary transformation must be performed

$$U'' = e^{-(\frac{\epsilon}{\delta_q}\hat{q}^\dagger e^{-i\delta_q t} + \frac{\epsilon^*}{\delta_q}\hat{q}e^{i\delta_q t})} \ , \quad (3.37)$$

leading to the final Hamiltonian

$$H''_{pdrive} = -\hbar\frac{\alpha_a}{2}\hat{Q}^\dagger\hat{Q}^\dagger\hat{Q}\hat{Q} + \hbar\sum_k(\epsilon^*\lambda_k^*\hat{b}_k e^{i(\delta_k-\delta_q)t} + \epsilon\lambda_k\hat{b}_k^\dagger e^{-i(\delta_k-\delta_q)t}) \ , \tag{3.38}$$

with $\hat{Q} = \hat{Q}_1 + \epsilon e^{-i\delta_q t}$. This is just an approximation up to the first order, so it is valid only for low amplitudes. It is now crucial to note that how much the phonon mode is driven is proportional on the intensity of the drive ϵ, as well as λ_k, which is proportional to the coupling g_k, but also inversely proportional to the detuning δ_k to the qubit. The device g_k and the FSR of the phonon modes constrains phonon state creation. The limitation is discussed more in detail in section 4.1.1. Since there is in principle no strong limitation on the driving power ϵ_k, δ_k can be increased as desired. It is then necessary to have a tradeoff between a faster drive (when λ_k is big) and a small induced qubit population (when λ_k is small). Close to the end of the project, the coherent drive for the parameters of cQAD turned out different from what was expected. This is explained in Appendix D. The phonon drive is the fundamental ingredient of all the cat simulations of the next chapter.

4 Simulations

Playing with the felines

"One of the basic rules of the universe is that nothing is perfect. Perfection simply doesn't exist. Without imperfection, neither you nor I would exist"
Stephen Hawking

It is possible to simulate the Hamiltonian of our device through the Python QuTiP package [52]. In this way, it is not complicated to reproduce just the evolution of the protocols described in section 2. However, to fully characterize the experimental process state characterization and further imperfections can also be included. These processes can be implemented through specific QuTiP packages, such as "circuit", "compiler" and "qip", allowing for pulse simulations. Based on these concepts, part of the work of the thesis consists in developing a simulator framework which encompasses the master equation solver plus the alluded packages. The whole structure slows down the full simulations, in exchange for better predictions, code consistency and structure. The parameters that are used in the simulations (unless ideal simulations or further stated) are summed up in Table 1. Most of the parameters are chosen based on the settings and results of the measurements in chapter 5. Clearing doubts on the remaining parameters: the qubit Hilbert space dimensions N_q is fixed to be 2 due to simulation speed and because decay in the f-state is not considered a major decay channel, the phonon Hilbert space dimensions N_p must be carefully chosen after compromises between simulation speed and abiding to real physics, the number of phonon modes n_{phon} is fixed to 1 (always for simulation length). Coherent state amplitude α_p is discussed in subsection 4.2. These constraints could inadvertently change the simulation results, hence, is crucial to pay attention on not going out of the boundaries instantiated.

Parameter	Symbol	Value
Qubit Hilbert space dimensions	N_q	2
Qubit frequency	ω_q	variable
Qubit rest frequency	ω_{qr}	5.969940 GHz
Qubit interaction frequency	ω_{qi}	5.972295 GHz
Qubit relaxation time	T_{1q}	10.1 µs
Qubit dephasing time	T_{2q}	8.8 µs
Phonon Hilbert space dimensions	N_p	30, more if needed
Phonon mode numbers	n_{phon}	1
Phonon frequency	ω_p	5.974117 GHz
Phonon relaxation time	T_{1p}	84.5 µs
Phonon dephasing time	T_{2p}	105.0 µs
Coherent drive duration	t_d	6 µs
Coherent drive single tail duration	$t_{\hat{\sigma}}$	0.2 µs
Rest detuning	δ_k *or* δ_{qr}	4.177 MHz
Interaction detuning	δ_k *or* δ_{qi}	1.822 MHz
Qubit-phonon coupling	g	258.5 kHz
Coherent state amplitude generated	α_p	1.5
Free spectral range	FSR	12 MHz

Table 1: Simulation parameters. Mostly settings and results from chapter 5, plus others chosen ad hoc. All frequencies must be multiplied by 2π. More explanation in text.

In this chapter the simulation steps needed for all the protocols in section 4.1 are presented. These are: coherent state creation (subsection 4.1.1), ramsey-like parity measurements in the dispersive regime (subsection 4.1.2) and the wigner tomography possible to infer from several displaced parity measurements (subsection 4.1.3). Afterwards the full simulations for the cat states examined in section 4.2 is shown: the resonant cat (subsection 4.2.1), the heralded cat (subsection 4.2.2) and the qcMAP (subsection 4.2.3). For each protocol, several properties and dependences are analyzed.

4.1 Simulation steps

Given the complexity of the protocols, it is functional to split them in steps and analyze each operation by itself. Through the simulator, different parameters are tuned and the system dynamics are emulated through the simulation of real physics operations. The three most important single steps to analyze are the creation of a coherent state in the phonon oscillator, the Ramsey sequences in the dispersive regime for parity measurements and full state characterization through Wigner tomography.

4.1.1 Coherent state creation

Phonon driving through a qubit antenna was derived in subsection 3.3.2. For convenience, the Hamiltonian is rewritten isolating the driving term

$$H_{drive} = \hbar \sum_k (\epsilon^* \frac{g^*}{\delta_k} \hat{b}_k e^{i(\delta_k - \delta_q)t} + \epsilon \frac{g}{\delta_k} \hat{b}_k^\dagger e^{-i(\delta_k - \delta_q)t}) \ , \tag{4.1}$$

where the parameters are already defined in subsection 3.3.2. Several consideration stem out from the Hamiltonian and device physics. Firstly, g (simplified from g_k) solely depends on the device properties and is incontrollable after device fabrication. Another parameter, δ_k, the rest detuning, can be tuned in-situ as described in subsection 3.1.3. It is essential for the qubit frequency to be not too close to the phonon mode, otherwise the resonant JC interaction could make the phonon population decay. The last two parameters, δ_q and ϵ, just depend on the specific drive, giving the option to tune coherent state amplitude and phase. Other criterions, missing from the equation, surface when taking into account the approximation applied previously. As mentioned earlier, the higher order transverse modes are not detrimental in an appreciable manner to our system, due to their low coupling with the qubit. However, coupling to other modes is relevant when considering longitudinal modes. Careful calibration of qubit detuning compared to the FSR of the main modes plays a fundamental role in making sure undesired phonon modes do not couple to our phonon drive. For the aforementioned reasons, it is necessary to reduce the extension in frequency of our drive. The mentioned requirement is achieved by using a gaussian square pulse instead of a common square pulse. The comparison with a square pulse in time domain and frequency space is presented in Appendix C. The state created through eqn. (4.1) is shown in Fig. 10(a). The fidelity for the state for the parameters mentioned in table 1 is $\mathcal{F} = 0.955$, calculated by taking the density matrix overlap with an ideal coherent state with the same amplitude $\alpha = 1.5$. It is important to mention that the fidelity considered in the work is always the square as the default QuTiP fidelity, justifying the lower numbers with respect to the ones the reader might be accustomed to. The expression is the following

$$\mathcal{F}(\hat{\rho_1}, \hat{\rho_2}) = Tr \left(\sqrt{\sqrt{\hat{\rho_1}} \hat{\rho_2} \sqrt{\hat{\rho_1}}} \right)^2 \tag{4.2}$$

with the density matrices $\hat{\rho_1}, \hat{\rho_2}$ defined in eqn. (A.1). The fidelity of a coherent state has an inverse square dependence with respect to the coherent state amplitude when accounting

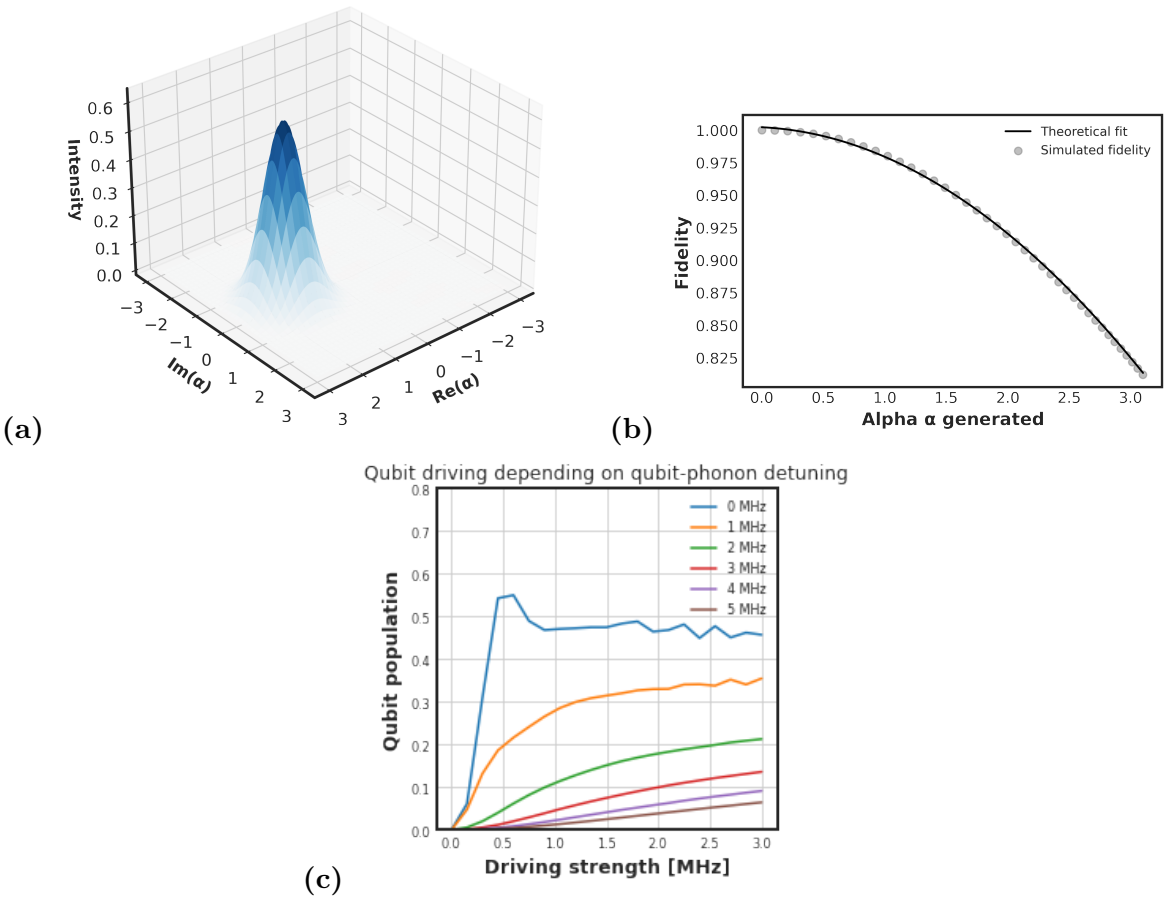

Figure 10: (a) Coherent state created for $\alpha = 1.5$. (b) α generated against fidelity with a square function theoretical fit on top. (c) Qubit population as a function of driving strength for different qubit-phonon detunings.

for losses: $F \propto 1/\alpha^2$. The proportionality is accurately fitted in Fig. 10. The actual values vary based on the rest detuning δ_k and the coherent drive duration t_d. When driving the phonon mode, the qubit can be inadvertently driven due to the broadening in frequency of the drive pulse. In Fig. 10(c), qubit population as a function of the driving strength ϵ for different detunings is shown. Naturally, when on resonance the qubit has a high population. As the qubit is tuned further away, the unwanted qubit population is decreased. However, the coherent state alpha is also different for equal amplitude at different detunings. As a consequence, it is an instrumental analysis to inspect qubit population for the same amplitude α at different detunings δ_k. Furthermore, it is instructive to add a dependency on the drive duration t_d, considering that the faster drive the less the system decoheres. In Fig. 11(a) the coherent state generated with a drive of amplitude ϵ and drive duration t_d for a detuning $\delta_k = 10$ MHz is shown. A linear dependency on both ϵ and t_d is present, as expected from the Hamiltonian evolution. In Fig. 11(c) the generated qubit population is shown for the same detuning δ_k. In Fig. 11(b) the amplitude α is plotted for a smaller detuning $\delta_k = 5$ MHz and in Fig.11(d) the qubit population is displayed for the same parameters. An imperfection can be seen for high drive strength and long drive in the upper right corner of Fig. 11(b): the reason is the dimensionality of the Hilbert space of the phonon system (N_{ph} for this simulation) not being enough. To compare the qubit population for the same amplitude α, focus on the upper right corner of Fig. 11(a). That corresponds to an $\alpha \approx 5$ and in the plot below to a residual qubit population of $\langle\hat{\sigma}_z\rangle \approx 0.06$. The same α on the right plot coincides with a qubit population of $\langle\hat{\sigma}_z\rangle \approx 0.12$, double the first case. Hence, it is better to drive at further away detunings, as it induces less excited state population in the qubit. Practically speaking, limitations are the pulse amplitude needed, that becomes higher and higher, and the frequency shape of the pulse, that can overlap with undesired transitions.

4.1.2 Parity measurements in the dispersive regime

The strong dispersive regime for the qubit-phonon mode system described in section 3.3.1 allows the qubit to be spectroscopically resolved at different frequencies depending on phonon population. Thus far, this effect has been considered only in the frequency domain. However, it is possible to analyze this behaviour also in time domain by carrying out measurements on the qubit based on Ramsey sequences. The exact calculation of the qubit state population at the end of the sequence for whichever initial phonon state is reported in Appendix B.2. To calibrate parity measurements preparation of different fock states is needed. The control sequence is shown in Fig. 12(a). The frequency above each stark shift pulse indicates the tuned qubit frequency during the pulse. As expected from the dispersive hamiltonian in the two level system approximation

$$H_{disp} = \hbar\frac{\chi}{2}\hat{b}_k^\dagger\hat{b}_k\hat{\sigma}_z \ , \tag{4.3}$$

the prepared fock state $|n\rangle$ contributes to a frequency shift of the qubit of $n\chi$. This means that when calibrating and canceling the phase accumulated by the qubit during the dispersive evolution, the frequency of the qubit population is just $\omega_{pop} = n\chi$. For the usual parameters, the simulation is revealed in Fig. 12(b). The origin of the high frequency oscillations is elucidated in Appendix B.1. Ideally, the measurements of the parity occur at an ideal time $t_{int} = \pi/\chi$, indicated by the black dashed line. At that point, prepared even fock states correspond to an excited state population, while odd fock states correspond to a ground state population. It is possible to define a contrast to quantify how far away from

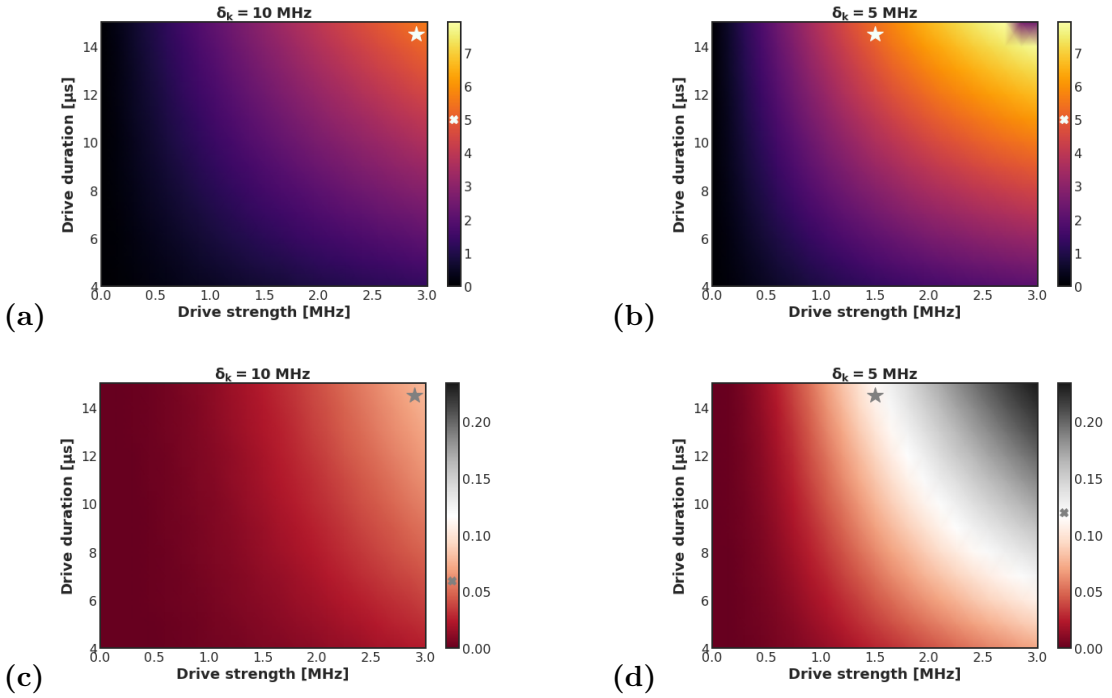

Figure 11: Amplitude α of the coherent state generated as a function of drive strength and drive duration for two different detunings $\delta_k = 10$ MHz (a) and $\delta_k = 5$ MHz (b). Qubit population $\langle \hat{\sigma}_z \rangle$ for the same parameters in (c) ($\delta_k = 10$ MHz) and (d) ($\delta_k = 5$ MHz)). Stars represent points with same α and same corresponding detuning on the plots below. Crosses indicate the respective amplitudes of the stars on the colorbars. For these simulations the dimensions of the Hilbert space of the fock system $N_{ph} = 90$ have been used.

ideality the parity measurements are in the following way

$$C = \sum_{n=0}^{n_{max}} |0.5 - \langle \hat{\sigma}_z \rangle (t_{int})| \ , \tag{4.4}$$

with n_{max} the highest fock state $|n_{max}\rangle$ taken into account in our contrast. A normalized contrast symbolizes the precision of the measurements $C_{norm} = C/(n_{max}+1)$. Ideally each fock state has a contrast of 0.5. Including decoherence, without the dispersive regime imperfections the expression of eqn. (4.4) is found by substituting an exponential decay with characteristic time T_2

$$C_{th} = \frac{(n_{max}+1)}{2}\left(1 - e^{-\frac{t_{int}}{T_2}}\right) \ , \tag{4.5}$$

with C_{th} meaning theoretical contrast. When no losses are present, canceling out the exponential yields an ideal value of 0.5 for each different Fock state. In Fig. 12(c) simulations of the contrast for different coherence times are shown. The simulated values approximate precisely the theoretical curve. The only difference can be noticed for high coherence times, where the imperfection effect of the dispersive regime is significantly more appreciable than the dephasing effect of the qubit. Another analysis is presented in Fig. 25(d), where g^2/δ_k is set to constant and consequently the interaction time $t_{int} \approx 7.48$ µs. The coherence times are set to $T_1, T_2 = 30$ µs for each point of the plot. Simulations display that the contrast always increases for higher detuning and, consequently, higher coupling. The results mentioned have a vigorous impact for the future of cQAD based devices. In fact, given higher qubit-phonon coupling for the same coherence times, there always exists a new interaction point such that the contrast of the parity measurements increases.
Another meaningful investigation consists in simulating the contrast of eqn. (4.4) up to $n_{max} = 3$ as a function of qubit-phonon coupling g and interaction detuning δ_{int}. The resulting 2-dimensional plot is pictured in Fig. 13. The behaviour of the contrast generally follows expectations. In fact, for low couplings and high detunings the contrast is very low due to long interaction times, while as the coupling increases the contrast increases. Surprising is the fact that for the device parameters chosen (the same as the measured ones of Table 1) choosing a lower detuning always improves the contrast. The resulting implication is that, for current qubit coherence, fast interaction is more dominant than not being perfectly in the dispersive regime. However, issues not related to contrast arise, especially phase-related, as is explained in section 4.2.2. These problems generate the oscillating pattern in the middle of the figure. Lastly, in the plot it can be noticed that diagonal lines of similar contrast can be shown. The lines correspond to the plot of Fig. 12(d), with g^2/δ_{int} constant.

4.1.3 Displaced parity measurements

Wigner functions represent a way of characterizing a state by its tomography in phase space. Their expressions, properties and some examples are listed in Appendix A. In a cQAD system, it is possible to perform state tomography with displaced parity measurements by applying a displacement for each point α in phase space and subsequently implementing the Ramsey segment of the parity measurement control sequence. The dispersive regime imperfections due to the high g/δ_k The simulated Wigner functions of $|0\rangle$, $|1\rangle$ and $|2\rangle$ are compared in Fig. 26 with the ideal and measured states. The most evident difference with the ideal states is the presence of a negative background, due to dispersive regime imperfections. Furthermore, the contrast in the parity is lower than the ideal case due to decoherence. Characterization of the states is achieved by quantifying a fidelity measure $\mathcal{F}$. For

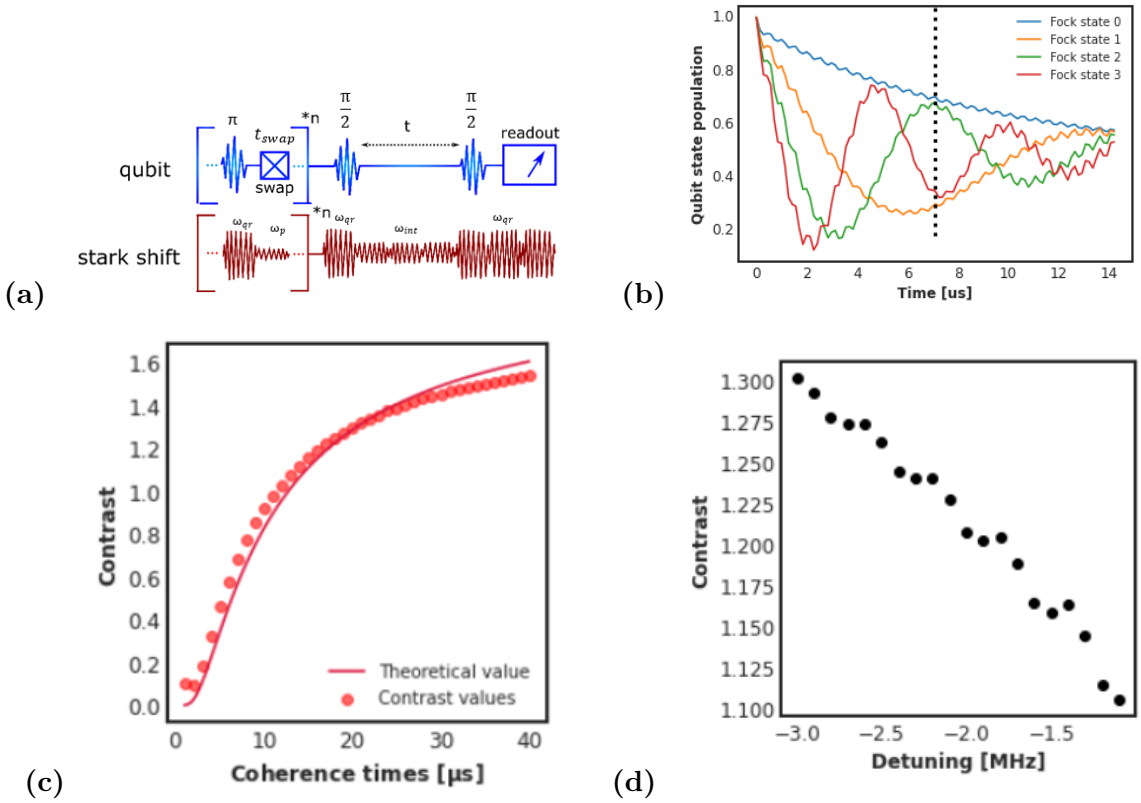

Figure 12: (a), Parity measurements calibration control sequence for qubit and stark shift pulse. ω_{qr} is the qubit rest frequency, ω_p is the phonon frequency, ω_{int} is the qubit interaction frequency and t_{swap} is the excitation swap time between qubit and phonon. (b), Ramsey sequence for the qubit after preparing fock states $|0\rangle$, $|1\rangle$, $|2\rangle$ and $|3\rangle$. The dashed line represents the interaction time $t_{int} = \pi/\chi$. (c) Simulated contrast (eqn. (4.4)) of parity measurements as a function of coherence times. Red dots are simulated values, while the red line is the theoretical estimate of eqn. (4.5). (d) Simulated contrast (eqn. (4.4)) as a function of qubit-phonon detuning δ_k. The ratio g^2/δ_k, and subsequently the interaction time $t_{int} = \pi/\chi$ is kept constant.

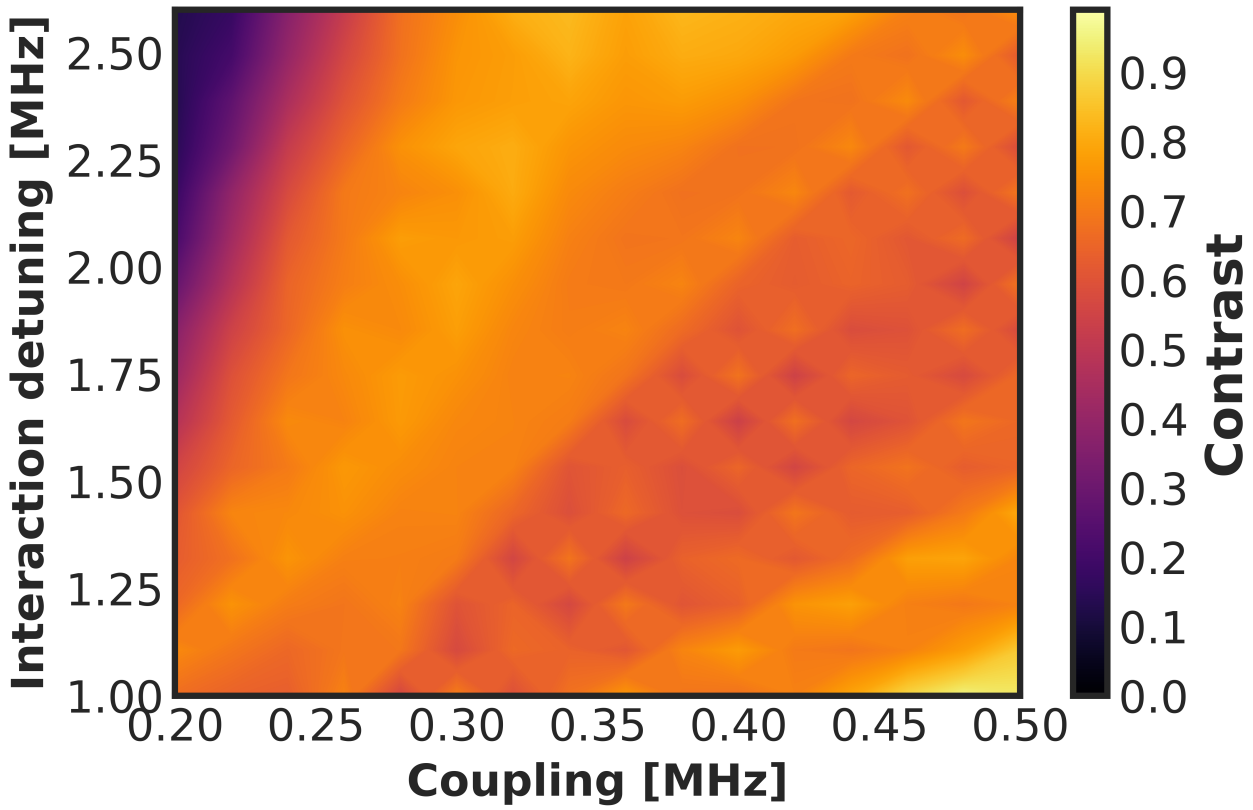

Figure 13: Contrast of eqn. (4.4) up to $n_{max} = 3$ as a function of qubit-phonon coupling g and interaction detuning δ_{int}.

density matrices, the fidelity has already been defined in eqn. (4.2). A viable approach to characterize the fidelity of a state would be to reconstruct the density matrix given enough points in phase space and employ the fidelity formula. However, another manner is chosen using a property of Wigner function from Appendix A.2. The expression of eqn. (A.10) allows to calculate the overlap of two Wigner functions as an integral of their product

$$\pi \int_{-\infty}^{+\infty} W_1(x,p)\, W_2(x,p)\, dx\, dp = Tr[\hat{\rho}_1 \hat{\rho}_2] \ , \tag{4.6}$$

for two Wigner functions $W_1(x,p), W_2(x,p)$ related to two density matrices $\hat{\rho}_1, \hat{\rho}_2$. The equation can be written for a finite number of points assuming the Wigner functions to be defined over a grid along the x and y axis

$$\begin{aligned} \mathcal{F} = \pi \frac{x_{max} - x_{min}}{x_{steps}} \frac{y_{max} - y_{min}}{y_{steps}} \frac{x'_{max} - x'_{min}}{x'_{steps}} \frac{y'_{max} - y'_{min}}{y'_{steps}} \\ \sum_{x=x_{min}}^{x=x_{max}} \sum_{y=y_{min}}^{y=y_{max}} \sum_{x'=x'_{min}}^{x'=x'_{max}} \sum_{y'=y'_{min}}^{y'=y'_{max}} W(x,y) W'(x',y') \ , \end{aligned} \tag{4.7}$$

for two Wigner functions $W(x,y)$ and $W'(x',y')$ corresponding to two density matrices $\hat{\rho}$ and $\hat{\rho}'$. x_{min} and x_{max} represent the minimum and maximum extrema of the x-axis over which the Wigner $W(x,y)$ is defined, while x_{steps} are the number of points in the x direction. Same thing for y_{min}, y_{max} and y_{steps} for the y-axis and analogously substituting with x', y' for $W'(x,y)$. When simulating or measuring the Wigner function through parity measurements, a normalization to amplitude must be executed: $W(x,y) = \frac{2}{\pi} W_p(x,y)$, with $W_p(x,y)$ the measured displaced parity.

4.2 Full cat simulations

Thus far, the topic of the discussion has been the achievement of state characterization through its different steps in a cQAD system. The objective of this section is to combine the cat state protocols listed in chapter 2 with state tomography. Parameter sweeps and protocol analysis provides insights about how to maximize fidelities of the state created. More specifically, understanding several control parameters for the resonant cat is crucial for the measurements of chapter 5. Analysis of the other two cat protocols is needed for possible future measurements on the same device or better devices.

4.2.1 Resonant cat

The resonant cat state expression, derived in section 4.2.1, is an approximated cat state. For this reason, a rigorous benchmark for how much of a cat the protocol has generated must be defined. To find the fidelity of a cat state the following expression is employed

$$\mathcal{F}_{cat} = max_{\hat{\rho}_{cat}}(\mathcal{F}(\hat{\rho}_{cat}, \hat{\rho}_{res})) \ , \tag{4.8}$$

with $\hat{\rho}_{cat} = |\psi_{cat}\rangle\langle\psi_{cat}|$ and ψ_{cat} defined as

$$\psi_{cat} = \frac{1}{N_\theta} \hat{D}(\alpha_d e^{i\theta_d})(|\alpha e^{i\theta_s}\rangle + e^{i\theta}|-\alpha e^{i\theta_s}\rangle) \ , \tag{4.9}$$

with the generalization of the normalization factor of eqn. (A.20) N_θ

$$\mathcal{N}_\theta = 2(1 + e^{i\theta} e^{-2|\alpha|^2}) \ . \tag{4.10}$$

Five parameters are present in eqn. (4.9): α, the coherent state amplitude of each blob of the cat, α_d, an offset displacement to the full cat state, θ_d, the phase of this displacement, θ_s, the phase of the coherent state blobs and θ the phase between the two coherent state. The α used is the same as the alpha fitted after coherent state creation. An offset displacement is supposed due to imperfection in resonant cat generation. θ_s is necessary due to measurement in a different rotating frame with respect to the phonon mode. Simulations show that the relative phase θ depends on the initial state of the qubit.

Resonant cat for different sizes

The cat state protocol employed in the simulations operates in the following way: a coherent state is driven in the phonon mode to create an $|\alpha\rangle$ state. Afterwards, a π pulse on the qubit is applied and eventually the qubit and phonon are put on resonance interacting for a time $t_{int} = t_r/2 = \alpha\pi/g$. The state generated resembled a cat state as $\overline{n} = |\alpha|^2 \to \infty$. The affinity is exhibited in Fig. 14(a-d), with increasing amplitudes $\alpha = 1, 1.2, 1.5, 2$. The corresponding fidelities are $\mathcal{F} = 0.597, 0.703, 0.646, 0.495$. The ideal fidelity trends towards one as the largeness of the cat state increases. However, due to included losses depending on $1/\alpha^2$, the actual values reach a maximum and plummet. These trends can be deduced from Fig. 15. As a function of the coherent state amplitude α, the fidelity with an ideal SCS is plotted with losses of both qubit and phonon mode and without any losses. The ideal case displays a sharp increase in fidelity after $\alpha \approx 1$. However, at $\alpha \approx 1.4$, the fidelity value decreases and reaches a stable value, attributed to the balance between the imperfection due to higher qubit losses as the coherent drive amplitude increases, and the resemblance of the resonant cat to a SCS. The case with losses shows a similar trend, despite with a parabolic envelope, caused by the losses dependent on the amplitude α, as already mentioned. The dependence of the fidelity of alpha provides a calibration mechanism to select the best α for our experiment and simulations. The values chosen are $\alpha \approx 1.4 - 1.5$, a tradeoff between high fidelity and large enough mean phonon number $\overline{n}$.

Adding parity measurements

After state creation, implementation of displaced parity measurements in simulations has been achieved. In the previous paragraph, qubit coherence had an effect only on state creation. Here, the effect of coherence losses is investigated additionally during measurements. Preserving the same device parameters and fixing $\alpha = 1.5$, the measurement sequence is simulated for different qubit coherence times of $T_{1q}, T_{2q} = 12, 16$ µs, shown in in Fig 16(a); $T_{1q}, T_{2q} = 25, 32$ µs, shown in in Fig 16(b); $T_{1q}, T_{2q} = 38, 48$ µs, shown in in Fig 16(c). Two figures of merit are defined to calibrate the "closeness" of the measured states to a cat state: $\mathcal{F}_1$ and $\mathcal{F}_2$. $\mathcal{F}_2$ is defined as in eqn. (4.8) as the fidelity of the resonant cat density matrix at the end of state generation with the fitted cat $\hat{\rho}_{cat}$ inducing the highest fidelities. While $\mathcal{F}_1$ is defined as in eqn. (4.7) as the fidelity of the resonant cat Wigner function after measurement with the best fitted cat found for $\mathcal{F}_2$. The measurement process only adds imperfections, but does not change the parameters of eqn. (4.9). The values of the fidelities increase for higher coherence times, as expected. The ratio $\mathcal{F}_1/\mathcal{F}_2$ can also be computed. The value of this quantity stays constant to an approximate value of $\approx 2/3$ for the different cases, implying that coherence times affect state generation and the measurement sequence with the same proportion. The quantities mentioned are displayed in Table 2.
Two main things jump to the eye when observing the simulated Wigner tomographies. The first is the contrast of the blobs and fringes, increasing with better qubit coherence times, because of higher contrast parity measurements. The second is the offset background, vary-

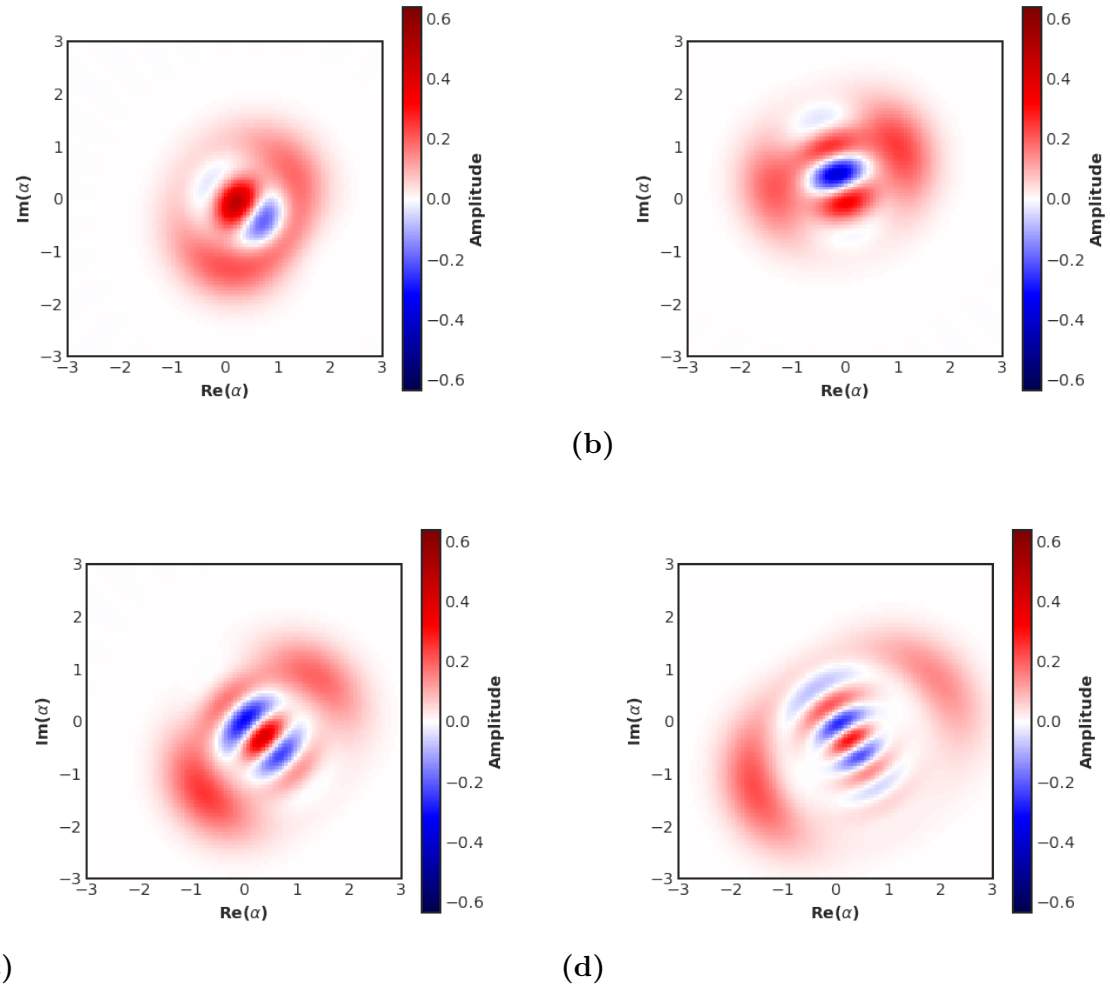

Figure 14: Simulation of the resonant cat protocol without state tomography for the usual device parameters for different amplitudes α. (a) $\alpha = 1$ with fidelity to an ideal cat state of $\mathcal{F} = 0.597$, (b) $\alpha = 1.2$ with fidelity $\mathcal{F} = 0.703$ (c) $\alpha = 1.5$ with fidelity $\mathcal{F} = 0.646$, (d) $\alpha = 2$ with fidelity $\mathcal{F} = 0.495$. Losses are set to $T_{1q} = 10.1$ µs, $T_{2q} = 8.8$ µs, $T_{1p} = 42$ µs and $T_{2p} = 77.5$ µs.

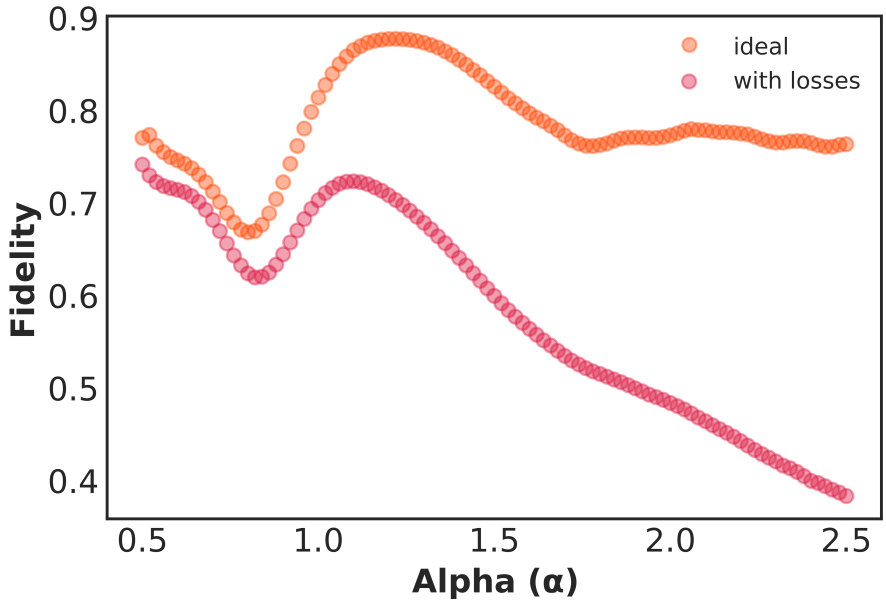

Figure 15: Fidelity of a resonant cat with a fitted ideal SCS as a function of the amplitude α of the size of the coherent state created. The two lines represent the case without any losses (orange) and with qubit and phonon losses (red). The losses for the red case are the same as in Table 1.

Parameter	Case 1	Case 2	Case 3
Qubit coherence times T_{1q}, T_{2q} [µs]	$12, 16$	$25, 32$	$38, 48$
Fidelity $\mathcal{F}_1$	0.272	0.393	0.444
Fidelity $\mathcal{F}_2$	0.407	0.590	0.701
Ratio $\mathcal{F}_2/\mathcal{F}_1$	0.668	0.667	0.633

Table 2: Simulation results for resonant cat Wigner tomography as a function of coherence times. Parameters are mostly from Table 1, except for $T_{1p} = 42$ µs, $T_{2p} = 77.5$ µs, $\omega_{qr} = 5.956115$ GHz and $\omega_{qi} = 5.972115$ GHz.

ing for the three plots. The offset background is present due to higher order terms in the dispersive regime (see Appendix B). In particular, the theoretical time $t_{int} = \pi/\chi$ set for the interaction time of the ramsey sequence is not ideal, due to the presence of residual JC interaction. Varying the interaction time changes the background offset [1]. Due to very long simulation times (multiplied by four due to four phase averaging as described in Appendix B.3), this interaction time is set to the ideal value. Thus, the background value depends on the particular parameters of the simulation, including coherence times and can be negative (Fig. 16(a)), positive (Fig. 16(b)) or close to zero (Fig. 16(c)).

4.2.2 Heralded cat

The heralded cat is prepared in exactly the same way as in section 2.3. Transferring the pulses to the simulator the protocol unfolds as expected. After applying the necessary gates, measuring the qubit state collapses the cat state either in the odd cat state in case of a qubit measured in the ground state, or an even cat state if the qubit is measured in the excited state. The fidelities for the simulated protocols for ideal parameters can even reach

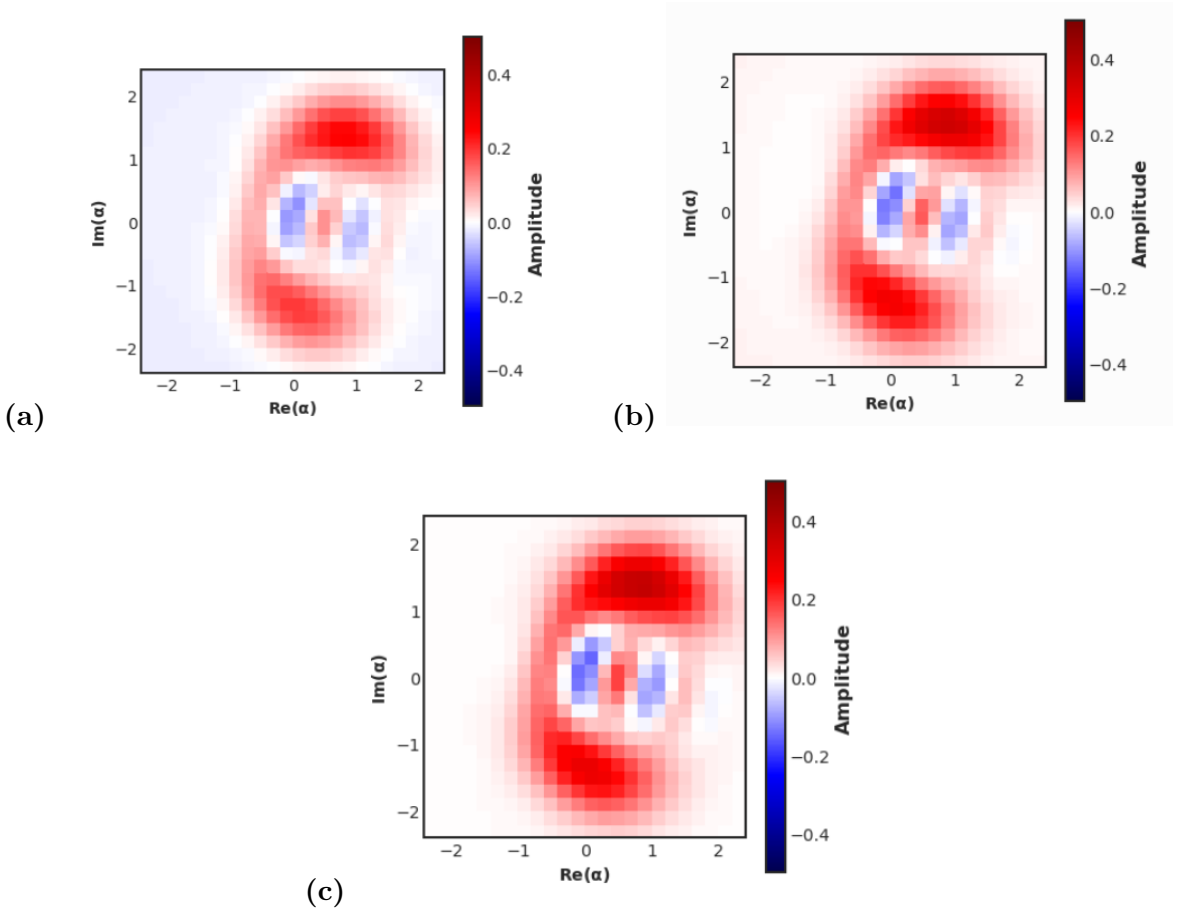

Figure 16: Resulting Wigner function from state generation and displaced parity measurements of the resonant cat protocol for $\alpha = 1.5$. Square symmetric grid is composed by n x n simulated measurements with $n = 25$ with $x_{max} = 2.4$. Other parameters are from Table 1 with some changes written in Table 2. Plots differ by qubit decay time T_{1q} and qubit decoherence time T_{2q}. Phonon coherence times are set to $T_{1p} = 42$ µs and $T_{2p} = 77.5$ µs. (a) $T_{1q} = 12$ µs, $T_{2q} = 16$ µs. (b) $T_{1q} = 25$ µs, $T_{2q} = 32$ µs. (c) $T_{1q} = 38$ µs, $T_{2q} = 48$ µs.

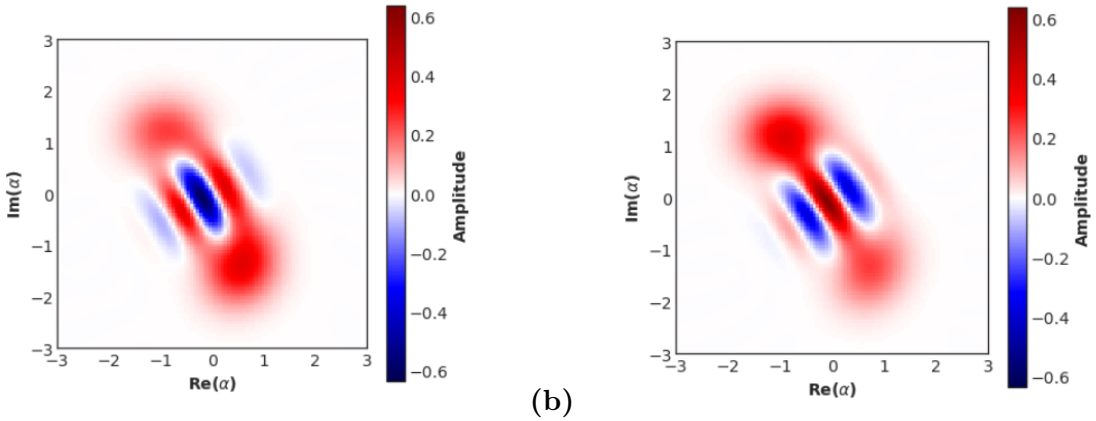

Figure 17: Heralded cats for usual device parameters except for coherence times, set to a very large value. (a) displays $|\psi_{cat}\rangle_+$ with fidelity $\mathcal{F}_+ = 0.9802$. (b) displays $|\psi_{cat}\rangle_-$ with fidelity $\mathcal{F}_- = 0.9768$.

$\mathcal{F} = 0.98 - 0.99$, defined as in eqn. (4.8). Plots of the Wigner function are displayed in Fig. 17(a) for the even cat, and in Fig. 17(a) for the odd cat. The calculated fidelities in this case are respectively $\mathcal{F}_+ = 0.9802$ and $\mathcal{F}_- = 0.9768$.
The exact values of the fidelities depend on the relative phase θ of the qubit superposition dependent on the phase of the $R_\theta\left(\frac{\pi}{2}\right)$ gate. This behaviour can be seen in Fig. 18(a), where the odd cat of the protocol is plotted for a particular initial relative phase θ. A strong asymmetry in the coherent state blobs can be noticed. In fact, by varying the phase θ, simulations show that a sinusouidal oscillation in the coherent state blob asymmetry is present. The dependence is assumed to be attributed to higher terms in the dispersive Hamiltonian. This assumption is supported by Fig. 18(b), where odd and even SCSs state fidelities are plotted as a function of qubit-phonon coupling g. Oscillations in the fidelity are present, with a frequency proportional to g^2, and subsequently to the interaction time π/χ. Hence, the oscillation frequency decreases as g goes up. Theoretically extending the plot to extremely large couplings, it is possible to imagine that the frequency of the oscillations in fidelity is so low that there is no dependence of the fidelity on g.
After state creation, displaced parity measurements can be simulated for the given state. Sweeping coherence times returns fidelity values similar to Table 2. To gain new insights, coupling is varied as a sweeping parameter, simulating different piezoelectric materials for qubit-phonon interaction. Fig. 18(b) has already shown the SCSs dependance on coupling, with a small increasing envelope for higher values of g. When including parity measurements, the fidelity quantities used are $\mathcal{F}_1$, $\mathcal{F}_2$ and $\mathcal{F}_2/\mathcal{F}_1$ defined in subsection 4.2.1, reported in Table 3. The ratios are quite constant as well, except for coupling 0.6, for which the dispersive regime is not a good approximation $g/\delta_k \approx 1/3$. Furthermore, fidelities $\mathcal{F}_2$ are higher than the resonant counterparts due to the final state being ideally a SCS.
A further useful dependence to show is the shift of the "best" interaction point for the qubit as the coherence times increase. "Best" referes to the highest fidelity for the fitted SCS. If coherence times are low, a short interaction time t_{int} allows better fidelities. However, as coherence times increase, the best interaction point shifts further and further away, as having a better dispersive approximation is preferred. The interaction point dependence is shown for different coherence times of $T_{1q}, T_{2q} = 16, 20$ µs in Fig. 19(a), $T_{1q}, T_{2q} = 48, 60$ µs in Fig. 19(b), $T_{1q}, T_{2q} = 100, 120$ µs in Fig. 19(c), $T_{1q}, T_{2q} = 200, 240$ µs in Fig. 19(d). The fidelity oscillations and amplitude depend on the detuning of the qubit-phonon system dur-

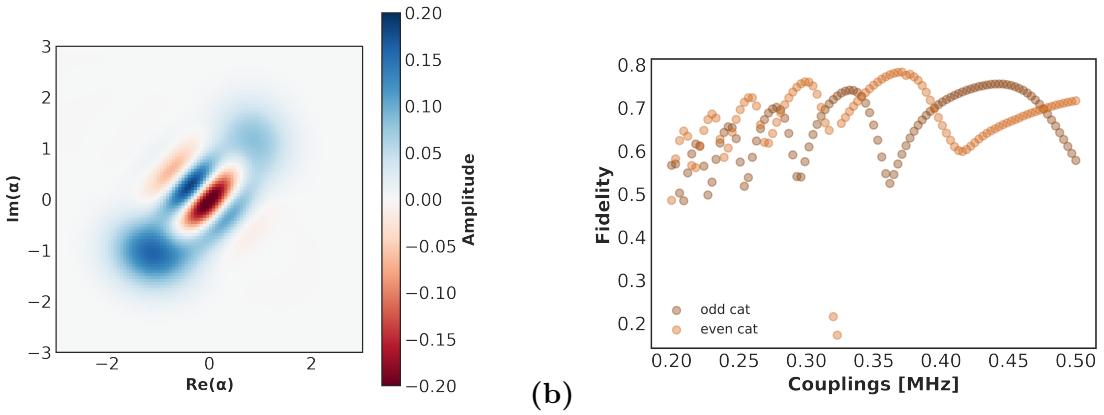

Figure 18: (a) Odd SCS of the heralded cat protocol simulated for a particular angle θ of the $R_\theta\left(\frac{\pi}{2}\right)$ gate. Particularly interesting is the asymmetry of the coherent state blobs. Parameters are the same as Table 1, except for losses which are removed to isolate the asymmetry issue. (b) Fidelity of both odd and even SCSs of the heralded cat protocol as a function of coupling. Oscillations of the fidelity periodic with g^2 can be noticed for both states.

Parameter	Case 1	Case 2	Case 3
Coupling [MHz]	0.2	0.4	0.6
Fidelity $\mathcal{F}_1$	0.372	0.343	0.292
Fidelity $\mathcal{F}_2$	0.830	0.771	0.853
Ratio $\mathcal{F}_2/\mathcal{F}_1$	0.448	0.445	0.342

Table 3: Simulation results for the even heralded cat Wigner tomography as a function of couplings. Parameters are mostly from Table 1, except for $T_{1q} = 25$ µs, $T_{2q} = 29$ µs, $T_{1p} = 60$ µs, $T_{2p} = 100$ µs, $\omega_{qr} = 5.9691$ GHz and $\omega_{qi} = 5.9721$ GHz.

ing the interaction time and the relative phase of the superposition state created, as already mentioned earlier.

4.2.3 qcMAP

The qcMAP sequence has been described in subsection 2.4. However, executing the exact protocol does not function as intended. The reason being that the phonon drive corresponds to a displacement which is conditional to the qubit state. A short derivation of the new expression with cQAD parameters is found in Appendix D. The protocol actually takes less time now, because the dispersive evolution is not anymore needed. In the control sequence of Fig. 5, the $S\left(\frac{\pi}{\chi}\right)$ operation is then removed. The third step is replaced by

$$\hat{D}_\theta \frac{1}{\sqrt{2}}(|g\rangle + |e\rangle) \otimes |\alpha\rangle = \frac{1}{\sqrt{2}}(|e,0\rangle + |g,2\alpha\rangle) \ , \tag{4.11}$$

where $\hat{D}_\theta$ is the displacement depending on the qubit state $R_x(\phi)|g\rangle$. The expression at the end of eqn. (4.11) after tracing out the qubit state is shown in Fig. 20(a). The two blobs have no interference fringes, as expected. Imperfections can be seen due to higher order terms in the second drive pulse. Conditional π pulse $R_x^0(\pi)$ can be performed by exploiting the dispersive regime and consequent phonon number splitting. Its operation consists in applying a long enough drive pulse to select just the qubit state entangled with Fock

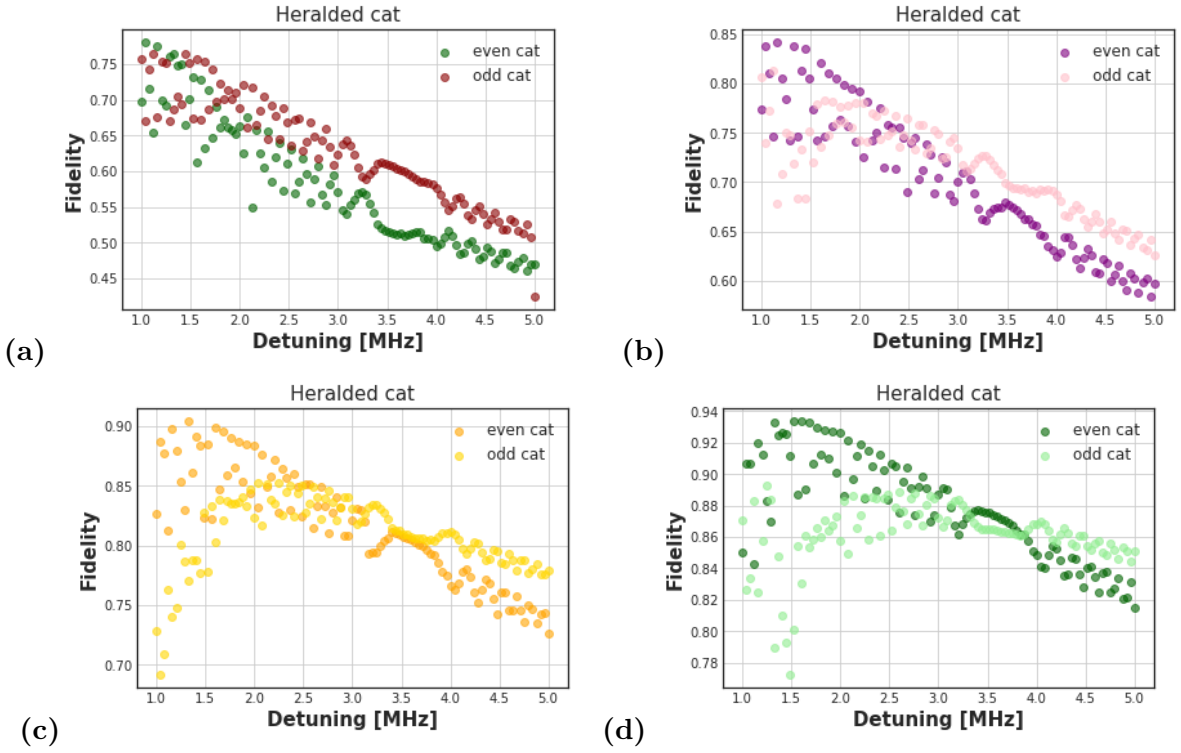

Figure 19: Fidelities of both even and odd cats generated with the heralded cat protocol as a function of interaction detuning δqi for different coherence times. (a) $T_{1q}, T_{2q} = 16, 20$ µs, (b) $T_{1q}, T_{2q} = 48, 60$ µs, (c) $T_{1q}, T_{2q} = 100, 120$ µs in Fig. 19, (d) $T_{1q}, T_{2q} = 200, 240$ µs. Other parameters are from 1, except for phonon coherence times $T_{1p} = 100$ µs, $T_{2p} = 140$µs for (a) and (b), $T_{1p} = 200$ µs, $T_{2p} = 240$µs for (c) and $T_{1p} = 400$ µs, $T_{2p} = 480$µs for (d).

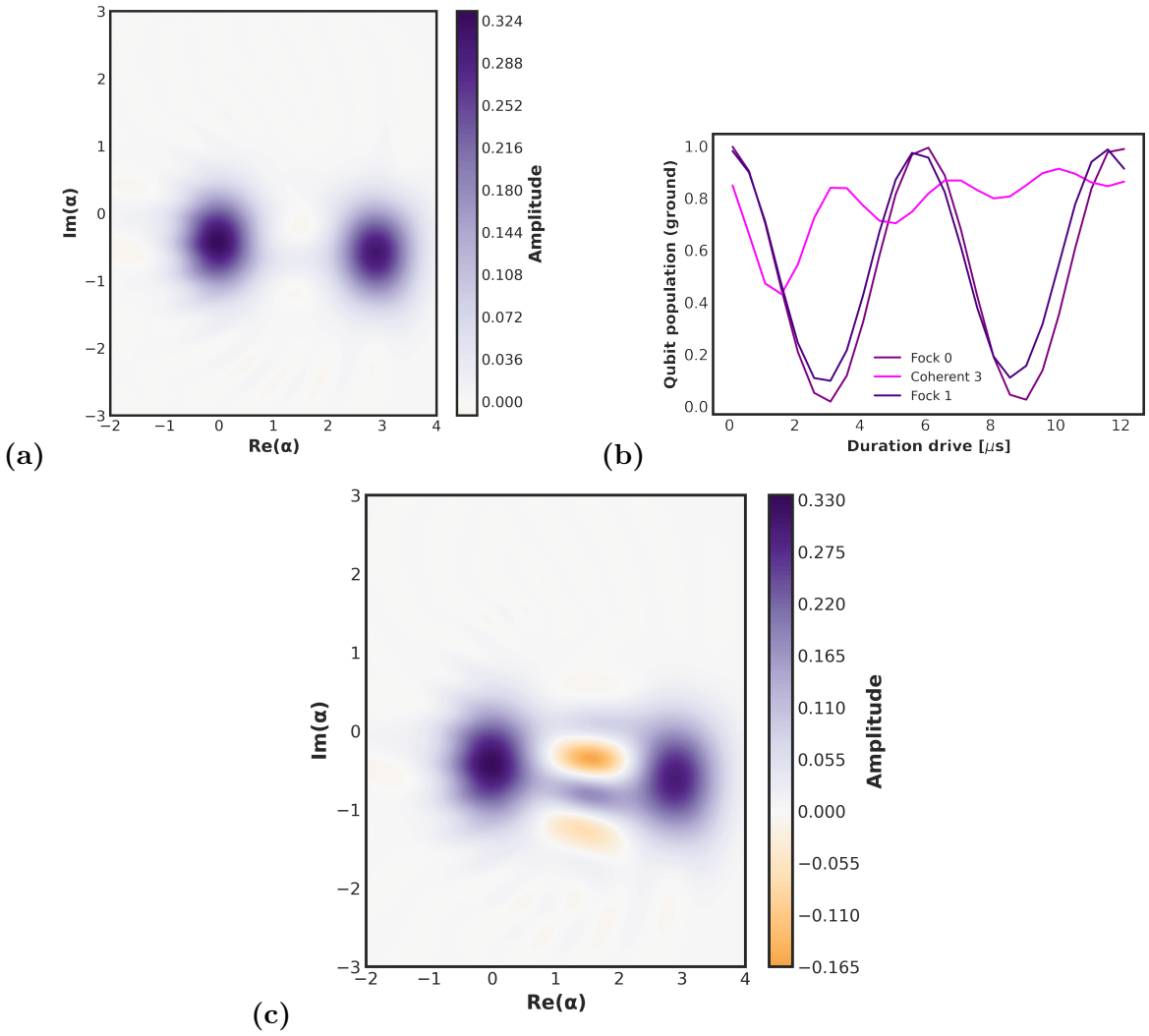

Figure 20: (a) Wigner tomography of the final expression of eqn. (4.11) after tracing out the qubit. (b) Ground state population of qubit state for phonon initial states fock $|0\rangle$, fock $|1\rangle$ and coherent $|\alpha\rangle$ with $\alpha = 3$. (c) Final state of the qcMAP protocol. Qubit coherence times have been set to ∞. Parameters are from Table 1, except from rest point $\omega_{qr} = 5.952117$ GHz.

number $|0\rangle$. In Fig. 20(b), the action of such a pulse over time is shown. The qubit state population of the qubit state entangled with the Fock $|0\rangle$ state follows Rabi oscillations, as expected from the a normal drive interaction. As a reference, the case when it is entangled to the Fock $|1\rangle$ state is plotted, showing Rabi oscillations with clipped amplitude due to the detuned frequency of χ. In the case of a coherent state of amplitude $\alpha = 3$ (which corresponds to double of the target coherent state amplitude $\alpha = 1.5$), oscillations are very faint. Less than 0.2 of the qubit population in this case is excited for a time of only $t_\pi \approx 3$ µs. Better parameters could reduce the undesired qubit population and the drive duration. The effect of the $R_x^0(\pi)$ pulse on the state of eqn. (4.11) produces an even cat state, as shown in Fig. 20(c). The fidelity for this state is $\mathcal{F} = 0.6312$, for no losses included. Despite the reduced protocol, fringes are not visible for simulations with the parameters of our device. More careful simulations have the potential to slightly improve state fidelities. However, better device parameters such as qubit losses and qubit-phonon coupling are needed to increase state fidelity.

5 Experiments

Adopting a kitten

"It doesn't matter how beautiful your theory is, it doesn't matter how smart you are. If it doesn't agree with experiment, it's wrong."
Richard P. Feynman

The article [1] has been able to prove that the device is in the strong dispersive regime of cQAD by showing phonon number splitting. Furthermore, parity measurements in the dispersive regime, described in subsection 4.1.2 and shown again in subsection 5.2.3, have been performed. The goal of this experiment is to recalibrate all necessary steps and implement the resonant cat protocol. Most of the calibrated parameters have been already mentioned in 1, because they are the ones mostly adopted for simulations after performing the measurements for better comparison. In section 5.1 the measurement setup is described. After that, step by step calibration is needed in section 5.2, beginning with qubit properties (subsection 5.2.1), phonon properties and coherent state calibration (subsection 5.2.2) and Ramsey-like parity measurements (subsection 5.2.3). The experiments end up with state tomography through Wigner function measurements in section 5.3, with both quantum and quasi-classical states (subsection 5.3.1) and the resonant SCS (subsection 5.3.2). In this last subsection, collapse and revival of Rabi oscillations are shown for different coherent state amplitude α to prove qubit cavity interaction.

5.1 Measurement setup

The measurement setup is shown in Fig. 21. The device sits in a dilution refrigerator (denoted by "Fridge") at the base temperature stage. The schematic shows the key electronic tools to control it. As a substitute for an Arbitrary Waveform Generator (AWG) the Quantum Machines Operator-X (OP-X) is employed. This device allows to send qubit pulses and to perform readout. One I-Q channel pair is used to control the qubit and the phonon modes. The Local Oscillator (LO) frequency from a Windfreak SynthHD (WF) at a detuning $\delta_{qIF} = \omega_{qr} - \omega_{qLO} = 50$ MHz ($\omega_{qLO} = 5.91994$ MHz) from the qubit rest frequency upconverts the Intermediate Frequency (IF) of the I-Q pair up to the desired qubit or phonon frequency. Another I-Q channel pair is dedicated to readout the cavity frequency and performing the stark shift. In this case the Rohde & Schwarz (R&S) signal generator is needed to upconvert the IF frequency whose value is $\delta_{rIF} = \omega_r - \omega_{rLO} = 250$ MHz ($\omega_{rLO} = 7.762$ MHz), with ω_r the cavity frequency. Through the same channel a different waveform is sent at $\omega_{ss} = 180$ MHz (70 MHz away from the cavity frequency) for the stark shift. Afterwards, the two Radio Frequency (RF) upconverted signals from the mixers are combined through a Directional Coupler (Dir Coup) with a -20dB in power on the qubit signal. This device ensures that the signals are unidirectional and do not undermine the linearity of the mixers. Another directional coupler channels part of the signal to a Spectrum Analyzer (SA), important for debugging and mixer calibration (not performed in this case for time constraints). The output of the fridge, after an initial amplification stage at the base stage with an Superconducting nonlinear asymmetric inductive element (SNAIL) Parametric Amplifier (SPA) [53] and a High-Electron-Mobility Transistor (HEMT) at the 4K stage, is amplified first with a 20 dB amplifier and after with two 7 dB amplifiers. Eventually, this signal is downconverted with a Image Reject mixer and read out by the OP-X. To downconvert the output signal the same R&S is used thanks to a splitter, such that LOs with the same phase can be used for input and output. The last two instruments are a Direct Current (DC) source to bias the SPA through a magnetic flux, and an SPA pump necessary for the three-wave mixing amplifying properties of the SNAIL. However, the SPA

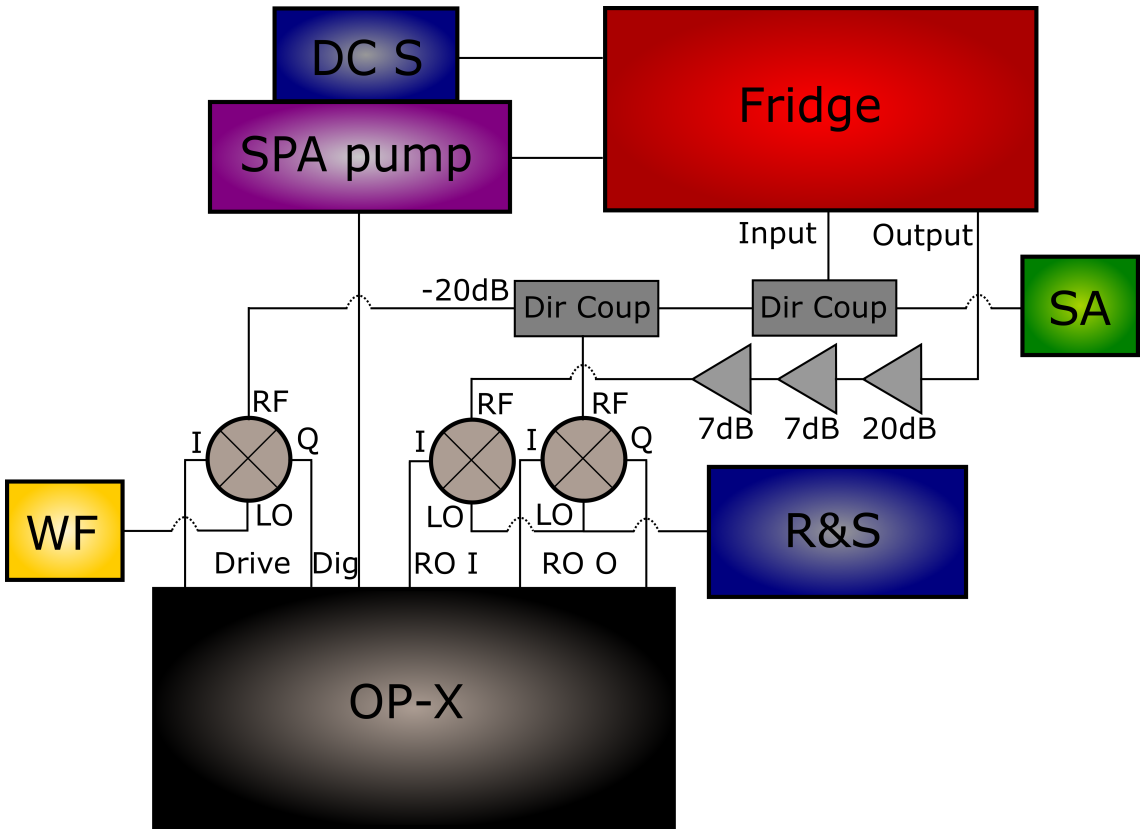

Figure 21: Measurement setup for the experiment. Control electronics and connections are shown. The circle with the two crosses represent IQ mixers, while the triangular shaped components represent amplifiers. Meaning of the abbreviations: "Dig": Digital line, "Dir Coup: Directional Coupler, "RF": Radio Frequency, "LO": Local Oscillator, "R&S": Rohde & Schwarz, "WF": Windfreak, "SA": Spectrum Analyzer, "DC S": Direct Current Source, "OP-X": Operator-X, "SPA": Snail Parametric Amplifier, "RO I/RO O": Readout Input/Output More details in main text.

pump populates the cavity, increasing its average photon number. As a solution for this, it is advised to activate the SPA pump only when reading out. When sending the readout pulse, the OP-X can be set to send a digital trigger such that the SPA pump outputs synchronously with the cavity probe tone. This time is set to the readout pulse length of the OP-X.

5.2 Device calibration

The calibration begins with cavity spectroscopy. Due to our readout structure based on transmission, the feature displayed by the resonator is a peak, because the signal is amplified at the resonance frequency $\omega_r = \frac{1}{\sqrt{C_r L_r}}$ For that, ω_{rIF} is tuned over a small interval around the predicted frequency. The result is shown in Fig. (a). The plots show as the amplitude the raw values $\sqrt{|I|^2 + |Q|^2}$. It is also possible to normalize the values by the qubit ground state and excited state values. Fitting the cavity peak, parameters can be derived such as the frequency ω_r, equal to 8.012 GHz, and the linewidth γ_r, equal to $\kappa = 496$ kHz, which is the Full Width at Half Maximum (FWHM) of the peak. Introducing the fitting function is convenient because all of the peaks (qubit, phonon and cavity related) are ap-

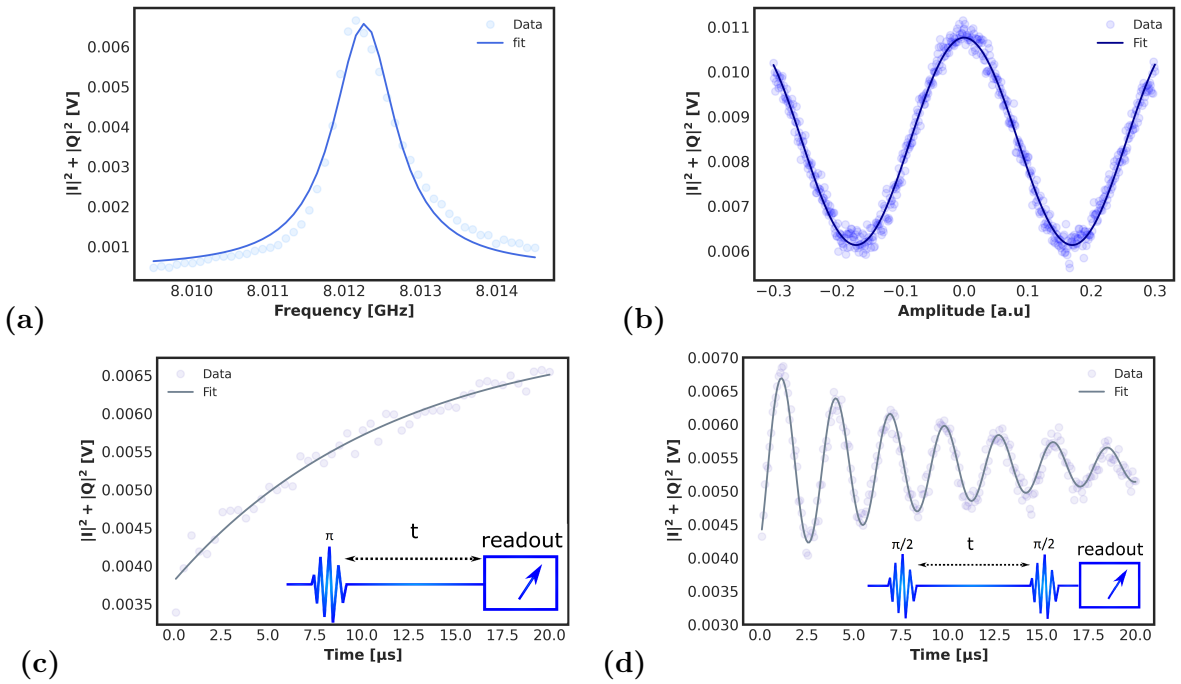

Figure 22: Initial calibration of our device. In (a) cavity spectroscopy can be seen. The peak is fitted to a Lorentzian function. In (b) qubit Rabi oscillations are shown. In (c) and (d) a qubit T_1 and T_2 measurement with their respective control sequences are shown. Values: $\omega_r = 8.012$ GHz, $\gamma_r = 496$ kHz, $T_1 = 10.2$ µs, $T_2 = 8.8$ µs, $V_\pi = 0.085$ V.

proximated to have a Lorentzian shape of the following form

$$\mathcal{L}(f) = A\frac{\gamma}{\gamma^2 + (f - f_0)^2} + A_0 \ , \tag{5.1}$$

where A is the amplitude of the Lorentzian peak, γ is the linewidth of the peak, f_0 is the center frequency and A_0 is the offset given by the noise floor. The Signal-to-Noise Ratio (SNR) is greatly increased by the presence of an SPA as a Quantum limited amplifier.

5.2.1 Qubit properties

After performing two-tone spectroscopy, fixing ω_r and sweeping the qubit IF ω_{qIF}, the qubit frequency is found very close to the phonon mode. For this reason it is not possible to operate at the bare qubit frequency without starkshift. A new rest point is chosen by applying a stark shift pulse. The chosen qubit rest frequency is at 5.969940 GHz, corresponding to a stark shift amplitude $\epsilon_0 = 0.159$ V. Afterwards a gaussian pulse of length $t_g = 100$ ns is sent, and as a function of amplitude Rabi oscillations are observed as in Fig. 22(b). The π pulse amplitude is calibrated to be $\epsilon_g = 0.085$ V. Then, qubit properties are measured. Their plots and sequences are shown in Fig. 22(c) and 22(d) (Refer to subsection 3.15 for significance of these measurements). In particular T_1, the relaxation time, is measured by fitting an exponential line to a qubit decaying after exciting it with a π pulse to the excited state. The T_1 value has an average of 10.1 µs. T_2, the dephasing time, is measured by applying a $\pi/2$ pulse, waiting for a time t and applying a second $\pi/2$ pulse before reading out. Better resolution is present when setting an artificial detuning for the second pulse, resulting in oscillations in the qubit population. The expressions for the two fitting functions are

$$A_1(t) = Ae^{(-t/T_1)} + A_0 \ , \qquad A_2(t) = -Ae^{(-t/T_2)}\cos(2\pi\omega_{det} * t + \phi) + A_0 \ , \tag{5.2}$$

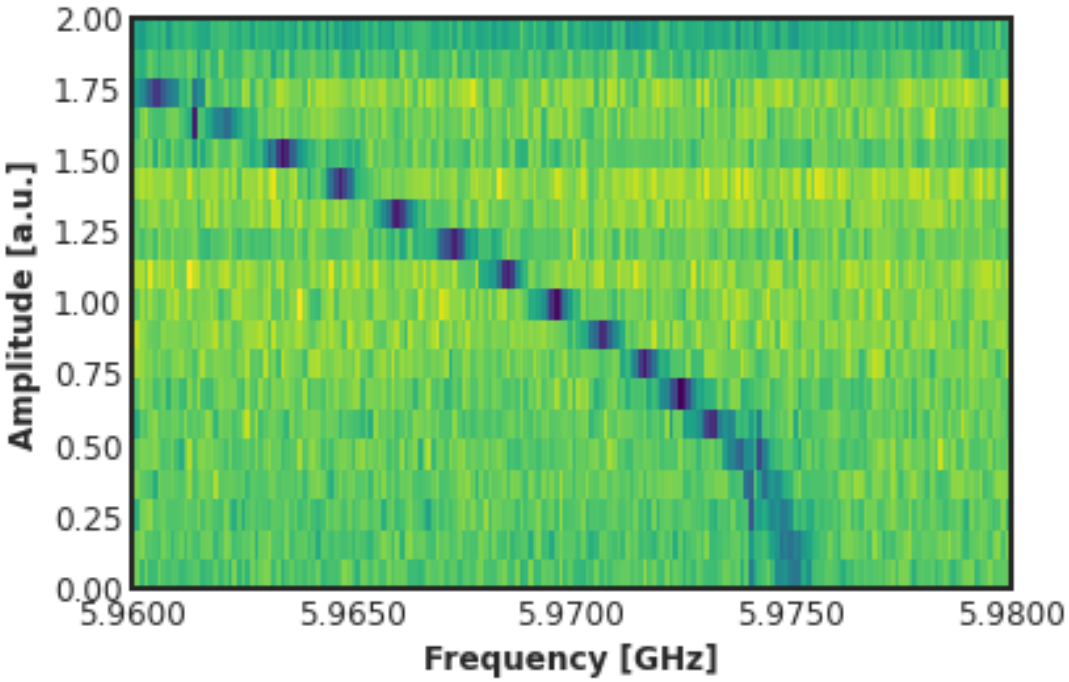

Figure 23: Qubit spectroscopy over stark shift amplitude. At $\omega_r - \omega_{ss} = 70$ MHz detuning the qubit can be tuned over a 20 MHz range. A slight feature of the anticrossing can be seen around 5.974 GHz and is addressed in the main text.

with the maximum amplitude and amplitude offset A and A_0, ϕ as a possible phase offset in the cosinusoidal function and ω_{det} the artificial detuning . The average T_2 time is 8.8 µs. After standard qubit characterization, the next step is measuring the shift in qubit frequency depending on amplitude of the stark shift. As discussed in subsection 3.1.3, compromising between stark shift detuning and amplitude is crucial to not populate the microwave cavity with a high number of photons. The plot of measured qubit frequency vs stark shift amplitude at 70 MHz detuning is shown in Fig. 23. The qubit can be tuned over two different phonon modes, that are needed for the desired protocol. The phonon frequency can be seen in the anticrossing feature. After zooming in, we report a phonon frequency of ω_p of 5.974117 GHz, basically unchanged from previous measurement in different cooldowns. The stark shift amplitude to tune the qubit on resonance with the phonon mode is 0.151 V.

5.2.2 Phonon properties and tuneup

Afterwards, the phonon mode addressed can be analyzed. The first step is to calibrate the swap operation between the qubit and the phonon mode, that exchanges excitation between the two. After measuring a frequency of $g = 258.5$ kHz (consistent with previous measurements), the swap time can be found imposing $2\pi * gt_{swap} = \pi$, resulting in $t_{swap} \approx 960$ ns. Now, it is possible to measure the phonon decoherence times T_1 and T_2 with the usual protocols, interleaving the waiting time by two swap operations. They are shown in Fig. 24(a) and 24(b). Average T_1 is 84.5 µs and average T_2 is 105 µs. In Fig. 24(c), vacuum Rabi oscillations between the first order transverse mode and the qubit (left), and the longitudinal mode and the qubit (right). It is important to note that the abscissa in this plot is the stark shift amplitude, so it has an opposite dependence with respect to the frequency.

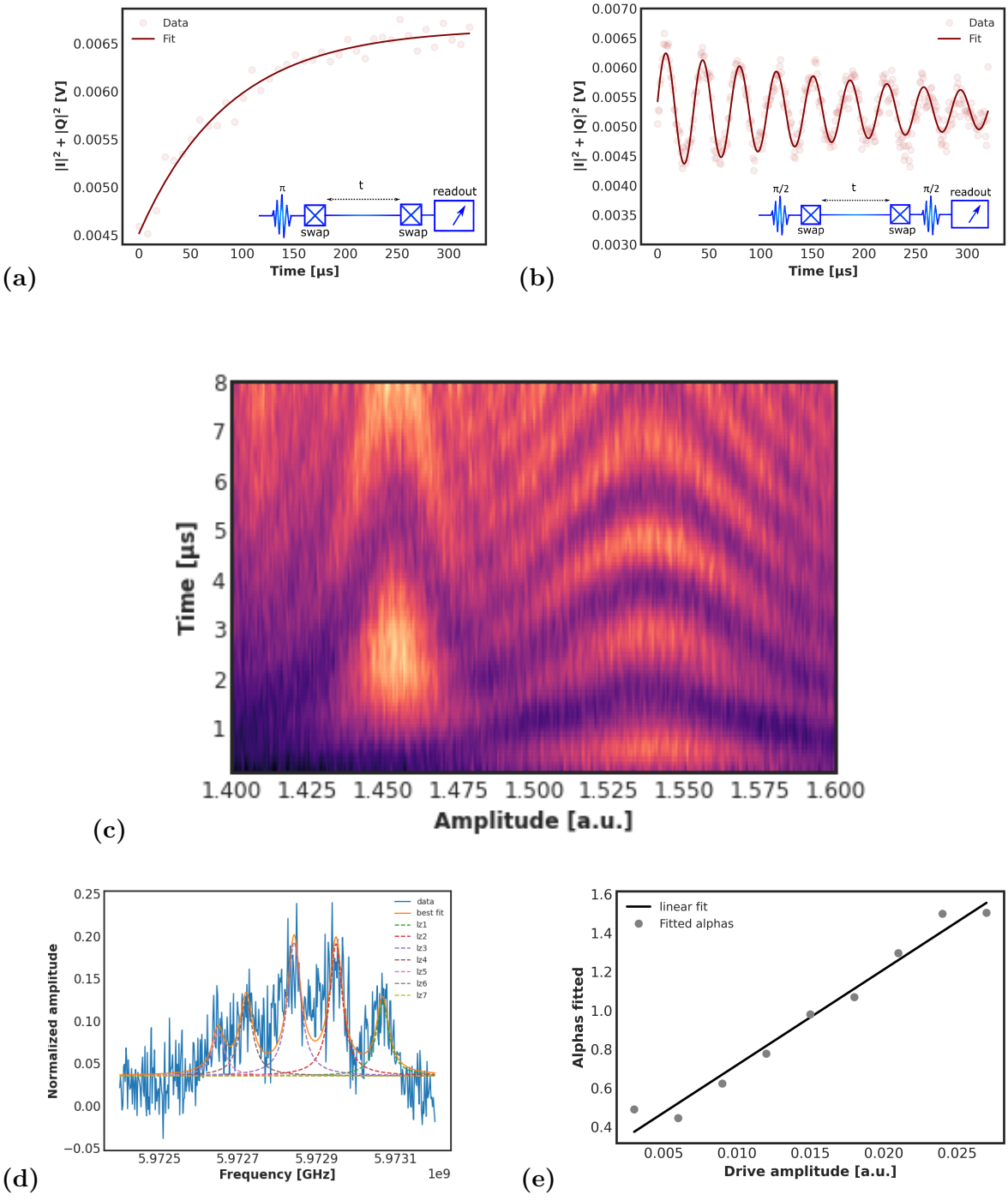

Figure 24: Phonon properties measurement, vacuum Rabi oscillations between qubit and phonons and coherent state calibration. In (a) and (b) T_1 and T_2 data and control sequences are shown. (c) displays vacuum Rabi oscillations as the qubit is tuned with two different phonon modes. The phonon mode interacting with the qubit on the left is the higher order transverse mode, while the one on the right is the fundamental mode that addressed during the protocols. The amplitudes on the x-axis differ from the amplitude value 0.305 used for resonant interaction between qubit and phonon mode used in the following experiments, because here we sweep over the next lower fundamental mode family. (d) shows the effect of number splitting of a coherent state on the qubit, and the fit of this coherent state. (e) represents the fitted values of the coherent state amplitude α depending on the drive amplitude.

From this plot it is also possible to extract the selectivity of the zero order mode, defined as the ratio between the coupling with the fundamental mode and the coupling with the higher order mode. In this case the selectivity is satisfying: $g_{m=0}/g_{m=1} \approx 4$. This means that except from being close to the resonance of the higher order phonon, the qubit does not interact with it. After measuring the phonon properties, the next step is calibrating the amplitude during the creation of coherent states. Therefore, a coherent drive is applied while the qubit is at the rest point and after tuning it up closer to the phonon mode at a frequency of $\omega_{cs} = 5.97308$ GHz, it is driven with a slow saturation pulse of a duration of 20 µs, bringing it to a superposition state. The frequency of the pulse is changed to effectively perform qubit spectroscopy. The length of the π pulse is essential to not widen the qubit intrinsic linewidth $1/\gamma$. Remembering eqn. (3.27), the peaks are spectroscopically resolved in the case $\chi >> \gamma_q$ where γ_q is the linewidth of the qubit. The amplitude of each peak is linear as a function of the corresponding Fock state population. Phonon number splitting is observed and the coherent state amplitude α can be measured by fitting a Voigt profile, a sum of Lorentzian peaks. α is extracted by fitting a poissonian distribution to the presumed Fock number amplitudes (recall eqn. (2.14)). Typical errors are on the order of $10 - 15\%$. The errors are due to phonon decay, during the saturation pulse Fitting α for several drive amplitudes is shown in Fig. 24(e). As expressed in eqn. (3.3.2), the drive amplitude - coherent state dependence is linear. In fact, the points can be fitted together with a line. The target α of 1.5 needs a drive amplitude of 0.026 a.u. for that specific rest point.

5.2.3 Ramsey-like parity measurements

The last ingredient to measure the Wigner tomography of a state and fully characterize it is represented by parity measurements possible in the strong dispersive regime (subsection 3.3.1). An interaction point is chosen after some considerations at $\omega_{qi} = 5.972295$ GHz. The interaction detuning corresponds to $\delta_{ki} = 1.82$ MHz. This point allows to be in the dispersive approximation ($g/\delta_{ki} = 0.2585/1.822 \approx 1/7$), while granting an interaction time π/χ shorter than the qubit coherence times. Using the same protocol as in subsection 4.1.2 the result is shown in Fig. 25. The expected interaction time from the dispersive approximation is $\pi/\chi = 4\pi g/\delta_k = 6.817$ µs with $g = 2\pi * 258.5$ kHz and $\delta_{ki} = 2\pi * 1.822$ MHz. This number is fairly close to the right vertical line in the plot, corresponding to the maximum contrast of the first four Fock state parities. The contrast of the left line corresponds to the maximum over the sum at different times of the first three Fock numbers ($|0\rangle$, $|1\rangle$ and $|2\rangle$)

$$C_{left} = max\left(\sum_{n=0}^{2}(-1)^n(0.5 - \langle\sigma_z\rangle(t))\right) = 0.705 = 0.235 * 3 \ , \tag{5.3}$$

with

$$t_{left} = argmax\left(\sum_{n=0}^{2}|0.5 - \langle\sigma_z\rangle(t)|\right) \approx 6.4\mu s \ , \tag{5.4}$$

while the contrast of the right line is the same quantity over the first four Fock numbers ($|0\rangle$, $|1\rangle$, $|2\rangle$ and $|3\rangle$)

$$C_{right} = max\left(\sum_{n=0}^{3}(-1)^n(0.5 - \langle\sigma_z\rangle(t))\right) = 0.82 = 0.205 * 4 \ . \tag{5.5}$$

with

$$t_{right} = argmax\left(\sum_{n=0}^{3}|0.5 - \langle\sigma_z\rangle(t)|\right) \approx 6.8\mu s \ . \tag{5.6}$$

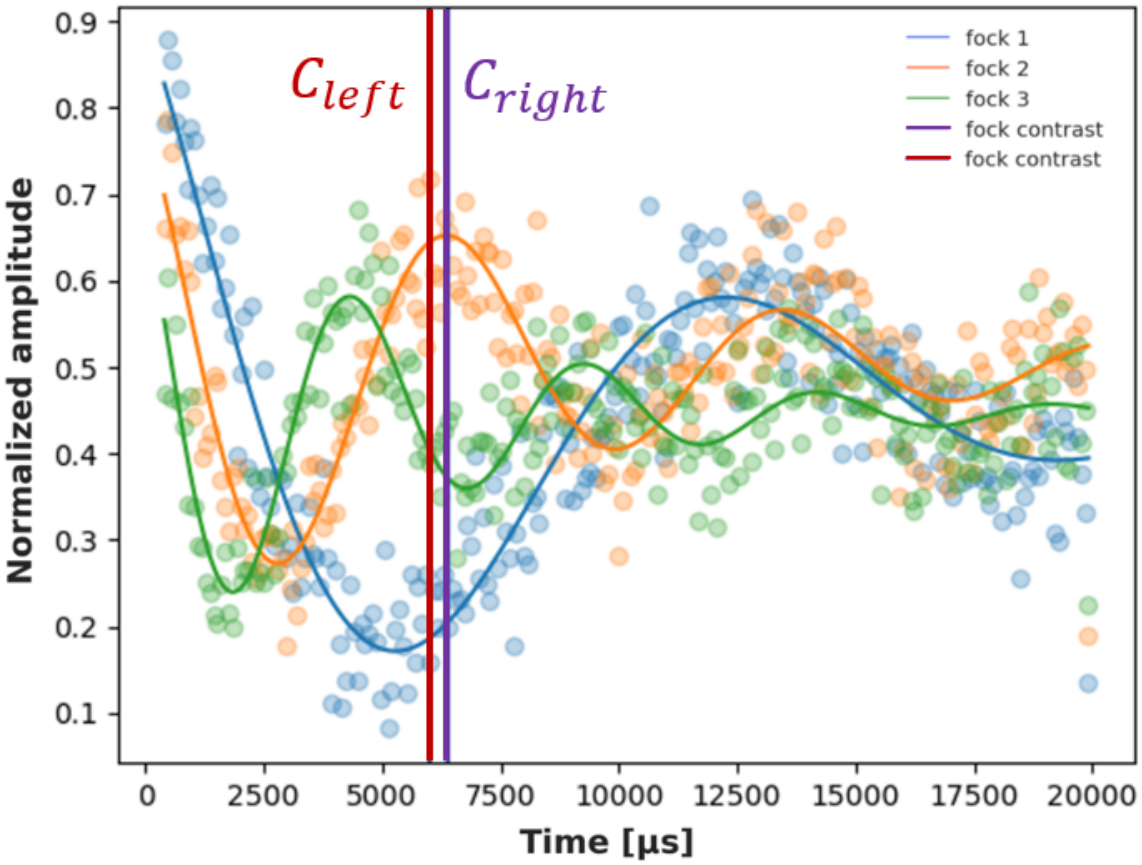

Figure 25: Ramsey sequences at the interaction point depending on the state generated in the phonon mode plotted for Fock $|1\rangle$, $|2\rangle$ and $|3\rangle$. Each added Fock number increases the frequency of the oscillation by χ. The vertical lines C_{left} and C_{right} represent the maximal contrast of eqn. (5.3) and eqn. (5.5) respectively.

The normalized contrasts $C_{left}/3 = 0.235$ and $C_{right}/4 = 0.205$ display that the average value for each single measurement are higher for the left line. Furthermore, since the coherent states generated have a smaller average phonon number than 3, an interaction time of $t_{int} \approx 6.4$ µs is chosen, the time for which there is maximum contrast for the first three Fock state parity values.

5.3 State tomography

As elucidated in subsection 4.1.3, tomography of the full state can be performed by measuring the parity at different points in phase space. Selecting a point in phase space is possible by applying a displacement operator $D(\alpha)$. To verify the effectiveness of the sequence, Fock state $|0\rangle$, $|1\rangle$ and $|2\rangle$ have been measured. In this section, qubit-phonon interaction when the phonon is prepared in a coherent state, is also shown. After preparing a coherent state α, collapse and revival of Rabi oscillations can be observed. By measuring the phonon state after a specific time, the collapse time $t_r/2$ (≈ 2.89 µs, for the given parameters), the resonant SCS emerges.

5.3.1 Quantum and quasi-classical states

After the necessary steps aforementioned, measuring the Fock $|0\rangle$ state is straightforward. It is just necessary to perform displaced parity measurements with different amplitude and phase. To measure Fock $|n\rangle$ states, a sequence of π pulses and swap operations is performed n times, where n is the desired Fock state. Climbing the Fock state ladder requires recalibrating the swap time for each Fock number. Eqn. (2.6) illustrates the dependence of the frequency on the Fock state number n. When addressing the $\{|e,n\rangle, |g,n+1\rangle\}$ the swap time is $t_{swap,n} = \frac{1}{\sqrt{n}}\frac{1}{4g}$. In the case of $\{|e,1\rangle, |g,2\rangle\}$ the estimated swap time is of $t_{swap,1} = \frac{960}{\sqrt{2}} \approx 678.8$ ns. The actual swap time chosen is of 676 ns (the number chosen must be a multiple of 4 ns, due to control equipment constraints). Immediately after state preparation, a second ancillary longitudinal phonon mode one FSR away is employed for qubit cooling. Bringing back the qubit to the ground state is independent from the qubit state itself. It is necessary to tune the qubit in resonance with the ancillary phonon mode for a swap time $t_{swap} = 960$ ns. This timescale is the same as the main phonon mode addressed, due to the same coupling value. The sequence for state preparation portrayed is executed before displaced parity measurements. The measured Wigner tomographies of the Fock states $|0\rangle$, $|1\rangle$ and $|2\rangle$ are depicted in Fig. 26. The slight negative background, present in both simulations and measurements, is due to the fact that the system is not perfectly in the dispersive regime for the interaction point chosen. Slightly varying the interaction time t_{int} compensates the aforementioned effects. The decreased negativity in the measured plots is attributed to several reasons. The first consists of decay of the states towards the vacuum, consequently becoming more and more classical over time. Secondly, during the dispersive measurement, finite energy exchange is present, consequently reducing the contrast due to misalignment of the oscillations relative to different Fock states. However, these effects and more are all intertwined, making it hard to pinpoint a single cause.

5.3.2 Cat state, collapse and revival

The goal of this subsection is to measure the effects of the qubit-phonon interaction, when a coherent state α in the phonon mode is prepared. In the qubit population, collapse and revivals of the Rabi oscillations are seen (see section 4.2.1), while in the phonon mode a resonant cat is generated.

Observation of the collapse and revival of the Rabi oscillations

As explained in subsection 2.2, a two-level system interacting with a coherent state does not present the simple Rabi oscillations deriving from the JC interaction, but the oscillations collapse with a rate depending on α and manifest themselves again after a revival time t_r (see eqn. (2.19)). To verify the oscillations experimentally, coherent state of different sizes are prepared and left to interact with the qubit prepared in the excited state. The resulting observation is shown in Fig. 27, for coherent state amplitudes α of approximately $0.3, 0.6, 0.7, 0.9, 1.4, 2, 2.5, 3$. For low values of α the qubit population experiences slightly distorted Rabi oscillations. As the coherent state increases, different features can be discerned until full collapse for $\alpha \approx 1.4$. It is remarkable that for $\alpha \approx 3$ revival of the Rabi oscillations is present at time $t_r = 12$ µs, but predictable from the high phonon T_1 and not too small qubit T_1.

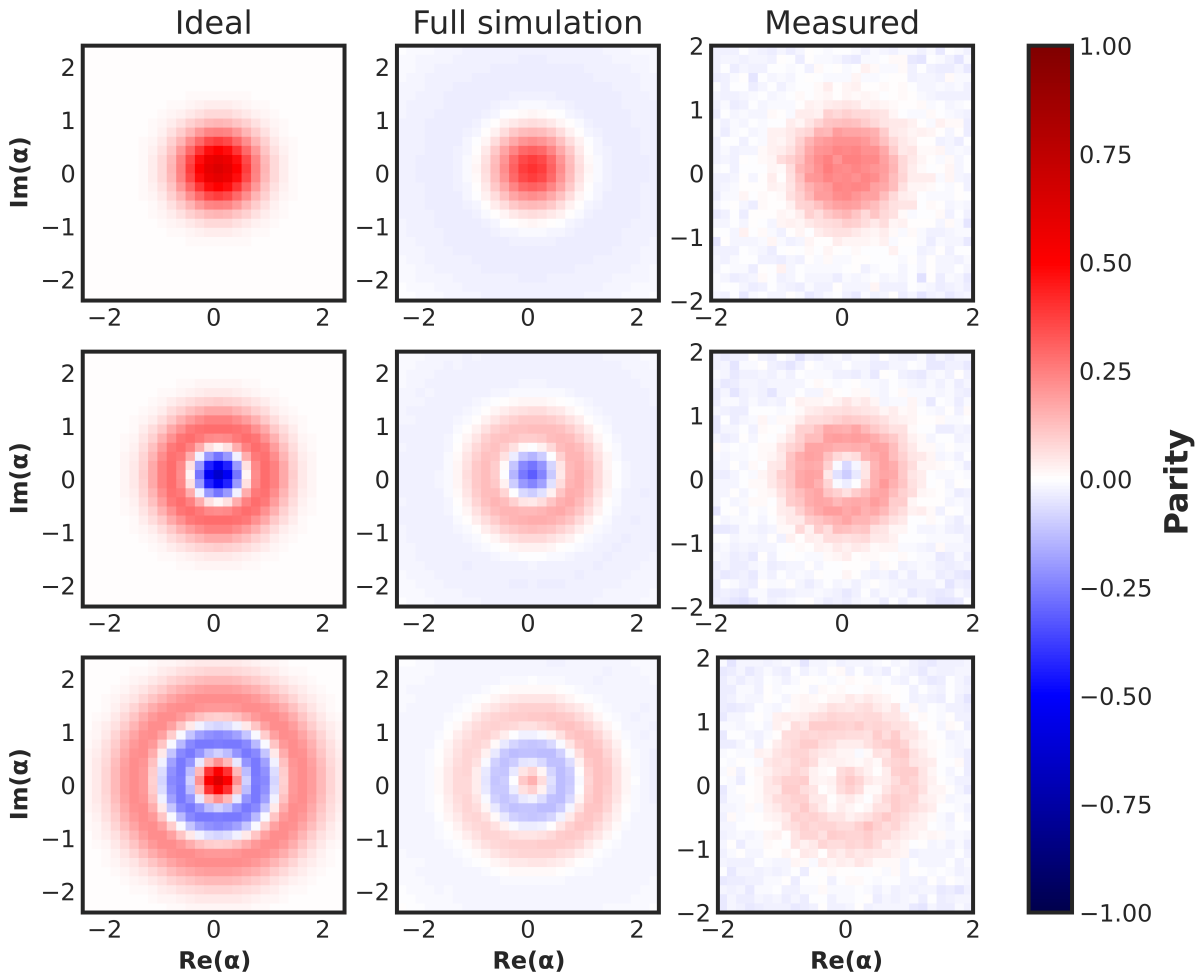

Figure 26: Ideal, fully simulated and measured $|0\rangle$, $|1\rangle$ and $|2\rangle$ Fock states. The colorbar for the first column refers to amplitude of the Wigner function, while for the second and last column it refers to the simulated and measured parity.

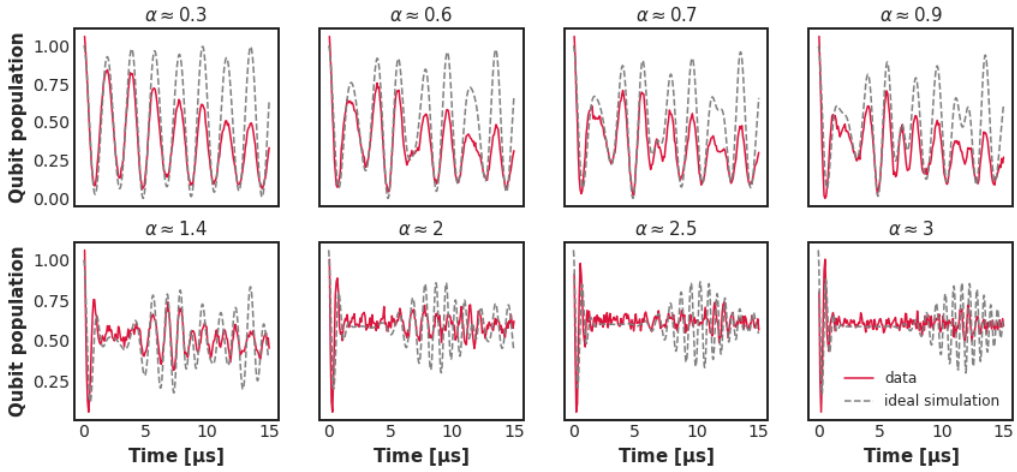

Figure 27: Collapse and revival of the qubit initial state population for eight different coherent state amplitudes α are shown. Some of the data has an offset to overlap with the center line of the simulated data. This results from incorrect normalization of the excited state.Decay is not included in the theoretical simulation curves.

Resonant cat measurements

After verifying qubit-phonon interaction through the qubit population during collapse and revival, the last experiments consist in generating the resonant SCS as explained in subsection 2.2. Verifying its creation requires checking the phonon state instead. The protocol from section 4.2.1 can be applied. The starting point consists in tuning the qubit to the rest point frequency ω_{qr}, and applying a pulse drive at the phonon mode frequency creating a displaced vacuum state with $\alpha = 1.5$. After performing a π pulse on the qubit to bring it to the excited state, the qubit is shifted into resonance with the phonon, interacting for half of the revival time $t_r/2 = \alpha\pi/g'_k \approx 2.976$ µs with $g'_k = 2\pi g_k$. This number can be calibrated in a better way by optimizing it with respect to the final state fidelity. However, simulations show that the resonant cat has negative fringes, whose presence proves state creation, in a relatively large neighbourhood of interaction times t_{int}. Following the displacement of the qubit at the rest point, Wigner tomography is performed, showing resonant cat fringes in Fig. 28(a). 20000 averages were taken to acquire a sufficient contrast, and a large picture was not taken for measurement time constraints and control instrument memory constraints. After measuring the SCS, it is possible to simulate the state with the simulator with the same parameters as the device. The amplitude of the coherent state of the simulated cat is of $\alpha = 1.4$, fairly close to the predicted 1.5. The simulated state is shown in Fig. 28(b). The simulated and measured states encompass analogous features in the Wigner function. The size of the states match, while fringes are qualitatively similar. Parity measurements can be performed also in simulations, resulting in the Wigner function of Fig. 28(c). The fidelity between the measured and the simulated cat is calculated with eqn. (4.7), with value $\mathcal{F} = 0.272$. This relatively low value of fidelity comes about from several effects. For example, due to the slight mismatch in rotation and the difference in parity amplitude between the measured and simulated Wigner functions (compare Fig. 28(a) and 28(c)). Fidelity can be further improved by better calibration overall: performing mixer calibration, measuring precisely qubit and phonon frequencies, reducing phase noise in the

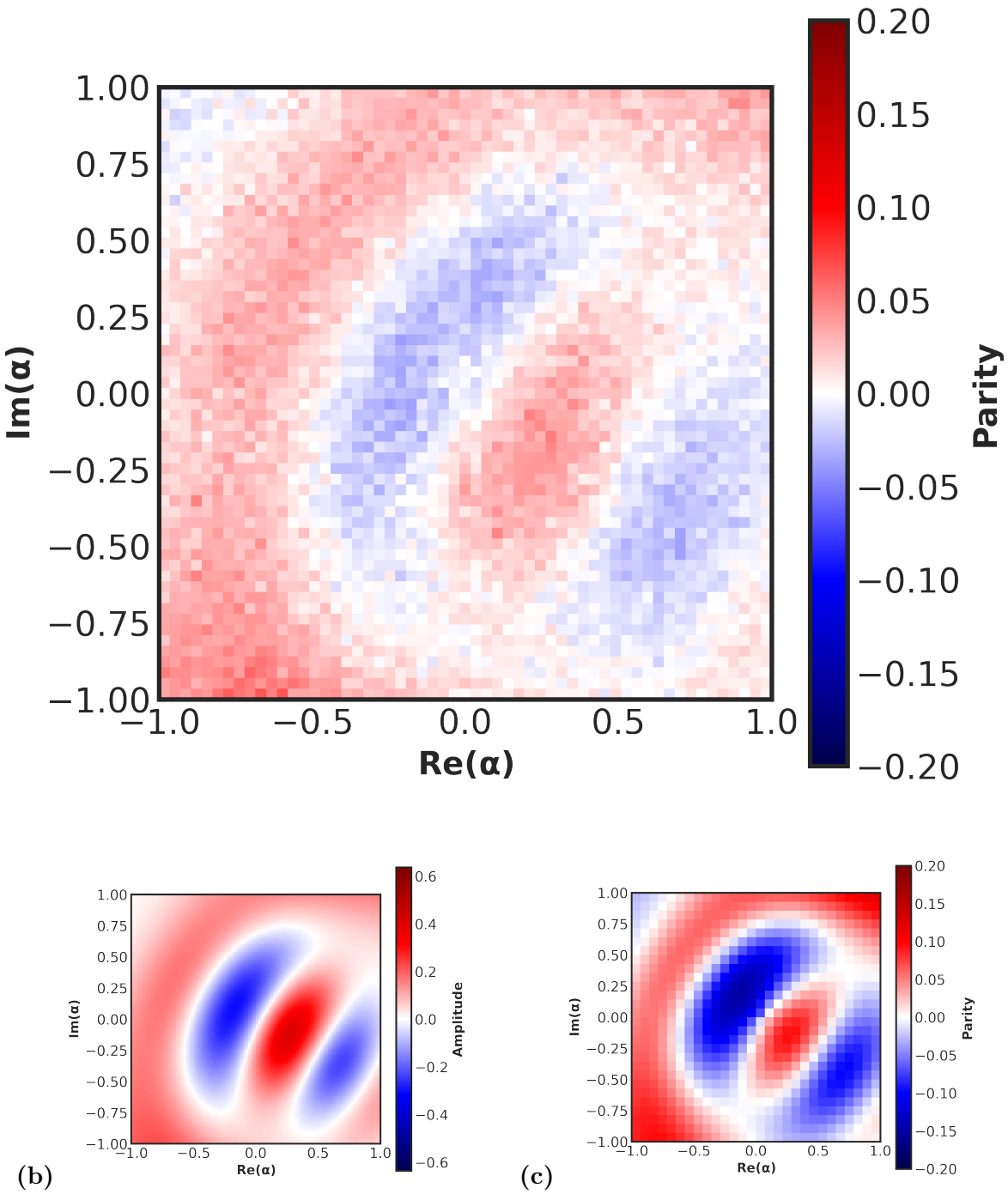

Figure 28: In (a), the measured resonant cat fringes are shown, in an n x n grid with $n = 58$ and axes between the values [-1,1]. In (b), the resonant cat with a coherent state of $\alpha = 1.4$ and same parameters as Table 1 is depicted for comparison with the measured state, also zoomed-in. In (c), simulated displaced parity measurements are added, showing the final result. There is a slight mismatch in rotation, since the measurements of the simulations are performed in the qubit rotating frame.

stark shift pulse that makes the shifted qubit frequency unstable. Nonetheless, the crucial result of being able to generate in experiments SCSs identical, at least structurally, to simulations firmly encourages to employ the simulator developed to predict several properties of the states. For example, some features of interest are coherence and sensitivity to particular processes, as shown in the following chapter.

6 Cat state applications

Raising the kitties

"Infinities and indivisibles transcend our finite understanding, the former on account of their magnitude, the latter because of their smallness; Imagine what they are when combined."
Galileo Galilei

In chapter 5, the generation of a resonant cat has been proven experimentally. Naturally, state characterization has not been obtained from a single shot measurement, but rather it was reconstructed from a collection of realizations over time. Quantum state reconstruction has been studied for a long time [54], and has been achieved for SCSs [55]. The reconstruction process allows to assemble the corresponding density matrix of the state from the measured Wigner function. Given the reconstructed state, an interesting idea for analyzing it is quantifying how macroscopic the state is. In the literature, the topic of macroscopicity has been thoroughly disputed [56]. A question to ask is what defines the size of a quantum state created? The phase space is a pragmatic gadget through which this notion can be objectively quantified. A displaced vacuum state in phase space has a gaussian shape of finite width as a quasi-probability distribution. The coordinates of the center point are the same as in classical mechanics, as stated by the Ehrenfest theorem [57]. Consequently, a coherent state is as macroscopic as a vacuum state, despite containing a larger number of excitations. Instead, quantum fluctuations are the origin of quantum noise in the probability distribution, contributing to a macroscopicity measure. A notion of subjective macroscopicity can be defined referring to an observer dependent measurement, based on the concept of a coarse-grained detector that can only distinguish macroscopically separated eigenvalues. The sensitivity to a certain type of operation is a quantitative measure for this type of subjective macroscopicity. In Section 6.1, resonant cat coherence for the device parameters is simulated, and the dependence of cat coherence on α is computed. In Section 6.2, the resonant cat is compared to other ideal states and their sensitivity is calculated.

6.1 Coherence

The concept of macroscopicity is fully tangled with quantum coherence. However, this coherence must be defined with respect to a basis. Quantum coherence for a SCS can be quantified in different ways, for example with respect to a coherent state basis. A simplistic approach for measuring it consists in measuring the Wigner function at several times t and calculate the fidelity with the original Wigner function and fit its decay overtime. However, better measures have been developed over the years. In this work, the method of [55] to actively observe decoherence in the density matrix is adopted. First, the state is rotated until the coherent state blobs both lie on the $\Re(\alpha)$ axis. The second step consists in displacing a SCS such that one coherent blob coincides with the origin, such that the classical coherence of each component of the SCS can be distinguished from their mutual quantum coherence. The displacement acts on an ideal state in the following way

$$\hat{D}(-\alpha)|\psi\rangle_{cat} \propto (|0\rangle + |-2\alpha\rangle) \ , \tag{6.1}$$

leaving the relative distance between each classical component unchanged in phase space. The reconstructed density matrix has quantum coherence only present in the diagonal terms, with maxima corresponding to the classical component position $k = 0$ and $k = |2\alpha|^2$. More explicitly, quantum coherence can be quantified by the sum of the matrix elements overlapping with the $|0\rangle$ state in the Fock state basis, either $C_{cat} = \sum_{k>2\alpha}\langle 0|\hat{\rho}_{cat}|k\rangle$ or equivalently $C_{cat} = \sum_{k>2\alpha}\langle k|\hat{\rho}_{cat}|0\rangle$. The terms up to 2α are removed because of distorsions of the vacuum blob with respect to an ideal coherent state. The coherence of a resonant SCS, with

$\alpha = 1.5$ generated with the parameters of Table 1, is fitted and plotted in Fig. 29(a). Oscillations in the plot are partly attributed to imperfect alignment of the state with the $\Re(\alpha)$ axis. The resulting coherence time value for the SCS $T_{cat} = 6.83$ µs, can be mainly associated to decay losses through the qubit and due to the coherent state amplitude. In fact, the qubit-phonon detuning chosen is the same as the measurement rest point of $\delta_{qr} = 4.177$ MHz. However, the coherence value heavily varies for different qubit resting points. For a detuning of $\delta_{qr} = 24$ MHz, cat coherence of $T_{cat} = 13.28$ µs has been simulated for the same amplitude α. Moving the qubit even further away, has increased this value even more. In [25], an expression for T_{cat} as a function of amplitude α is derived by calculating the impact of relaxation processes affecting the non-diagonal coherence terms of $\hat{\rho}_{cat} = |\psi\rangle_{cat}\langle\psi|_{cat}$. The resulting expression of the ideal coherence time T_{id} reads

$$T_{id} = \frac{T_{1s}}{2|\alpha|^2} \ , \tag{6.2}$$

where T_{1s} is the decay time of the system. In the case under consideration $T_{1s} = T_{1p}$ is the decay time of the phonon mode. Coherence is simulated for resonant SCSs with different coherent states $\alpha = 1, 1.25, 1.5, 1.75, 2$. The respective coherence times of the SCSs are $T_{cat} = 24.67, 17.88, 13.28, 9.69, 8.22$ µs at the previously mentioned rest point $\delta_{qr} = 24$ MHz. As can be seen in Fig. 29(b), the values follow the curve defined in eqn. (6.2), albeit with a normalization factor. An example of SCS theoretical coherence time is given by substituting in eqn. (6.2) $\alpha = 1$: $T_{id,\alpha=1} = 84.5/2 = 42.25$ µs, value higher than the simulated value $T_{cat,\alpha=1,} = 24.67$ µs. The reduction in the SCS coherence time, as mentioned before, depends on the qubit-phonon interaction and changes for difference detuning. Problems arise when attempting the protocol in practice, because larger δ_k means larger amplitude ϵ_k, thus impractical implementations and more undesired couplings.

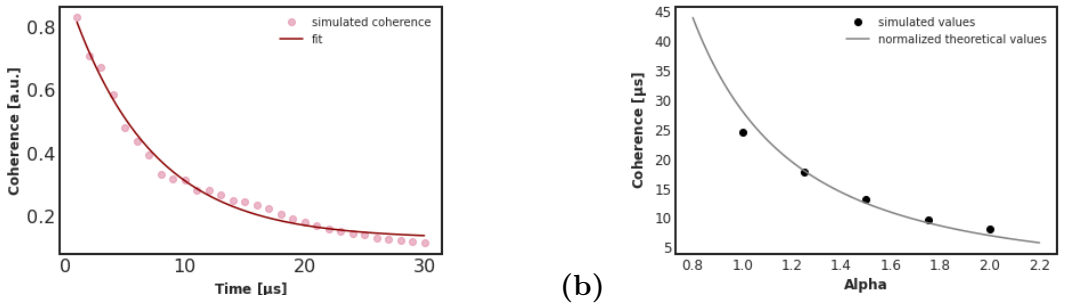

Figure 29: (a) Cat coherence of a simulated resonant cat with the same parameters as Table 1 as a function of waiting time calculated with the method discussed in main text. Fitted value of $T_{cat} = 6.83$ µs. (b) Cat coherence as a function of α. Same parameters of (a) are used except for the qubit-phonon detuning of $\delta_{qr} = 24$ MHz. Inverse square dependence is well predicted by theory (eqn. (6.2)).

6.2 Sensitivity to a displacement

Another indicator of the usefulness of the state is its sensitivity to a displacement. The details are out of the scope of the thesis, but the objective of this discussion is to demonstrate that this sensitivity of a simulated resonant cat with the same parameters as the measured one has a bigger sensitivity than other quantum states that have been already created and measured in the device of this work. Hence, generating a SCS A quantity employed to quantify this sensitivity is the quantum Fisher information (QFI), defined as the

maximum of the classical Fisher information after over a generalized measurement $\hat{M}$ on a quantum state [58]. Several inequalities have been derived to bound the QFI. The one used for this analysis is the following: define a displacement $\hat{D}(\beta)$ in the same direction of the maximum amplitude change of the Wigner function relative to the quantum state (in the case treated, perpendicolar to the SCS fringes). Afterwards, measure the statistics of the observable

$$\hat{\mathcal{O}}(\beta) = \hat{D}(\beta)^{\dagger}\mathcal{P}\hat{D}(\beta) \ , \tag{6.3}$$

where $\mathcal{P}$ is the parity operator. In the case of the parity operator the eigenvalues are either -1 and $+1$. Apply operator $\hat{\mathcal{O}}(\beta)$ to state $\hat{\rho}_{cat}$ and measure the number of counts (analogous to probability) for each result. Call the counts associated to eigenvalue -1 as p_- and the ones associated to eigenvalue $+1$ as p_+. Afterwards, apply another infinitesimal displacement along the same direction $\hat{D}(\zeta)$. Subsequently, repeat the same observable statistic measurements, obtaining two count values, q_- for eigenvalue -1 and q_+ for eigenvalue $+1$. It can be proven that a QFI lower bound is given by (analogous to the one in [59])

$$\mathcal{F}_Q > \frac{1}{\zeta^2}\arccos\left(\sqrt{p_+q_+} + \sqrt{p_-q_-}\right)^2 \ . \tag{6.4}$$

In Fig. 30(a) a cross-cut of the Wigner function along the $\Re(\alpha)$ axis is plotted, for an ideal ψ_{cat} state, an ideal resonant cat, a resonant cat with losses ψ_{res} and a Fock superposition state $\psi_{sup} = 1/\sqrt{2}(|0\rangle + |1\rangle)$. The superposition state is chosen for comparison because its generation and measurement has been achieved in the device used in this work and, among the states generated, has an appreciable area in the Wigner function with negative values, necessary condition for high sensitivity. The initial coherent state for all SCSs chosen is $\alpha = 1.4$, as the one measured. The losses (and all other parameters, see Table 1) for the non-ideal resonant cat are set to the same of our measurements. Parity measurements are not included. One thing to note is that the resonant cat fringe structure adequately coincide with the ideal SCS both for the ideal case and not, with the difference being their amplitude and symmetry. Ideally, one would expect the sensitivity to a displacement along the fringe direction to directly depend on the derivative of the fringes themselves. From eqn. (6.4), this can be seen by using the conditions $p_+ + p_- = 1$ and $q_+ + q_- = 1$. In fact, the more q_+ varies from p_+ in the second measurement, the more q_- would also vary from p_-, consequently decreasing the argument of the arccos function and subsequently increasing the overall lower bound. The sensitivity values of eqn. (6.4) for the four states are shown in Fig. 30(b), using a small enough displacement with parameter $\zeta \approx 0.055$. The only discrepancy with expectation corresponds to the 0 point of the ideal SCS. That point suffers from an indeterminate form $0/0$ and as soon as losses are present, with the maximum amplitude of the SCS Wigner function being subsequently lower than $2/\pi$, a dip emerges with width and depth depending on the exact losses. The key takeaway from this plot is that the resonant cat display a substantial sensitivity, more than three the sensitivity of an ideal superposition state such as ψ_{sup} for the α chosen. Even for the In the literature, several measures of macroscopicity have been defined. Even the coherence of the QFI has been employed [58], and its decay should theoretically coincide with the coherence of section 6.1. As discussed in the next chapter, the two measures of coherence and sensitivity allow to characterize the macroscopicity and "quantumness" of the state created.

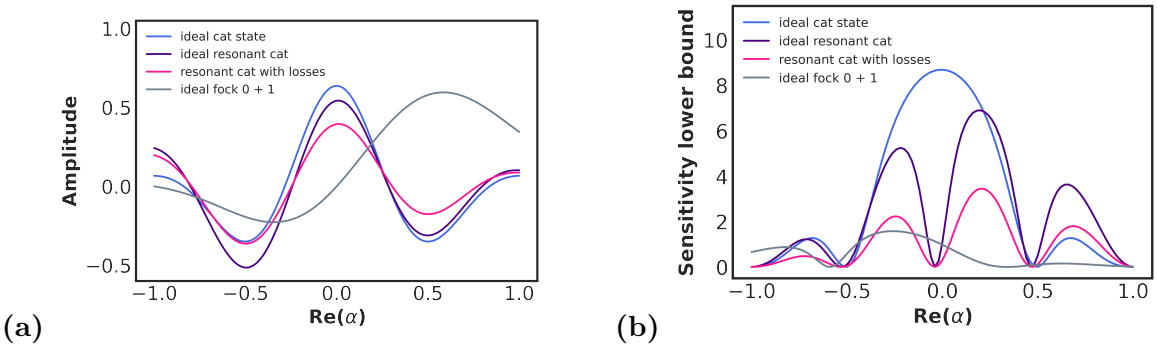

Figure 30: (a) Cross-cuts of Wigner functions along the $\Re(\alpha)$ axis of an ideal even cat state (blue), an ideal resonant cat (purple), a resonant cat state with decoherence (pink), a superposition of Fock states $|0\rangle$ and $|1\rangle$ (gray). $\alpha = 1.4$ is chosen for all SCSs. (b) Sensitivity of a displacement along the $\Re(\alpha)$ axis of the same states as a function of the position β (or $\Re(\alpha)$). For the resonant cat, points of maximum sensitivity correspond to points of higher derivative of (a). The sensitivity values are calculated from eqn. (6.4) with parameter $\zeta \approx 0.055$, small enough for the approximation to derive the equation to be valid.

7 Outlook

Developing Schrödinger tigers

"Nothing in life is to be feared, it is only to be understood. Now is the time to understand more, so that we may fear less."
Marie Curie

The objective of this Thesis was the realization of a SCS in an acoustic resonator. The project was subdivided in two different parts: simulations and experiments.
At first, in chapter 1, we introduced the concept of a SCS both philosophically and as a physical state. In chapter 2, we have treated the basic theory of the Jaynes-Cummings Hamiltonian. Starting from the collapse and revival of Rabi oscillations, we derived the expression for an approximated SCS, the resonant cat. Two more protocols are shown to achieve the creation of a SCS. Afterwards, in chapter 3, we have dealt with the structure of our device, an HBAR chip coupled to a superconducting qubit chip inside a microwave 3D cavity. The physics and the ways to operate the system were presented. In chapter 4, we showed simulation results of achieving the implementation of both singular operations and the protocols aforementioned. Furthermore, Wigner tomography through displaced parity measurements was implemented successfully. Simulation automation of coherent state creation, parity measurements, resonant cat and heralded cat protocols for any possible parameter has been achieved. Particular emphasis has been put into finding optimal parameters to improve fidelities of the measured states. We performed studies on leakages of the phonon population through the qubit, dependence of fidelities on coherence times, detunings and qubit-phonon coupling. These studies have shown findings, such as the fact that improving qubit and phonon coherence always allows to find a new interaction point for parity measurements with better contrast. An important analysis was based on the dependence of the fidelity of a resonant cat to a SCS for a given coherent state amplitude α. We have shown a peak in fidelity for values close to $\alpha \approx 1.3$. As a result, we have chosen a coherent state amplitude of $\alpha \approx 1.5$ for simulations and experiments. This slightly higher value compared to the highest fidelity one is chosen as a consequence of the better resemblance to a SCS of the resonant cat for larger αs, as explained in section 4.2.1. Furthermore, larger αs result in higher negativity and larger average phonon number. Important findings were also related to unexpected behaviour for particular simulations. In fact, simulations did not all initially function as intended, eventually offering new insights on our physical understanding of the system. Indeed, we have discovered a coherent state drive dependence on the qubit state, previously not predicted due to invalid approximations (see Appendix D). Furthermore, during cat protocols, we have simulated coherent state amplitude dependence on the relative phase of the qubit superposition state after dispersive evolution. This effect can be potentially attributed in higher order terms in the dispersive Hamiltonian. In chapter 5, after careful characterization of the device, we have managed to reproduce displaced parity measurements to fully characterize the state in the phonon mode. Fock states $|n\rangle$ up to $n = 2$ were measured and compared to simulated states. The final result was the Wigner tomography measurement of a resonant SCS with average phonon number $\overline{n} \approx 2$. We have compared the measured state, with a simulated state using the same device parameters of $\alpha \approx 1.4$, subsequently reproducing the measured state in simulations. We have also introduced displaced parity measurements in simulations, for parity amplitude comparison. The seemingly low fidelity value of $\mathcal{F} = 0.272$ between the measured and simulated states is justified by the smaller values in parity contrast compared with simulated states. Despite the non-ideal measured contrast, the remarkable achievement of measuring a SCS has prompted us to think about possible applications with this state.

In chapter 6, we consequently discussed the coherence of a resonant cat and its sensitivity to a displacement perpendicular to the cat fringes in phase space. We have shown that, even for our device parameters, this sensitivity is much higher compared to other quantum states, such as an ideal Fock state superposition.
The results of this thesis have provided us several insights for SCS creation. We are confident that with better device parameters achieved by employing different materials and improving chip design, we will be able to measure SCSs with better fidelities. The heralded cat simulations yield simulation fidelities very similar, if not higher, to the resonant cat already measured. Attempting its generation in experiments is one of our next steps. The qcMAP protocol needs higher qubit coherence times compared to the other two protocols. The last conditional gate of the protocol limits the gate implementation: it must be long enough for it to be ideal, otherwise SCS fringes are faint. It is worth noting that the protocols adopted in this work are not the only ones possible. Generating a SCS with the quantum theory of optimal control has been simulated for a duration of 40 ns with fidelities of 0.9999 for a circuit QED system [60]. Further studies for implementation of SCSs in a cQAD system with optimal control will be conducted.

A Quantum states in phase space

In classical physics phase space distribution are employed to describe particle motion having coordinates position x and momentum p with dimensions of the according system. In 1932, Wigner introduced the concept for the first time of a phase space representation in the quantum case [61]. In the classical case, statistical uncertainty is given by a probability density $f(x,p)$; in quantum mechanics, even without any distribution describing the system, the exact value of conjugated variables cannot precisely be determined due to Heisenberg uncertainty principle. In quantum mechanics, a general quantum state can be described as

$$\hat{\rho} = \sum_i p_i |\Psi_i\rangle\langle\Psi_i| \tag{A.1}$$

This operator, the density matrix, can be represented in phase space through several functions: the Husimi-Q distribution, the Glauber-Sudarshan P distribution or the Wigner function. The first and the latter, are frequently used in quantum optics. However, the Wigner function is more valuable for describing the quantum features of a system. In particular, this way of visualizing quantum states provides a straightforward manner to understand single state properties, such as whether a state is classical or quantum and the uncertainty in the different coordinates of the state. Furthermore, it is possible to compare two different states by measuring the overlap between the two. In this chapter the Wigner function expression is treated in alternative ways in section A.1, its properties are listed in section A.2 and some examples are shown in section A.3.

A.1 Wigner function expressions

The Wigner function has several expressions. Its standard definition is [24]

$$W(x,p) = \frac{1}{\pi}\int_{-\infty}^{+\infty} e^{-2ipu} \left\langle x+\frac{1}{2}u\right| \hat{\rho} \left|x-\frac{1}{2}u\right\rangle du \ , \tag{A.2}$$

where $|x \pm \frac{1}{2}u\rangle$ are eigenstates of the position operator. If $\hat{\rho}$ is a pure state $|\Psi\rangle\langle\Psi|$ the expression becomes

$$W(x,p) = \frac{1}{\pi}\int_{-\infty}^{+\infty} e^{-2ipu}\Psi^*\left(x-\frac{1}{2}u\right)\Psi\left(x+\frac{1}{2}u\right) du \ , \tag{A.3}$$

where $\Psi\left(x \pm \frac{1}{2}u\right) = \langle x \pm \frac{1}{2}u||\Psi\rangle$. A simpler expression of the Wigner Function can be derived from eqn. (A.2). By using the translation relation and its conjugate

$$\begin{aligned} \left|x-\frac{1}{2}u\right\rangle &= e^{-i(x-u)p} D(x+ip) \left|-\frac{u}{2}\right\rangle \ , \\ \left\langle x+\frac{1}{2}u\right| &= \left\langle \frac{u}{2}\right| D(-x-ip) e^{i(x+u)p} \ . \end{aligned} \tag{A.4}$$

The parity operator $\mathcal{P}$ performs a symmetry around the phase space origin in the following manner

$$\mathcal{P}|x\rangle = |-x\rangle \ , \qquad \mathcal{P}|p\rangle = |-p\rangle \ . \tag{A.5}$$

Replacing eqn. (A.4) into eqn. (A.2), and using eqn. (A.5)

$$W(x,p) = \frac{1}{\pi}\int_{-\infty}^{+\infty} \left\langle \frac{u}{2}\right| D(-\alpha)\,\hat{\rho}\,D(\alpha)\,\mathcal{P} \left|\frac{u}{2}\right\rangle du = \frac{2}{\pi} Tr[D(-\alpha)\,\hat{\rho}\,D(\alpha)\,\mathcal{P}] \ . \tag{A.6}$$

The Wigner function is the average value of $2\mathcal{P}/\pi$ of the state obtained by applying a displacement in phase space by $-\alpha$ in the form $\hat{\rho} \to D(-\alpha)\hat{\rho}D(\alpha)$ Being the expectation value of an observable, W is directly measurable. From the eigenvalues of the parity operator being +1 and -1, it follows that the Wigner function is bounded:

$$-2/\pi \leq W(x,p) \leq 2/\pi \ . \tag{A.7}$$

In the case of parity measurements Wigner tomography, the bounds are the values of the operator $\mathcal{P}$ itself.

A.2 Wigner function properties

From the expression in eqn. (A.2), the Wigner Function can be grasped as a Fourier transform of the state

$$\hat{\rho}_x(u) = \left\langle x + \frac{1}{2}u \right| \hat{\rho} \left| x - \frac{1}{2}u \right\rangle \quad . \tag{A.8}$$

By noticing that $\hat{\rho}_x(u) = \hat{\rho}_x^\dagger(-u)$, it is possible to infer that $W(x,p)$ is always a real function, from Fourier transform properties. Furthermore, by integrating the Wigner function over the whole phase space, the integral can be calculated to be unitary

$$\int_{-\infty}^{+\infty} W(x,p)\, dx\, dp = 1 \ . \tag{A.9}$$

The function can be understood as a joint probability distribution in x and p, having both positive and negative values. For this reason, it is defined as quasi-probabily distribution. Additionally, the distribution allows to characterize how much a state resembles a different one. By taking the overlap of two Wigner function $W_1(x,p)$ and $W_2(x,p)$, each defined in eqn. (A.2) it is possible to find that

$$\begin{aligned} \pi \int_{-\infty}^{+\infty} W_1(x,p)\, W_2(x,p)\, dx\, dp &= \frac{1}{\pi} \int_{-\infty}^{+\infty} e^{-2ip(u_1+u_2)} \hat{\rho}_{1,x}(u_1)\, \hat{\rho}_{2,x}(u_2)\, du_1\, du_2\, dx\, dp \\ = \int_{-\infty}^{+\infty} \hat{\rho}_{1,x}(u)\, \hat{\rho}_{2,x}(-u)\, du\, dx &= \int_{-\infty}^{+\infty} \langle z|\ \hat{\rho}_1\ |z'\rangle \langle z'|\ \hat{\rho}_2\ |z\rangle\ dz\, dz' \\ = \int_{-\infty}^{+\infty} \langle z|\ \hat{\rho}_1\, \hat{\rho}_2\ |z\rangle\ dz &= Tr[\hat{\rho}_1 \hat{\rho}_2] \ , \end{aligned} \tag{A.10}$$

where z and z' are defined as

$$z = x + \frac{1}{2}u \ , \qquad\qquad z' = x + \frac{1}{2}u \ . \tag{A.11}$$

Substituting eqn. (A.1) for pure states leads to the fidelity between two states

$$\mathcal{F} = |\langle \psi_1 | \psi_2 \rangle|^2 \tag{A.12}$$

From the last two equations it is straightforward to check that $\hat{\rho}$ is a pure state if and only if

$$\pi \int_{-\infty}^{+\infty} W(x,p)^2\, dx\, dp = Tr[\hat{\rho}^2] = 1 \ . \tag{A.13}$$

In chapter 4, the same expression is used to calculate the fidelity of two states even if the states are not pure.

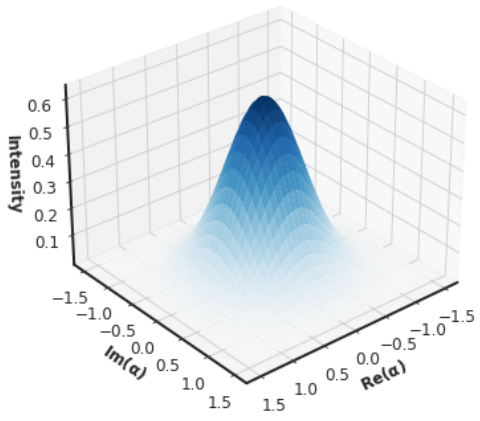

(a)

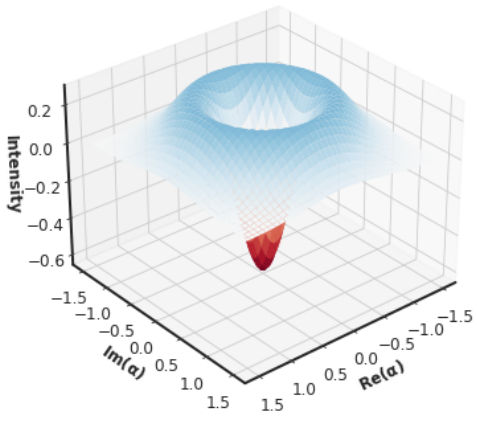

(b)

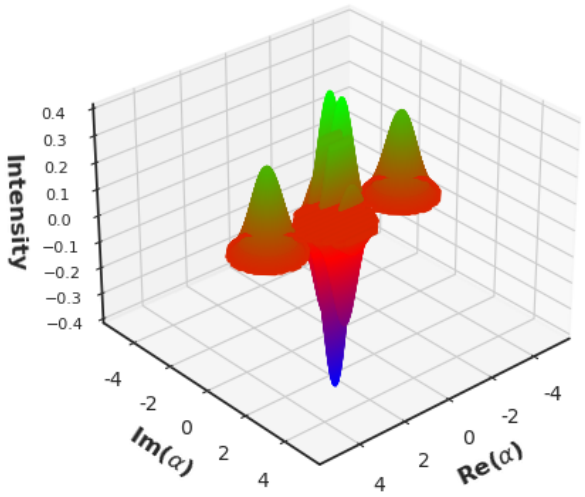

(c)

Figure 31: Representation of several states in phase space through their Wigner function represented in 3D. (a) Represents the fock number 0 state $|0\rangle$, while (b) the fock number 1 state $|1\rangle$. In (c) a SCS of $\alpha = 1.5$ of wavefunction $|\psi^{+}_{cat}\rangle$ from eqn. (A.19) is shown with different colours to enhance the fringes.

A.3 Examples of Wigner functions

For this section the treatment follows [25]. There are two main classes of states based on the Wigner distribution: 'quasi-classical' states, those whose Wigner function values are everywhere positive, and 'non-classical' those who present negative values.

Quasi-classical states

The paradigmatic example of a classical state is a coherent state $|\beta\rangle$ (including the vacuum state). Substituting the expression of a coherent state into the first line of eqn. (A.6), the Wigner function results to be a gaussian of the following form

$$W^{[|\beta\rangle\langle\beta|]}(\alpha) = \frac{1}{\pi^2}\int e^{-|\lambda|^2/2} e^{\lambda(\beta^*-\alpha^*)-\lambda^*(\beta-\alpha)} = \frac{2}{\pi} e^{-2|\beta-\alpha|^2} \ . \tag{A.14}$$

The maximum value of the gaussian is the upper bound $2/\pi$ at $\alpha = \beta$, it is centered on β, the width is $1/\sqrt{2}$. Substituting the special case of $\beta = 0$, the expression for a vacuum state can be found (subsequently shown in eqn. (A.15). The Wigner function of this state is depicted in Fig. 31(a).The Wigner function of a coherent state is identical to the one shown translated by β. Other types of quasi-classical states are a thermal field, or squeezed states, but their description is outside of the scope of the thesis.

Non-classical states

The simplest states that present negativity are non-zero fock states. Its Wigner can be deduced to be

$$W^{[|n\rangle\langle n|]}(\alpha) = \frac{2}{\pi}(-1)^n e^{-2|\alpha|^2} \mathcal{L}_n(4|\alpha|^2) \ , \tag{A.15}$$

where $\mathcal{L}_n(x)$ is the nth Laguerre polynomial

$$\mathcal{L}_n(x) = \sum_{p=0}^{n} (-1)^p \frac{n!}{p!^2(n-p)!} x^p \ . \tag{A.16}$$

In eqn. (A.15), the Wigner distribution is only a function of the modulus of alpha $|\alpha|^2$, reflecting the phase independence of Fock states. Substituting the value $\mathcal{L}_n(0) = 1$, the maximum value at the center depends on the parity of the photon number

$$W^{[|n\rangle\langle n|]}(0) = \frac{2}{\pi}(-1)^n \ . \tag{A.17}$$

In general, all photon number states except $|0\rangle$ have negativities. For example, the Wigner function of a single photon

$$W^{[|1\rangle\langle 1|]}(\alpha) = \frac{2}{\pi} e^{-2|\alpha|^2}(1 - 4|\alpha|^2) \ , \tag{A.18}$$

is shown in Fig. 31(b). The non-classical state that we most care about is given by the so called "phase SCS" well treated in chapter 1. The wavefunction can be rewritten in a slightly different way

$$|\psi^{\pm}_{cat}\rangle = \frac{1}{\sqrt{\mathcal{N}_{\pm}}}(|\beta\rangle \pm |-\beta\rangle) \ , \tag{A.19}$$

with the normalization factor

$$\mathcal{N}_{\pm} = 2(1 \pm e^{-2|\beta|^2}) \ , \tag{A.20}$$

resulting from the fact that the coherent state basis is overcomplete, so $|\beta\rangle$ and $|-\beta\rangle$ overlap. Substituting the density matrix of a SCS $\rho^{\pm}_{cat} = |\psi^{\pm}_{cat}\rangle\langle\psi^{\pm}_{cat}|$ into eqn. (A.6) the expression becomes

$$W^{\pm}_{cat}(\alpha) = \frac{1}{\pi^2 \mathcal{N}_{\pm}} \int e^{(\alpha\lambda^* - \alpha^*\lambda)} (|\beta\rangle D(\lambda)|\beta\rangle + |-\beta\rangle D(\lambda)|-\beta\rangle \pm |\beta\rangle D(\lambda)|-\beta\rangle \pm |-\beta\rangle D(\lambda)|\beta\rangle)\, d^2\lambda \ . \tag{A.21}$$

The quantum coherence of the SCSs can be noticed from the last two terms, while the first two are the weighted coherent states that lead to eqn. (A.14). When considering a statistical mixture, only these two terms are present in the Wigner function. The coherence terms can be integrated as Gaussian integrals, giving the final expression

$$W^{\pm}_{cat}(\alpha) = \frac{2}{\pi(1 \pm e^{-2|\beta|^2})} [e^{-2|\alpha+\beta|^2} + e^{-2|\alpha-\beta|^2} \pm e^{-2|\alpha|^2} \cos\left(4\, Im(\alpha)\beta\right)] \ , \tag{A.22}$$

with the insertion $\mathcal{N}_{\pm}$ from eqn. (A.20) and the assumption that β is real for simplicity, subsequently exploiting

$$|-\beta\rangle D(\lambda)|\beta\rangle = e^{i\beta\, Im(\lambda)} \langle -\beta|\beta + \lambda\rangle = e^{(-2\beta(\beta+\lambda) - |\lambda|^2/2)} \ . \tag{A.23}$$

The Wigner function of $|\psi^{+}_{cat}\rangle$ is shown in Fig. 31(c).

B Dispersive regime addendum

In this chapter belong all further analysis and calculations related to the dispersive regime and parity measurements. In section B.1, the reasoning behind small oscillations in parity measurements is explained. In section B.2 the qubit population of the parity measurement sequence is computed for whichever qubit initial state up to the first order in the dispersive parameter $\xi = g/\delta_k$. section B.3 consists in the second order calculation and a way to reduce dispersive regime imperfections.

B.1 Parity measurements oscillations

In this section, the cause of the slight modulation pattern of the qubit population in parity measurements is explained in a pictorial way backed up by simulations. In Fig. 32(a) parity measurements for a detuning of $\delta_{qi} = 3$ MHz are shown. The high frequency modulation is imperceptible. In Fig. 32(b) parity measurements are shown for the same parameters except for $\delta_{qi} = 1$ MHz and the coupling g_k such that $2g_k^2/\delta_{qi}$ and subsequently the interaction time $t_{int} = \pi/\chi$ is kept constant. In this case, the oscillations described are strongly visible. These additional small high frequency oscillations can be attributed to higher order terms in the dispersive approximation. To understand these oscillations on an intuitive level it is possible to go back to the JC Hamiltonian. The qubit experiences two influences towards different perpendicular axes, the coupling term proportional to g and the detuning proportional to δ_k. The resulting effect can be calculated using the law of addition of two vectors, with consequent expression $\sqrt{g^2 + \delta_k^2} \approx \delta_k$ in the limit of $\delta_k \gg g$. Hence, the qubit experiences oscillations due to the detuning with the phonon with a frequency similar to the detuning itself, as can be seen in the figures.

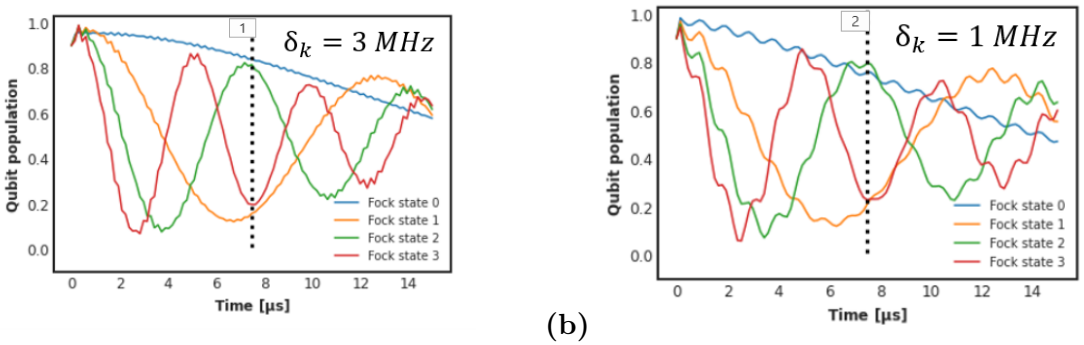

(a) (b)

Figure 32: Parity measurements simulated as in subsection 4.1.2, keeping $\chi = 2g_k^2/\delta_k$ constant for interaction detunings (a) $\delta_k = 3$ MHz and (b) $\delta_k = 1$ MHz.

B.2 Ramsey sequence in the dispersive regime calculations

The following discussion is adapted from [1]. Suppose initially the qubit is in the ground state, such that the initial state is

$$|\psi_0\rangle = \sum_n c_n |g, n\rangle \ . \tag{B.1}$$

The first gates consists of a $\pi/2$ pulse with parameter ϕ determining the angle of the axis of rotation, transforming $|g\rangle$ in $|g\rangle + e^{i\phi}|e\rangle$. After the application of the gate, the new wave

function ψ_1 can be written as

$$|\psi_1\rangle = \sum_n c_n \frac{1}{\sqrt{2}}(|g\rangle + e^{i\phi}|e\rangle) \otimes |n\rangle \ . \tag{B.2}$$

Subsequently, the same Schrieffer-Wolff (SW) U_{SW} transformation to derive eqn. (3.30) can be employed

$$U_{SW} = e^{\frac{g}{\delta_k}\hat{\sigma}^+ b_k - \frac{g}{\delta_k}\hat{\sigma}^- b_k^\dagger} \ . \tag{B.3}$$

acting on the basis states in the following way

$$\begin{aligned} U_{SW}|g,n\rangle &= |g,n\rangle + \xi\sqrt{n}|e,n-1\rangle + O(\xi^2) \ , \\ U_{SW}|e,n\rangle &= |e,n\rangle + \xi^*\sqrt{n+1}|g,n+1\rangle + O(\xi^2) \ , \end{aligned} \tag{B.4}$$

where $\xi = g/\delta_k$ for simplicity and omitting terms of second order or higher. Applying it on ψ_1

$$|\psi_2\rangle = \sum_n c_n \frac{1}{\sqrt{2}}[(|g,n\rangle + \xi\sqrt{n}|e,n-1\rangle) + e^{i\phi}(|e,n\rangle - \xi^*\sqrt{n+1}|g,n+1\rangle)] + O(\xi^2) \ . \tag{B.5}$$

Now, the crucial part is letting the state evolve for time $t_{ev} = \pi/\chi$, where $\chi = 2|g|^2/\delta_k$ is the dispersive parameter from eqn. (3.31). The Hamiltonian of eqn. (3.30) can be rewritten in the rotating frame of the dressed qubit frequency $\omega_q^{'} = \omega_q + |g|^2/\delta_k$. After the rotation the Hamiltonian H becomes

$$H = -\delta_k^{'}\hat{b}_k^\dagger\hat{b}_k + \frac{\chi}{2}\hat{\sigma}_z\hat{b}_k^\dagger\hat{b}_k \ . \tag{B.6}$$

with $\delta_k^{'} = \delta_k + |g|^2/\delta_k$. After the evolution ψ_2 transforms to

$$\begin{aligned} &|\psi_2(t=t_{ev})\rangle = e^{-iHt_{ev}}|\psi_2\rangle \\ &= \sum_n c_n \frac{1}{\sqrt{2}}[(e^{in\pi(\delta_k^{'}/|\chi|\pm 1/2)}|g,n\rangle + \xi\sqrt{n}e^{i(n-1)\pi(\delta_k^{'}/|\chi|\mp 1/2)}|e,n-1\rangle) \\ &+e^{i\phi}(e^{in\pi(\delta_k^{'}/|\chi|\mp 1/2)}|e,n\rangle - \xi^*\sqrt{n+1}e^{i(n+1)\pi(\delta_k^{'}/|\chi|\pm 1/2)}|g,n+1\rangle)] + O(\xi^2) \\ &= \sum_n c_n \frac{1}{\sqrt{2}}e^{in\pi(\delta_k^{'}/|\chi|\pm 1/2)}[(|g,n\rangle + \xi\sqrt{n}e^{-in\pi}e^{-i\pi(\delta_k^{'}/|\chi|\mp 1/2)}|e,n-1\rangle) \\ &+e^{i\phi}(e^{-in\pi}|e,n\rangle - \xi^*\sqrt{n+1}e^{i\pi(\delta_k^{'}/|\chi|\pm 1/2)}|g,n+1\rangle)] + O(\xi^2) \ . \end{aligned} \tag{B.7}$$

The wave function is shifted in the original basis by applying the complex conjugate of eqn. (B.3)

$$\begin{aligned} &|\psi_1(t=t_{ev})\rangle = U_{SW}^\dagger|\psi_2(t=t_{ev})\rangle \\ &= \sum_n c_n \frac{1}{\sqrt{2}}e^{in\pi(\delta_k^{'}/|\chi|\pm 1/2)}[(|g,n\rangle + \xi\sqrt{n}(e^{-in\pi}e^{-i\pi(\delta_k^{'}/|\chi|\mp 1/2)} - 1)|e,n-1\rangle) \\ &+e^{i\phi}(\xi\sqrt{n}e^{-in\pi}|e,n\rangle - \xi^*\sqrt{n+1}(e^{i\pi(\delta_k^{'}/|\chi|\pm 1/2)} - e^{-in\pi})|g,n+1\rangle)] + O(\xi^2) \ . \end{aligned} \tag{B.8}$$

Afterwards another $\pi/2$ is applied. This corresponds to the last gate of the Ramsey sequence with the same phase ϕ as the first $\pi/2$

$$\begin{aligned} |\psi_3\rangle &= \sum_n c_n \frac{1}{\sqrt{2}}e^{in\pi(\delta_k^{'}/|\chi|\pm 1/2)}[(1-e^{-in\pi})|g,n\rangle + e^{i\phi}(1+e^{-in\pi})|e,n\rangle \\ &+\xi\sqrt{n}(e^{-in\pi}e^{-i\pi(\delta_k^{'}/|\chi|\mp 1/2)} - 1)(|e,n-1\rangle - e^{-i\phi}|g,n-1\rangle) \\ &+e^{i\phi}e^{-in\pi}(\xi^*\sqrt{n+1}(1-e^{in\pi}e^{i\pi(\delta_k^{'}/|\chi|\pm 1/2)}(|g,n+1\rangle + e^{i\phi}|e,n+1\rangle)] + O(\xi^2) \ . \end{aligned} \tag{B.9}$$

By splitting states of fock number n in odd and even, subsequently substituting $e^{-in\pi} = \pm 1$ for n of different parity and taking the expectation value of the $\hat{\sigma}_z$ operation the final result is

$$\langle\hat{\sigma}_z\rangle_\phi = \langle\psi_3|\hat{\sigma}_z \otimes \sum_{n'}|n'\rangle\langle n'||\psi_3\rangle = \sum_{even\ n}|c_n|^2 - \sum_{odd\ n}|c_n|^2$$
$$+ \sum_{even\ n}\frac{1}{\sqrt{2}}[c_n e^{in\pi(\delta_k^{'}/|\chi|\pm 1/2)}(-\xi^*\sqrt{n+1}c^*_{n+1}e^{-i(n+1)\pi(\delta_k^{'}/|\chi|\pm 1/2)}e^{i\phi}(e^{-i\pi(\delta_k^{'}/|\chi|\mp 1/2)})+1)$$
$$-\xi\sqrt{n}c^*_{n-1}e^{-i(n-1)\pi(\delta_k^{'}/|\chi|\pm 1/2)}e^{i\phi}(e^{-i\pi(\delta_k^{'}/|\chi|\pm 1/2)})+1) + h.c.]$$
$$+ \sum_{odd\ n}\frac{1}{\sqrt{2}}[c_n e^{in\pi(\delta_k^{'}/|\chi|\pm 1/2)}(\xi^*\sqrt{n+1}c^*_{n+1}e^{-i(n+1)\pi(\delta_k^{'}/|\chi|\pm 1/2)}e^{i\phi}(e^{-i\pi(\delta_k^{'}/|\chi|\mp 1/2)})+1)$$
$$-\xi\sqrt{n}c^*_{n-1}e^{-i(n-1)\pi(\delta_k^{'}/|\chi|\pm 1/2)}e^{i\phi}(e^{-i\pi(\delta_k^{'}/|\chi|\pm 1/2)})+1) + h.c.]$$
$$+O(\xi^2)\ . \tag{B.10}$$

The zero order term $\langle\hat{\sigma}_z\rangle_\phi(0) = \sum_{even\ n}|c_n|^2 - \sum_{odd\ n}|c_n|^2 = \mathcal{P}$ is the parity value expected from an ideal measurement. From the Hamiltonian of eqn. (B.6), it is possible to deduce that the fock state number induces a shift of χ in the qubit frequency.

B.3 Four phase average

In the previous section, the expression of the expectation value of the qubit after a Ramsey sequence close to the phonon mode has been derived. However, all the higher order terms as a function of $\xi = g/\delta_k$ have been neglected. Including these terms, it is possible to compute second order terms, which are strong enough to appear at relatively small detunings, as in the simulation and measurement case of this work ($g_k/\delta_k \approx 1/7$). These terms are

$$\langle\hat{\sigma}_z\rangle_\phi = \langle\hat{\sigma}_z\rangle_\phi(0) + \langle\hat{\sigma}_z\rangle_\phi(\xi) + \frac{|\xi^2|}{2}\left(2\sin|\phi| - \sum_{even\ n}|c_n|^2 + \sum_{odd\ n}|c_n|^2\right)$$
$$+Re\left(\xi^2 e^{-2i\phi}(1+e^{2i\phi})\left(\sum_{even\ n}c_n c^*_{n-2}\sqrt{n(n-1)} - \sum_{odd\ n}c_n c^*_{n-2}\sqrt{n(n-1)}\right)\right) + O(\xi^3)\ , \tag{B.11}$$

where $\langle\hat{\sigma}_z\rangle_\phi(0)$ and $\langle\hat{\sigma}_z\rangle_\phi(\xi)$ are respectively the zero and first order term in ξ. From the calculations of section B.2, it is elementary to check that evaluating $\langle\hat{\sigma}_z\rangle_\phi + \langle\hat{\sigma}_z\rangle_{\phi+\pi}$ makes the terms of the first order in ξ cancel out. Furthermore, from the calculations of this section it can be seen that the last line of eqn. (B.11) can also be canceled out by averaging out over four different phases linearly spaced by $\pi/2$ intervals taking

$$\langle\hat{\sigma}_z\rangle_{avg} = (\langle\hat{\sigma}_z\rangle_\phi + \langle\hat{\sigma}_z\rangle_{\phi+\frac{\pi}{2}} + \langle\hat{\sigma}_z\rangle_{\phi+\pi} + \langle\hat{\sigma}_z\rangle_{\phi+3\frac{\pi}{2}})/4\ . \tag{B.12}$$

In Fig. 33(a), (b), (c) and (d), each individual wigner function measured with the four different phases is shown. To isolate the imperfections for each phase, same parameters are used as in Table 1 but decoherence times are set to ∞. Imperfections are still present from the term $|\xi|^2(\sin|\phi| - \mathcal{P}/2 + O(\xi^3)$. However, much better states can be measured by averaging, as shown in Fig. 33(e).

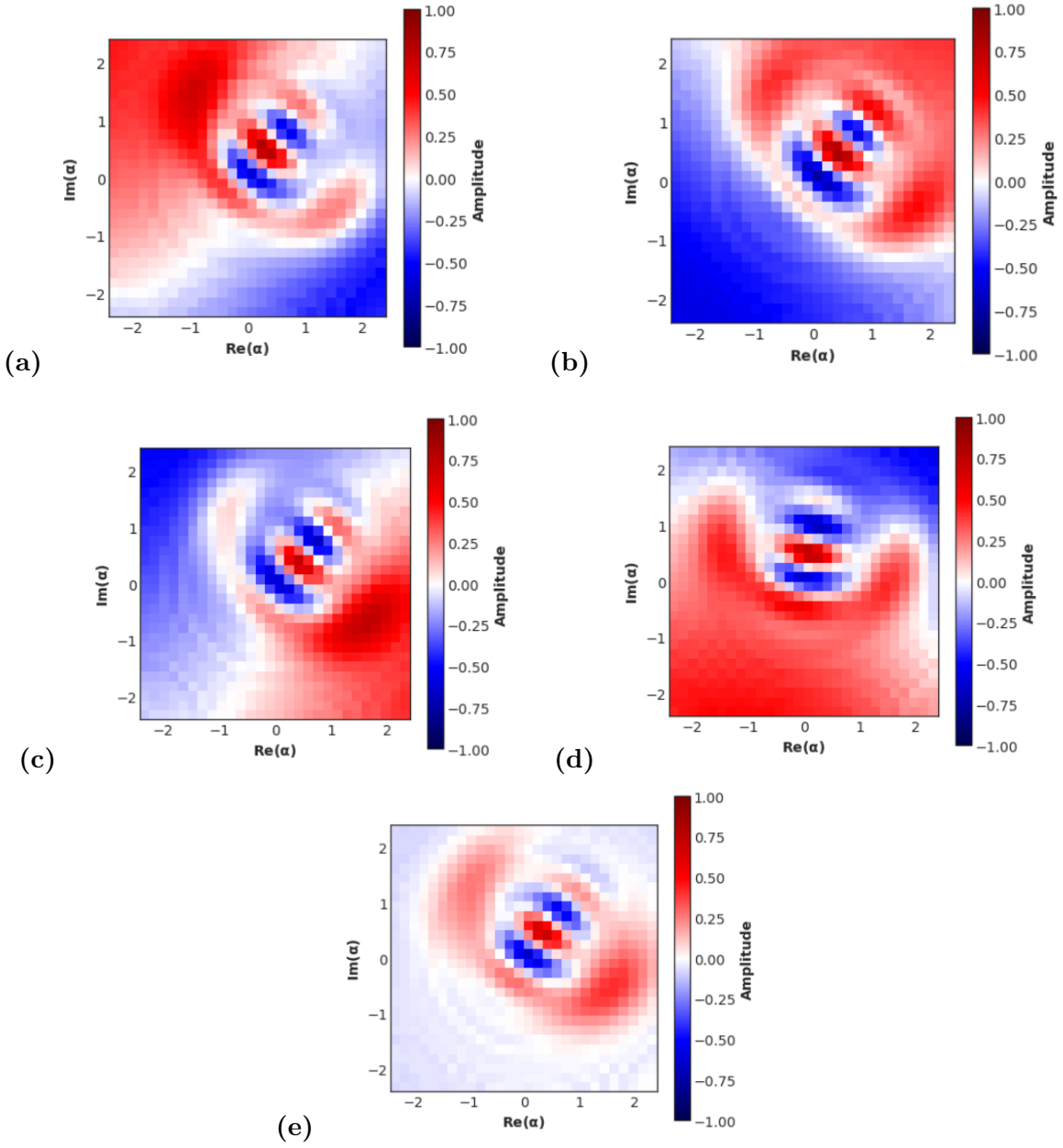

Figure 33: Resonant cat simulated wigner functions for different qubit phases. (a) with $\phi = 0$, (b) with $\phi = \pi/2$,(c) with $\phi = \pi$, (d) with $\phi = 3\pi/2$. For better understanding, the average of the four wigner functions is shown in (e).

C Pulse shape modification

An envelope of a pulse in time can drastically vary its shape in frequency domain. Not optimizing the pulse shape can be detrimental for experiments due to frequency overlap with undesired transitions. In this way, undesired excitations of some other states may occur. The most common waveform is a simple sinusoidal multiplied by a square pulse. The amplitude of this pulse ϵ depends only on time when multiplied by the sinusoidal wave at the desired frequency in the following way

$$\epsilon_s(t) = \begin{cases} \epsilon_0 & \text{if } 0 < t < t_p \\ 0 & \text{otherwise} \end{cases} , \tag{C.1}$$

with ϵ_0 the maximum value of the pulse and t_p being the full pulse time length. A different envelope for a waveform can be engineered. It is extremely prevalent to substitute the constant pulse with a "flat top gaussian", composed by a square pulse sandwiched by gaussian tails as in the subsequent equation

$$\epsilon_{ft}(t) = \begin{cases} \epsilon_0 e^{-\frac{(t-t_g)^2}{2\sigma_g^2}} & \text{if } 0 < t < t_g \\ \epsilon_0 & \text{if } t_g < t < t_p - t_g \\ \epsilon_0 e^{-\frac{(t-(t_p-t_g))^2}{2\sigma_g^2}} & \text{if } t > t_p - t_g \\ 0 & \text{otherwise} \end{cases} , \tag{C.2}$$

with ϵ_0 and t_p defined as before, t_g each of the gaussian tail time length, σ_g the standard deviation of each tail. Both waveform envelopes presented are plotted for a total length of 3 µs in Fig 34(a). It is possible to express the Fourier transform of the envelopes by writing flat top gaussian as a convolution of a gaussian with a constant pulse

$$\epsilon_{ft}(t) = (g * s)(t) = \int_{-\infty}^{+\infty} g(\tau) s(t-\tau)\, d\tau \ , \tag{C.3}$$

with $g(t)$ being a normal gaussian pulse envelope $g(t) \propto e^{-\frac{(t-t_g)^2}{2(\sigma_g)^2}}$ and $s(t)$ defined as eqn. (C.1). Knowing that the Fourier transform of a square pulse of length t_s is

$$\mathcal{FT}\{s(t)\} = t_s \,\mathrm{sinc}\left(\frac{\omega t_s}{2}\right) e^{-i\pi\omega t_s} \ , \tag{C.4}$$

where $\mathrm{sinc}(x) = \sin(x)/x$, that the Fourier transform of a gaussian is another gaussian

$$\mathcal{FT}\{g(t)\} = 2\,\sigma_g^2\,\epsilon_0\,\pi\, e^{-2\pi^2\omega^2\sigma_g^2} \ , \tag{C.5}$$

and that the convolution in time converts to a multiplication in fourier space, the flat top gaussian in frequency can be written as

$$\begin{aligned} \mathcal{FT}\{\epsilon_{ft}(t)\} &= \mathcal{FT}\{(g*s)(t)\} = \mathcal{FT}\{g(t)\}\mathcal{FT}\{s(t)\} \\ &= 2\,\sigma_g^2\,\epsilon_0\,\pi\, t_s\ \mathrm{sinc}\left(\frac{\omega t_s}{2}\right) e^{-i\pi\omega t_s}\, e^{-2\pi^2\omega^2\sigma_g^2} \ . \end{aligned} \tag{C.6}$$

In frequency domain, this means that the secondary lobes of the corresponding sync function are far decreased in amplitude because of the gaussian modulation, which acts like a low pass filter in both frequency directions. The Fourier transform of the pulses with their

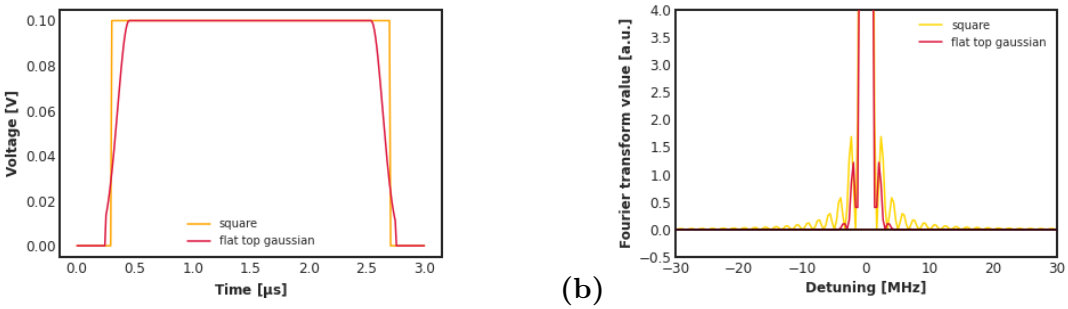

Figure 34: The square pulse and the square gaussian pulse are shown in (a). Their respective Power Spectral Densities (PSD) have the same integral value and are shown in (b). The tails of the FFT of the square gaussian are contained in frequency close to the carrier.

comparison can be seen in Fig. 34(b). This waveform is employed in the protocols for two main applications: the first is for phonon drives, for which usual values are: $t_p = 5 - 15$ µs, $t_g = 100 - 500$ ns, $\sigma_g = t_g/2$ for a standard deviation 4 times smaller than the gaussian length, and ϵ_0 depending on the qubit-phonon detuning and target phonon state. These parameters reduces the likelihood of driving other phonon modes or the qubit itself. The second implementation is used when stark-shifting the qubit, for which values are: t_p variable, $t_g = 10 - 20$ ns, $\sigma_g = t_g/2$ as before, and ϵ_0 depending on the cavity-pulse detuning and target qubit frequency. This pulse shape ensures qubit frequency tuning without affecting the cavity as much as with a square pulse.

D Coherent drive in cQAD

After simulations and theory calculations aided by code in Python, a new unexpected revelation about phonon coherent drive has emerged. The computations with unitary transformations mentioned in subsection 3.3.2 are well established in cQED systems. However, the system parameters of cQAD and the device of this work, have a fundamental dissimilarity, already mentioned in the context of the approximation of χ described in eqn. (3.31). That means that the anharmonicity term α is much larger than the qubit-phonon detuning. It turns out that it is not possible to perform the same approximation as the cQED case. The detuning δ_k is so small compared to the anharmonicity α, such that different terms become relevant. To make calculations easier, it is useful to employ the approximation of a two level system, in which $\alpha \to \infty$ and $\hat{q}^\dagger \hat{q}$ can be substituted with $\hat{\sigma}_z$. Using SymPi code, the starting point is the two-level system Hamiltonian, plus the drive and the JC interaction

$$H = \delta_k \frac{\sigma_z}{2} + \epsilon\hat{\sigma}_- + \epsilon\hat{\sigma}_+ + g_k\hat{\sigma}_-\hat{b}_k^\dagger + g_k\hat{\sigma}_+\hat{b}_k \ , \tag{D.1}$$

where g and ϵ are assumed real, $\hat{\sigma}_+ = (\hat{\sigma}_x + \hat{\sigma}_y)/2$, $\hat{\sigma}_- = (\hat{\sigma}_x - \hat{\sigma}_y)/2$ and the Hamiltonian has been written in the phonon rotating frame. It is possible to apply the unitary transformation

$$U = e^{-\lambda_k \hat{b}_k^\dagger \hat{\sigma}_- + \lambda_k \hat{b}_k \hat{\sigma}_+} \ , \tag{D.2}$$

with $\lambda_k = g_k/\delta_k$. the transformed Hamiltonian becomes

$$H' = \delta_k \frac{\sigma_z}{2} + \epsilon\hat{\sigma}_- + \epsilon\hat{\sigma}_+ + \epsilon\frac{g_k}{\delta_k}\hat{b}_k^\dagger\sigma_z + \epsilon\frac{g_k}{\delta_k}\hat{b}_k\sigma_z + \frac{g_k^2}{2\delta_k} + \frac{g_k^2}{\delta_k}\hat{b}_k^\dagger\hat{b}_k\sigma_z + \frac{g_k^2}{2\delta_k}\sigma_z \ . \tag{D.3}$$

The first three terms of the Hamiltonian refer to qubit driving. The fundamental terms are the fourth and fifth, resembling very closely the Hamiltonian of eqn. (4.1), with an additional σ_z. The sixth term consists only of a constant offset, while the last two terms are higher order terms in g_k. Hence, it has been discovered that in this parameter regime the displacement is conditional to the qubit state. The higher order terms can also be slightly spotted in simulations, especially for lower detunings. Their presence can be noticed especially when changing the phase of the qubit superposition states for the different protocols. In Fig. a coherent state for a qubit in $|g\rangle$ has been shown. Here, the displacement is calibrated again with a phase such that the resulting coherent state is on $\Re(\alpha)$ and for $\alpha = 1.5$. To demonstrate the effect of qubit state dependent drive with the simulator, coherent state creation is shown for two additional different initial qubit states. In Fig. 35(a) the qubit is in $|e\rangle$, in Fig. 35(b) the qubit is in $(|g\rangle + |e\rangle)/\sqrt{2}$. Decoherence is removed for better understanding. The surprising fact described in this section is, on one hand, detrimental because it infers the impossibility of a perfect unconditional displacement on the phonon mode. On the other hand, it enables the users of such devices to exploit unconditional operations and shorten protocols, for example the qcMAP as already described in subsection 2.4 or the Heralded cat in a similar manner.

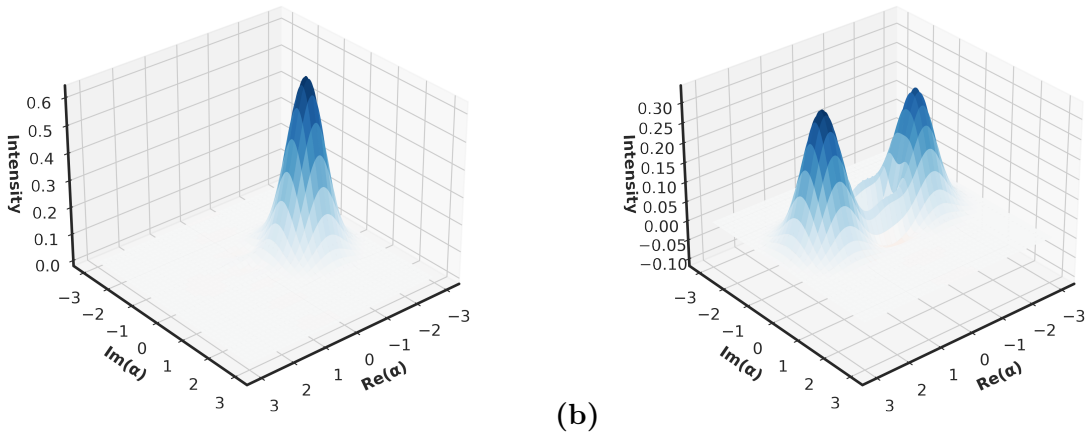

(a) **(b)**

Figure 35: Coherent state creation for $\alpha = 1.5$ along the real axis for different qubit initial states. In (a), the state is $|e\rangle$. In (b), the state is $(|g\rangle + |e\rangle)/\sqrt{2}$.

Acknowledgements

I would like to thank the whole Hybrid Quantum Systems (HyQu) group for the incredible atmosphere and kind help when needed.

Special thanks to Marius Bild, for an excellent supervision, always available with his constant fruitful discussions and answering countless questions. Thanks also to Yu Yang for his constant support and insights during simulations and experiments. The two of them have additionally contributed proofreading the Thesis. Dr. Matteo Fadel, with his acumen, has provided exceptional help in coherence and sensitivity simulations. I would like to thank Uwe von Lüpke, because my measurements would not have been possible without the device he fabricated.

I would like to express my gratitude to Prof. Yiwen Chu, for allowing me to conduct an extremely exciting Master's Thesis in her lab group.

References

[1] Uwe von Lüpke, Yu Yang, Marius Bild, Laurent Michaud, Matteo Fadel, and Yiwen Chu. Parity measurement in the strong dispersive regime of circuit quantum acoustodynamics. *arXiv:2110.00263 [quant-ph]*, October 2021. arXiv: 2110.00263.

[2] Gordon E Moore. Cramming more components onto integrated circuits. 38(8):4, 1965.

[3] Dr Ian Cutress. Samsung Foundry: 2nm Silicon in 2025.

[4] Anton Shilov. TSMC Roadmap Update: 3nm in Q1 2023, 3nm Enhanced in 2024, 2nm in 2025.

[5] Intel Technology Roadmaps and Milestones.

[6] Martin Fuechsle, Jill A. Miwa, Suddhasatta Mahapatra, Hoon Ryu, Sunhee Lee, Oliver Warschkow, Lloyd C. L. Hollenberg, Gerhard Klimeck, and Michelle Y. Simmons. A single-atom transistor. *Nature Nanotechnology*, 7(4):242–246, April 2012.

[7] Frank Arute, Kunal Arya, Ryan Babbush, Dave Bacon, Joseph C. Bardin, Rami Barends, Rupak Biswas, Sergio Boixo, Fernando G. S. L. Brandao, David A. Buell, Brian Burkett, Yu Chen, Zijun Chen, Ben Chiaro, Roberto Collins, William Courtney, Andrew Dunsworth, Edward Farhi, Brooks Foxen, Austin Fowler, Craig Gidney, Marissa Giustina, Rob Graff, Keith Guerin, Steve Habegger, Matthew P. Harrigan, Michael J. Hartmann, Alan Ho, Markus Hoffmann, Trent Huang, Travis S. Humble, Sergei V. Isakov, Evan Jeffrey, Zhang Jiang, Dvir Kafri, Kostyantyn Kechedzhi, Julian Kelly, Paul V. Klimov, Sergey Knysh, Alexander Korotkov, Fedor Kostritsa, David Landhuis, Mike Lindmark, Erik Lucero, Dmitry Lyakh, Salvatore Mandrà, Jarrod R. McClean, Matthew McEwen, Anthony Megrant, Xiao Mi, Kristel Michielsen, Masoud Mohseni, Josh Mutus, Ofer Naaman, Matthew Neeley, Charles Neill, Murphy Yuezhen Niu, Eric Ostby, Andre Petukhov, John C. Platt, Chris Quintana, Eleanor G. Rieffel, Pedram Roushan, Nicholas C. Rubin, Daniel Sank, Kevin J. Satzinger, Vadim Smelyanskiy, Kevin J. Sung, Matthew D. Trevithick, Amit Vainsencher, Benjamin Villalonga, Theodore White, Z. Jamie Yao, Ping Yeh, Adam Zalcman, Hartmut Neven, and John M. Martinis. Quantum supremacy using a programmable superconducting processor. *Nature*, 574(7779):505–510, October 2019.

[8] Philip Ball. FIRST 100-QUBIT QUANTUM COMPUTER ENTERS CROWDED RACE. page 1.

[9] S. Krinner, S. Storz, P. Kurpiers, P. Magnard, J. Heinsoo, R. Keller, J. Lütolf, C. Eichler, and A. Wallraff. Engineering cryogenic setups for 100-qubit scale superconducting circuit systems. *EPJ Quantum Technology*, 6(1):2, December 2019.

[10] Morten Kjaergaard, Mollie E. Schwartz, Jochen Braumüller, Philip Krantz, Joel I.-J. Wang, Simon Gustavsson, and William D. Oliver. Superconducting Qubits: Current State of Play. *Annual Review of Condensed Matter Physics*, 11(1):369–395, 2020. _eprint: https://doi.org/10.1146/annurev-conmatphys-031119-050605.

[11] Bosonic quantum error correction codes in superconducting quantum circuits | Elsevier Enhanced Reader.

[12] Kishor Bharti, Alba Cervera-Lierta, Thi Ha Kyaw, Tobias Haug, Sumner Alperin-Lea, Abhinav Anand, Matthias Degroote, Hermanni Heimonen, Jakob S. Kottmann,

Tim Menke, Wai-Keong Mok, Sukin Sim, Leong-Chuan Kwek, and Alán Aspuru-Guzik. Noisy intermediate-scale quantum algorithms. *Reviews of Modern Physics*, 94(1):015004, February 2022.

[13] Nissim Ofek, Andrei Petrenko, Reinier Heeres, Philip Reinhold, Zaki Leghtas, Brian Vlastakis, Yehan Liu, Luigi Frunzio, S. M. Girvin, L. Jiang, Mazyar Mirrahimi, M. H. Devoret, and R. J. Schoelkopf. Extending the lifetime of a quantum bit with error correction in superconducting circuits. *Nature*, 536(7617):441–445, August 2016.

[14] A. Grimm, N. E. Frattini, S. Puri, S. O. Mundhada, S. Touzard, M. Mirrahimi, S. M. Girvin, S. Shankar, and M. H. Devoret. Stabilization and operation of a Kerr-cat qubit. *Nature*, 584(7820):205–209, August 2020.

[15] E. Flurin, V.V. Ramasesh, S. Hacohen-Gourgy, L.S. Martin, N.Y. Yao, and I. Siddiqi. Observing Topological Invariants Using Quantum Walks in Superconducting Circuits. *Physical Review X*, 7(3):031023, August 2017.

[16] Luke D. Burkhart, James Teoh, Yaxing Zhang, Christopher J. Axline, Luigi Frunzio, M. H. Devoret, Liang Jiang, S. M. Girvin, and R. J. Schoelkopf. Error-detected state transfer and entanglement in a superconducting quantum network. *PRX Quantum*, 2(3):030321, August 2021. arXiv: 2004.06168.

[17] B. M. Escher, R. L. de Matos Filho, and L. Davidovich. General framework for estimating the ultimate precision limit in noisy quantum-enhanced metrology. *Nature Physics*, 7(5):406–411, May 2011.

[18] Philip Reinhold, Serge Rosenblum, Wen-Long Ma, Luigi Frunzio, Liang Jiang, and Robert J. Schoelkopf. Error-corrected gates on an encoded qubit. *Nature Physics*, 16(8):822–826, August 2020.

[19] Fault-tolerant detection of a quantum error.

[20] Yiwen Chu, Prashanta Kharel, Taekwan Yoon, Luigi Frunzio, Peter T. Rakich, and Robert J. Schoelkopf. Creation and control of multi-phonon Fock states in a bulk acoustic-wave resonator. *Nature*, 563(7733):666–670, November 2018.

[21] John D. Trimmer. The Present Situation in Quantum Mechanics: A Translation of Schrödinger's "Cat Paradox" Paper. *Proceedings of the American Philosophical Society*, 124(5):323–338, 1980. Publisher: American Philosophical Society.

[22] David L. Hu. Falling felines and fundamental physics. *American Journal of Physics*, 88(6):511–511, 2020.

[23] D. Leibfried, E. Knill, S. Seidelin, J. Britton, R. B. Blakestad, J. Chiaverini, D. B. Hume, W. M. Itano, J. D. Jost, C. Langer, R. Ozeri, R. Reichle, and D. J. Wineland. Creation of a six-atom 'Schrödinger cat' state. *Nature*, 438(7068):639–642, December 2005.

[24] Christopher C. Gerry and P. L. Knight. Introductory quantum optics. 2004.

[25] Pierre Meystre. Exploring the Quantum: Atoms, Cavities, and Photons. page 3.

[26] E.T. Jaynes and F.W. Cummings. Comparison of quantum and semiclassical radiation theories with application to the beam maser. *Proceedings of the IEEE*, 51(1):89–109, January 1963. Conference Name: Proceedings of the IEEE.

[27] J. I. Cirac, M. Lewenstein, and P. Zoller. Laser cooling a trapped atom in a cavity: Bad-cavity limit. *Physical Review A*, 51(2):1650–1655, February 1995.

[28] Alexandre Blais, Ren-Shou Huang, Andreas Wallraff, S. M. Girvin, and R. J. Schoelkopf. Cavity quantum electrodynamics for superconducting electrical circuits: an architecture for quantum computation. *Physical Review A*, 69(6):062320, June 2004. arXiv: cond-mat/0402216.

[29] A. A. Clerk, K. W. Lehnert, P. Bertet, J. R. Petta, and Y. Nakamura. Hybrid quantum systems with circuit quantum electrodynamics. *Nature Physics*, 16(3):257–267, March 2020.

[30] V. Bužek, H. Moya-Cessa, P. L. Knight, and S. J. D. Phoenix. Schrödinger-cat states in the resonant Jaynes-Cummings model: Collapse and revival of oscillations of the photon-number distribution. *Physical Review A*, 45(11):8190–8203, June 1992.

[31] J. H. Eberly, N. B. Narozhny, and J. J. Sanchez-Mondragon. Periodic Spontaneous Collapse and Revival in a Simple Quantum Model. *Physical Review Letters*, 44(20):1323–1326, May 1980.

[32] Julio Gea-Banacloche. Collapse and revival of the state vector in the Jaynes-Cummings model: An example of state preparation by a quantum apparatus. *Physical Review Letters*, 65(27):3385–3388, December 1990.

[33] Michael A. Nielsen and Isaac L. Chuang. *Quantum Computation and Quantum Information: 10th Anniversary Edition*. Cambridge University Press, 2010.

[34] Zaki Leghtas, Gerhard Kirchmair, Brian Vlastakis, Michel H. Devoret, Robert J. Schoelkopf, and Mazyar Mirrahimi. Deterministic protocol for mapping a qubit to coherent state superpositions in a cavity. *Physical Review A*, 87(4):042315, April 2013.

[35] Mohammad Mirhosseini, Alp Sipahigil, Mahmoud Kalaee, and Oskar Painter. Superconducting qubit to optical photon transduction. *Nature*, 588(7839):599–603, December 2020.

[36] Junliang Jiang, Yongchao Li, Jiazheng Pan, Huabing Wang, Guozhu Sun, and Peiheng Wu. Mechanical Oscillators Based on Superconducting Membranes. In *2019 IEEE International Superconductive Electronics Conference (ISEC)*, pages 1–3, July 2019.

[37] É. Dumur, K. J. Satzinger, G. A. Peairs, M.-H. Chou, A. Bienfait, H.-S. Chang, C. R. Conner, J. Grebel, R. G. Povey, Y. P. Zhong, and A. N. Cleland. Quantum communication with itinerant surface acoustic wave phonons. *npj Quantum Information*, 7(1):173, December 2021.

[38] Yiwen Chu, Prashanta Kharel, William H. Renninger, Luke D. Burkhart, Luigi Frunzio, Peter T. Rakich, and Robert J. Schoelkopf. Quantum acoustics with superconducting qubits. *Science*, 358(6360):199–202, 2017.

[39] Gloria G See, Anming Gao, Lu Xu, Ralph Nuzzo, Songbin Gong, and Brian T. Cunningham. Quantum dot emission modulation using piezoelectric photonic crystal mems resonators. *Opt. Express*, 25(21):25831–25841, Oct 2017.

[40] Connor T. Hann, Chang-Ling Zou, Yaxing Zhang, Yiwen Chu, Robert J. Schoelkopf, S. M. Girvin, and Liang Jiang. Hardware-efficient quantum random access memory with hybrid quantum acoustic systems. *Physical Review Letters*, 123(25), 12 2019.

[41] Nicolas K. Fontaine, Roland Ryf, Haoshuo Chen, David T. Neilson, Kwangwoong Kim, and Joel Carpenter. Laguerre-Gaussian mode sorter. *Nature Communications*, 10(1):1865, December 2019.

[42] Jens Koch, Terri M. Yu, Jay Gambetta, A. A. Houck, D. I. Schuster, J. Majer, Alexandre Blais, M. H. Devoret, S. M. Girvin, and R. J. Schoelkopf. Charge-insensitive qubit design derived from the Cooper pair box. *Physical Review A*, 76(4):042319, October 2007.

[43] Michael. Tinkham. *Introduction to superconductivity / Michael Tinkham.* McGraw-Hill New York, 1975.

[44] Alexandre Blais, Arne L. Grimsmo, S. M. Girvin, and Andreas Wallraff. Circuit Quantum Electrodynamics. *Reviews of Modern Physics*, 93(2):025005, May 2021. arXiv: 2005.12667.

[45] Peter Zoller and C. W. Gardiner. Quantum Noise in Quantum Optics: the Stochastic Schr\"odinger Equation. *arXiv:quant-ph/9702030*, February 1997. arXiv: quant-ph/9702030.

[46] H. Carmichael. *Statistical Methods in Quantum Optics 1: Master Equations and Fokker-Planck Equations.* 01 2002.

[47] Yuli V. Nazarov, editor. *Quantum Noise in Mesoscopic Physics.* Springer Netherlands, Dordrecht, 2003.

[48] Alexandre Blais, Jay Gambetta, A. Wallraff, D. I. Schuster, S. M. Girvin, M. H. Devoret, and R. J. Schoelkopf. Quantum-information processing with circuit quantum electrodynamics. *Physical Review A*, 75(3):032329, March 2007.

[49] Hanhee Paik, D. I. Schuster, Lev S. Bishop, G. Kirchmair, G. Catelani, A. P. Sears, B. R. Johnson, M. J. Reagor, L. Frunzio, L. I. Glazman, S. M. Girvin, M. H. Devoret, and R. J. Schoelkopf. Observation of High Coherence in Josephson Junction Qubits Measured in a Three-Dimensional Circuit QED Architecture. *Physical Review Letters*, 107(24):240501, December 2011.

[50] D.M. Pozar. *Microwave Engineering, 4th Edition.* Wiley, 2011.

[51] Rüdiger Achilles and Andrea Bonfiglioli. The early proofs of the theorem of Campbell, Baker, Hausdorff, and Dynkin. *Archive for History of Exact Sciences*, 66(3):295–358, May 2012.

[52] QuTiP - Quantum Toolbox in Python.

[53] N. E. Frattini, V. V. Sivak, A. Lingenfelter, S. Shankar, and M. H. Devoret. Optimizing the nonlinearity and dissipation of a snail parametric amplifier for dynamic range. *Phys. Rev. Applied*, 10:054020, Nov 2018.

[54] M. Paris and J. Rehacek. *Quantum State Estimation.* Lecture Notes in Physics. Springer Berlin Heidelberg, 2014.

[55] Samuel Deléglise, Igor Dotsenko, Clément Sayrin, Julien Bernu, Michel Brune, Jean-Michel Raimond, and Serge Haroche. Reconstruction of non-classical cavity field states with snapshots of their decoherence. *Nature*, 455(7212):510–514, September 2008.

[56] Assessments of macroscopicity for quantum optical states | Elsevier Enhanced Reader.

[57] P. Ehrenfest. Bemerkung über die angenäherte Gültigkeit der klassischen Mechanik innerhalb der Quantenmechanik. *Zeitschrift fur Physik*, 45(7-8):455–457, July 1927.

[58] Luca Pezze, Augusto Smerzi, Markus K Oberthaler, Roman Schmied, and Philipp Treutlein. Quantum metrology with nonclassical states of atomic ensembles. *Rev. Mod. Phys.*, 90(3):70, 2018.

[59] Florian Fröwis, Pavel Sekatski, and Wolfgang Dür. Detecting Large Quantum Fisher Information with Finite Measurement Precision. *Physical Review Letters*, 116(9):090801, March 2016.

[60] Nelson Leung, Mohamed Abdelhafez, Jens Koch, and David Schuster. Speedup for quantum optimal control from automatic differentiation based on graphics processing units. *Physical Review A*, 95(4):042318, April 2017.

[61] E. Wigner. On the Quantum Correction For Thermodynamic Equilibrium. *Physical Review*, 40(5):749–759, June 1932.